

ABSTRACT

Title of dissertation: NONLINEAR PULSE PROPAGATION
 THROUGH AN OPTICAL FIBER:
 THEORY AND EXPERIMENT

Bhaskar Khubchandani, Doctor of Philosophy, 2004

Dissertation directed by: Professor Rajarshi Roy
 Department of Physics

Pulse propagation through optical fibers is studied for two different phenomena: (i) the evolution of four-wave-mixing and (ii) the interplay between self- and cross-phase modulation for ultra-short pulses in a polarization maintaining fiber.

For the four-wave-mixing case, we present the results of a study of the dynamical evolution of multiple four-wave-mixing processes in a single-mode optical fiber with spatially and temporally δ -correlated phase noise. A nonlinear Schrödinger equation (NLSE) with stochastic phase fluctuations along the length of the fiber is solved using the Split-Step Fourier method. Good agreement is obtained with previous experimental and computational results based on a truncated-ODE model in which stochasticity was seen to play a key role in determining the nature of the dynamics. The full NLSE allows for simulations with high frequency resolution (60 MHz) and frequency span (16 THz) compared to the truncated ODE model (300 GHz and 2.8 THz, respectively), thus enabling a more detailed comparison with observations. Fluctuations in the refractive index of the fiber core are found to be

a possible source for this phase noise. It is found that index fluctuations as small as 1 part per billion are sufficient to explain observed features of the evolution of the four-wave-mixing sidebands. These measurements and numerical models thus may provide a technique for estimating these refractive index fluctuations which are otherwise difficult to measure.

For the case of self- and cross-phase modulation, the evolution of orthogonal polarizations of asymmetric femtosecond pulses (810 nm) propagating through a birefringent single-mode optical fiber (6.9 cm) is studied both experimentally (using GRENOUILLE) and numerically (using a set of coupled NLSEs). A linear optical spectrogram representation is derived from the electric field of the pulses and juxtaposed with the optical spectrum and optical time-trace. The simulations are in good qualitative agreement with the experiments. Input temporal pulse asymmetry is found to be the dominant cause of output spectral asymmetry. The results indicate that it is possible to modulate short pulses both temporally and spectrally by passage through polarization maintaining optical fibers with specified orientation and length.

NONLINEAR PULSE PROPAGATION THROUGH
AN OPTICAL FIBER : THEORY AND EXPERIMENT

by

Bhaskar Khubchandani

Dissertation submitted to the Faculty of the Graduate School of the
University of Maryland, College Park in partial fulfillment
of the requirements for the degree of
Doctor of Philosophy
2004

Advisory Committee:
Professor Rajarshi Roy, Chair/Advisor
Dr. Parvez N. Guzdar, Co-Advisor
Professor Robert W. Gammon
Professor Thomas Antonsen
Professor Edward Ott

© Copyright by
Bhaskar Khubchandani
2004

Preface

If needed.

Foreword

If needed.

Dedication

If needed.

Acknowledgments

I owe my gratitude to all the people who have made this thesis possible and because of whom my graduate experience has been one that I will cherish forever.

First and foremost I'd like to thank my advisor, Professor Rajarshi Roy for giving me an invaluable opportunity to work on challenging and extremely interesting projects over the past four years. He has always made himself available for help and advice and there has never been an occasion when I've knocked on his door and he hasn't given me time. It has been a pleasure to work with and learn from such an extraordinary individual.

I would also like to thank my co-advisor, Dr. Parvez Guzdar. Without his extraordinary theoretical ideas and computational expertise, this thesis would have been a distant dream. Thanks are due to Professor Robert Gammon, Professor Edward Ott and Professor Thomas Antonsen for agreeing to serve on my thesis committee and for sparing their invaluable time reviewing the manuscript.

My colleagues at the nonlinear optics laboratory have enriched my graduate life in many ways and deserve a special mention. David DeShazer helped me start-off by rewriting the basic simulation code in a user-friendly format. Christian Silva provided help by setting up the GRENOUILLE apparatus and performing some of the simulations. My interaction with Rohit Tripathi, Ryan McAllister, Vasily Dronov, Min-Young Kim, Elizabeth Rogers, William Ray, Jordi Garcia Ojalvo, Riccardo Meucci, Atsushi Uchida, and Fabian Rogister has been very fruitful. I'd also like to thank Wing-Shun Lam and Benjamin Zeff for providing the LaTeX style files

for writing this thesis.

I would also like to acknowledge help and support from some of the staff members. Donald Martin's technical help is highly appreciated, as is the computer hardware support from Edward Condon, LaTeX and software help from Dorothea Brosius and purchasing help from Nancy Boone.

I owe my deepest thanks to my family - my mother and father who have always stood by me and guided me through my career, and have pulled me through against impossible odds at times. Words cannot express the gratitude I owe them. I would also like to thank Dr. Mohan Advani, Dr. Vasudeo Paralikar and Dr. Vinod Chaugule who are like family members to me.

My housemates at my place of residence have been a crucial factor in my finishing smoothly. I'd like to express my gratitude to Sivasankar Pandeti, Jayakumar Patil, Amit Trehan and Punyaslok Purakayastha for their friendship and support.

I would like to acknowledge financial support from the Office of Naval Research (ONR), Physics, for all the projects discussed herein.

It is impossible to remember all, and I apologize to those I've inadvertently left out.

Lastly, thank you all and thank God!

Table of Contents

List of Figures	ix
List of Abbreviations	xi
1 Introduction	1
1.1 Source of Nonlinearity in an Optical Fiber	1
1.2 Physics of Pulse Propagation	3
1.3 Numerical Pulse Propagation	6
1.4 Experimental Pulse Diagnostics	7
1.5 Group Velocity Dispersion	7
1.6 Self-Phase Modulation	8
1.7 Four-wave-mixing	9
1.8 Cross-Phase Modulation	10
1.9 Stimulated Inelastic Scattering	11
1.10 Outline of Thesis	12
1.11 Theorems	14
1.12 Axioms	14
1.13 Tables	14
1.13.1 Adding Extra Space between Text and Horizontal Lines	15
1.14 Figures	17
1.14.1 Numbering Figures	23
1.14.1.1 This is a Subsubsection	23
1.15 Short Titles	23
1.16 Figures on Text Page	24
1.17 Wrapping Text around Figure	25
1.18 LaTeX – A Typesetting Program	26
1.19 Using Bibtex	26
1.20 APS Physical Review Style and Notation Guide	27
2 Stochastic Four-Wave-Mixing	28
2.1 Overview	28
2.2 Experimental and Computational Background	30
2.3 Stochastic NLSE Model	32
2.4 Discussion	52
2.5 Conclusions	55
3 Stochastic Four-Wave-Mixing	58
3.1 Overview	58
3.2 Experimental and Computational Background	60
3.3 Stochastic NLSE Model	62
3.4 Discussion	82
3.5 Conclusions	85

A	Overview	88
A.1	Experimental and Computational Background	90
A.2	Stochastic NLSE Model	92
A.3	Discussion	112
A.4	Conclusions	115
B	Overview	118
B.1	Experimental and Computational Background	120
B.2	Stochastic NLSE Model	122
B.3	Discussion	142
B.4	Conclusions	145
	Bibliography	148

List of Figures

1.1	Figure with caption indented on both sides and single-spaced.	18
1.2	Schematic illustrating receding horizon control.	20
1.3	Figure placed landscape on page.	22
1.4	Schematic illustrating receding horizon control.	24
1.5	Text wrap around figure.	25
2.1	Multimode pulse input to the NLSE: (a) input pulse in time domain and (b) input spectrum.	36
2.2	Short caption for Figure 2.2.	38
2.3	Effects of inclusion of the multimode nature	39
2.4	Effects of inclusion of the pulsed nature	40
2.5	Other effects of inclusion of the pulsed nature	41
2.6	Comparison between experiments measurements	45
2.7	This figure caption is indented and single-spaced.	47
2.8	Comparison between the experiments measurements (filled squares . .	50
2.9	Evolution of the FWM spectrum	51
2.10	Experimental FWM output spectrum	51
3.1	Multimode pulse input to the NLSE: (a) input pulse in time domain and (b) input spectrum.	66
3.2	Short caption for Figure 3.2.	68
3.3	Effects of inclusion of the multimode nature	69
3.4	Effects of inclusion of the pulsed nature	70
3.5	Other effects of inclusion of the pulsed nature	71
3.6	Comparison between experiments measurements	75
3.7	This figure caption is indented and single-spaced.	77
3.8	Comparison between the experiments measurements (filled squares . .	80
3.9	Evolution of the FWM spectrum	81
3.10	Experimental FWM output spectrum	81
A.1	Multimode pulse input to the NLSE: (a) input pulse in time domain and (b) input spectrum.	96
A.2	Short caption for Figure A.2.	98
A.3	Effects of inclusion of the multimode nature	99
A.4	Effects of inclusion of the pulsed nature	100
A.5	Other effects of inclusion of the pulsed nature	101
A.6	Comparison between experiments measurements	105
A.7	This figure caption is indented and single-spaced.	107
A.8	Comparison between the experiments measurements (filled squares . .	110
A.9	Evolution of the FWM spectrum	111
A.10	Experimental FWM output spectrum	111
B.1	Multimode pulse input to the NLSE: (a) input pulse in time domain and (b) input spectrum.	126

B.2	Short caption for Figure B.2.	128
B.3	Effects of inclusion of the multimode nature	129
B.4	Effects of inclusion of the pulsed nature	130
B.5	Other effects of inclusion of the pulsed nature	131
B.6	Comparison between experiments measurements	135
B.7	This figure caption is indented and single-spaced.	137
B.8	Comparison between the experiments measurements (filled squares . .	140
B.9	Evolution of the FWM spectrum	141
B.10	Experimental FWM output spectrum	141

List of Abbreviations

AAA	Antiaircraft artillery
ABCCC	Airborne Battlefield Command and Control Center
AEHF	Advanced Extremely High Frequency
AGM	Air-to-ground guided missile
AIT	Assembly, Integration, and Testing
AOR	Area of Responsibility
APAM	Anti-personnel, anti-material
ASOC	Air Support Operations Center
ATACM	Army Tactical Missile System
ATO	Air Tasking Order
AWACS	Airborne Warning and Control System
BAT	Brilliant Ani-Armor Submunition
BDA	Bomb-damage assessment
BFT	Blue Force Tracking
BLOS	Beyond Line-of-Sight
BMD	Ballistic Missile Defense
C ³	Command, Control, and Communications
CAFMS	Computer-aided Force Management System
CALCM	Conventional Air-Launched Cruise Missile
CBU	Cluster Bomb Unit
CCAFS	Cape Canaveral Air Force Station
CENTAF	CENTCOM's Air Force component
CENTCOM	U.S. Central Command
CINC	Commander-in-Chief
CONUS	Continental United States
DAGR	Defense Advanced GPS Receiver
DMA	Defense Mapping Agency
DOD	Department of Defense
DOP	Dilution of Precision
DOT	Department of Transportation
DSMAC	Digital Scene Mapping Area Correlator
EFOG-M	Enhanced Fiber Optic Guided Missile
FAA	Federal Aviation Administration
FLIR	Forward-looking infrared

GAM	Global Positioning System Aided Munition
GPS	Global Positioning System
GWAPS	Gulf War Air Power Survey
HARM	High-Speed Antiradiation Missile
HEO	Highly Elliptical Orbit
IADS	Integrated Air Defense System
ICBM	Inter-Continental Ballistic Missile
INS	Inertial navigation system
IIR	Imaging infrared
IR	Infrared
ISR	Intelligence, Surveillance, and Reconnaissance
JDAM	Joint Direct Attack Munition
JFC	Joint Force Commander
JSOW	Joint Standoff Weapon
LANTIRN	Low-Altitude Navigation and Targeting Infrared for Night System
LEO	Low Earth Orbit
LGB	Laser-guided bomb
MAJIC	Microsatellite Area-Wide Joint Information Communication
MARCENT	CENTCOM's Marine component
MARS	Mid-Atlantic Regional Spaceport
MLRS	Multiple Launch Rocket System
MUOS	Mobile User Objective System
NASA	National Aeronautics and Space Administration
NAVCENT	CENTCOM's Navy component
NPOESS	National Polar-Orbiting Operational Environmental Satellite System
ORS	Operationally Responsive Space
ORSO	Operationally Responsive Space Office
PDOP	Position Dilution of Precision
PGM	Precision-guided munition
P ³ I	Preplanned Product Improvement
PnP	Plug and Play

PnPSat	Plug and Play Satellite
PPS	Precise Positioning Service
RCS	Radar cross section
SA	Situational Awareness
SADARM	Sense and Destroy Armor Munition
SAM	Surface-to-air missile
SAR	Synthetic aperture radar
SBIRS	Space Based Infrared System
SEAD	Suppression of enemy air defenses
SFW	Sensor Fuzed Weapon
SIGINT	Signal Intelligence
SLAM	Standoff Land Attack Missile
SLAM-ER	SLAM-Expanded Response
SpaceX	Space Exploration Technologies Corporation
SPS	Standard Positioning Service
TACC	Tactical Air Control Center
TACS	Tactical Air Control System
TACP	Tactical Air Control Party
TASM	Tomahawk Anti-Ship Missile
TBIP	Tomahawk Baseline Improvement Program
TERCOM	Terrain Contour Mapping
TFR	Terrain-following radar
TLAM	Tomahawk Land Attack Missile
USAF	U.S. Air Force
VAFB	Vandenberg Air Force Base
WGS	Wideband Global SATCOM

Chapter 1

Introduction

1.1 Source of Nonlinearity in an Optical Fiber

The response of any dielectric to light becomes nonlinear for intense electromagnetic fields. Standard optical fibers are made of fused silica which is a dielectric. The total polarization \mathbf{P} is nonlinear in the electric field \mathbf{E} and is given by [1-5] -

$$\mathbf{P} = \epsilon_0 \left(\chi^{(1)} : \mathbf{E} + \chi^{(2)} : \mathbf{E}\mathbf{E} + \chi^{(3)} : \mathbf{E}\mathbf{E}\mathbf{E} + \dots \right), \quad (1.1)$$

where ϵ_0 is the permittivity of free-space, and $\chi^{(j)}$ is the j -th order susceptibility of the dielectric. The linear susceptibility $\chi^{(1)}$ represents the dominant contribution to \mathbf{P} and its effects are included through the refractive index $n(\omega)$ and the attenuation coefficient $\alpha(\omega)$. $\chi^{(2)}$ is responsible for nonlinear effects such as sum-frequency generation and second harmonic generation [1, 3]. Fused silica does not manifest these effects as it is centro-symmetric [6]. Hence, the dominant nonlinear contribution to \mathbf{P} is due to $\chi^{(3)}$ which results in effects such as third harmonic generation, four-wave-mixing, self- and cross-phase modulation. The cubic nonlinearity results in an intensity dependent refractive index

122 23333

1114 14444

$$\tilde{n}(\omega, |E|^2) = n(\omega) + n_2|E|^2, \quad (1.2)$$

where $n(\omega)$ is the linear part given by the Sellmier equation which takes into account the resonance frequencies (ω_j) of fused silica [1, 7],

$$n^2(\omega) = 1 + \sum_{j=1}^m \frac{B_j \omega_j^2}{\omega_j^2 - \omega^2} \quad (1.3)$$

and n_2 is given by

$$n_2 = \frac{3}{8n} \text{Re}(\chi_{xxxx}^3) \quad (1.4)$$

for an optical wave assumed to be linearly polarized along one of the axes of a polarization maintaining fiber. The tensorial nature of $\chi^{(3)}$ needs to be considered for the case in which the light is not polarized along one of the fiber axes.¹

The experimentally measured value of n_2 for fused silica ranges from $2.2 - 3.4 \times 10^{-20} \text{ m}^2/\text{W}$, which is small compared to most other nonlinear media by at least 2 orders of magnitude [1]. Despite this, nonlinear effects are easily observed for silica fibers for relatively low input power levels due to the fact that the effective fiber core areas are small and the fiber losses are low. Single mode fibers (those which propagate a single transverse mode of light for a given wavelength) have effective fiber core diameters of the order of $5 \mu\text{m}$ thus causing the light intensities within the fiber to be large despite the smallness of the input power. The low loss in the fiber ($<10 \text{ dB/km}$) allows one to use long fibers to observe nonlinear phenomena.

¹This is my footnote. I started playing the piano when I was eight years old. This is my footnote. I started playing the piano when I was eight years old. This is my footnote. I started playing the piano when I was eight years old. This is my footnote. I started playing the piano when I was eight years old.

1.2 Physics of Pulse Propagation

Mathematically speaking, in the classical limit, pulse propagation in an optical fiber is governed by Maxwell's equations [8, 9],

$$\begin{aligned}\vec{\nabla} \times \vec{E} &= -\frac{\partial \vec{B}}{\partial t} \\ \vec{\nabla} \times \vec{H} &= \vec{J} + \frac{\partial \vec{D}}{\partial t} \\ \vec{\nabla} \cdot \vec{D} &= \rho_f \\ \vec{\nabla} \cdot \vec{B} &= 0,\end{aligned}\tag{1.5}$$

where \vec{E} and \vec{H} are electric and magnetic field vectors, and \vec{D} and \vec{B} are electric and magnetic flux densities, respectively. \vec{J} is the current density and ρ_f is the free charge density.

Under the following assumptions [8] -

- (a) there are no free charges ($\vec{J} = \rho_f = 0$), a good approximation for an optical fiber,
- (b) the medium is non-magnetic ($\vec{M} = 0$), which an optical fiber is,
- (c) the wavelength of light propagated is away from any material resonances (0.5 - 2 μm), the results described in this thesis lie in this wavelength range, i.e., the results presented in Chap. 2 and Chap. 3 lie in the 600-700 nm regime and the results presented in Chap. 4 lie in the 800 nm regime,
- (d) the electric-dipole approximation is valid, due to which the second-order parametric processes such as three-wave-mixing and second harmonic generation

can be neglected (in practice they do occur because of quadrupole and magnetic-dipole effects but with a very low efficiency),

- (e) the medium only responds locally, which is a valid approximation for the projects considered herein,
- (f) the nonlinear polarization \vec{P}_{NL} can be taken as a perturbation to the total induced polarization \vec{P} , which is justified as the nonlinear effects are relatively weak for the results presented in this thesis,
- (g) only 3rd order nonlinear effects need to be taken into account, which is valid up to 5th order in \mathbf{E} since the 2nd and 4th order effects are absent due to the centrosymmetric nature of the disordered liquidlike state of fused silica,
- (h) the imaginary part of the dielectric constant $\epsilon(\omega)$ is small compared to the real part (low loss, which is a good approximation for the wavelength regimes and fiber lengths considered here),
- (i) the wavelength of light is higher than the cutoff wavelength of the fiber so that the single transverse mode condition is satisfied (or else there would be multimode propagation and nonuniform modal dispersion would have to be taken into account),
- (j) the optical fiber is polarization maintaining and the light pulse is traveling along one of the 2 principal axes of the fiber, a very good approximation for the results of Chap. 2, and Chap. 3, in the case of Chap. 4, this approximation is

relaxed as the incident light travels along both axes of the fiber, thus requiring a set of two coupled NLSEs for simulation, one for each axis,

(k) the slowly varying envelope approximation is valid, i.e., $\Delta\omega/\omega_0 \ll 1$ where $\Delta\omega$ is the spectral width of the pulse spectrum which is centered at ω_0 , this approximation is valid for the studies considered in Chap. 2 and Chap. 4, in Chap. 3, the Raman Stokes wave is considered as a separate slowly varying envelope from the pump wave, as the two taken together would not satisfy this condition,

(l) the nonlinear response of the medium is instantaneous, an approximation valid for pulse widths greater than ~ 70 fs, which amounts to neglecting the contribution of molecular vibrations to $\chi^{(3)}$ (the Raman effect), which have been included in the study presented in Chap. 4 since the pulse width was ~ 140 fs.

The propagation of the slowly varying envelope $A(z,t)$ of a light pulse along an optical fiber is governed by the nonlinear partial differential equation [8] -

$$\frac{\partial A}{\partial z} + \beta_1 \frac{\partial A}{\partial t} + \frac{i\beta_2}{2} \frac{\partial^2 A}{\partial t^2} = i\gamma|A|^2 A, \quad (1.6)$$

where $v_g = 1/\beta_1$ is the group velocity of the pulse, β_2 is the group velocity dispersion coefficient, and γ is the nonlinearity coefficient given by

$$\gamma = \frac{n_2\omega_0}{cA_{eff}}. \quad (1.7)$$

Here ω_0 is the central angular frequency of the pulse and A_{eff} , the effective core area of the fiber.

Under transformation to a frame of reference moving at the group velocity of the pulse, the above equation takes the form of the so-called ‘nonlinear Schrödinger equation’ (NLSE), i.e.,

$$\frac{\partial A}{\partial z} + \frac{i\beta_2}{2} \frac{\partial^2 A}{\partial \tau^2} = i\gamma|A|^2A, \quad (1.8)$$

where

$$\tau = t - \frac{z}{v_g} \quad (1.9)$$

is time measured in a frame of reference moving at the group velocity v_g of the pulse.

1.3 Numerical Pulse Propagation

The NLSE, like most nonlinear partial differential equations, is not amenable to analytical solution except in certain special cases where the inverse scattering transform can be used [10]. Thus a numerical approach is necessary for understanding the physics of phenomena governed by the NLSE. The numerical methods available can be classified as finite-difference techniques and pseudo-spectral techniques. Usually pseudo-spectral methods are an order of magnitude faster, the most popular method being the Split-Step Fourier Method (SSFM) [8, 11, 12]. The speed of the SSFM can be partly attributed to the use of the finite fast-Fourier transform (FFT) algorithm [13]. For an algorithmic description of the SSFM the reader is referred to Chap. 2, Sec. 2. Therein is also described an unconditionally stable scheme for including linear multiplicative noise into the SSFM without disturbing the conservative properties of the NLSE. In the projects described in Chap. 3, simulations

were carried out using a combination of the SSFM and finite difference schemes. The SSFM is also used to arrive at the simulated results described in Chap. 4.

1.4 Experimental Pulse Diagnostics

With the advent of frequency resolved optical gating (FROG) [14, 15, 16], it has become possible to not only measure the optical spectrum and optical time trace of a light pulse but to measure the full electric field envelope (intensity and phase) of the light pulse. The two fields of nonlinear fiber optics and frequency resolved optical gating (FROG) are yet to undergo cross pollination to their fullest potential since the inception of FROG 10 years ago. This novel experimental technique adds new dimensions to pulse measurement techniques, one of which is the ability to measure how asymmetric a pulse is, i.e., measure its skewness, kurtosis and all higher order moments. Asymmetric pulse propagation is a subject of interest in Chap. 4, where a highly simplified version of FROG [17] is used to measure pulse characteristics before and after a fiber.

1.5 Group Velocity Dispersion

Group velocity dispersion [18] (GVD) involves the temporal broadening of a pulse as it propagates through an optical fiber. From the NLSE (Eq. 1.6) one can derive length scales relevant to linear dispersion ($L_D=T_0^2/\beta_2$) and nonlinearity ($L_{NL}=1/\gamma P_0$). Here T_0 is the pulse width and P_0 is the peak power of the pulse. The regime in which the effects of GVD dominate and the effects of nonlinearity are

negligible is given by -

$$\frac{L_D}{L_{NL}} = \frac{\gamma P_0 T_0^2}{|\beta_2|} \ll 1. \quad (1.10)$$

In this regime, optical pulses propagate as they undergo symmetric temporal broadening and linear chirping without any spectral broadening. The sign of the GVD parameter β_2 determines the sign of the induced chirp. If the input pulse is chirped, then it may undergo some initial pulse compression followed by temporal broadening. Unlike the second-order dispersion associated with GVD, third-order dispersion causes asymmetric temporal broadening with leading and trailing edges. It becomes important, when the operating wavelength is near the zero dispersion wavelength of the fiber (the wavelength at which $\beta_2=0$). GVD starts to limit optical fiber communication systems when consecutive pulses broaden so much that they start to overlap.

1.6 Self-Phase Modulation

Self-phase modulation [19] (SPM) is a phenomenon that leads to spectral broadening and modulation of optical pulses. In the absence of GVD, SPM induced spectral broadening occurs without change in the temporal pulse shape. The spectral broadening occurs as a consequence of an intensity dependent phase-shift. The project described in Chap. 2 has the property that $L_{NL} < L \ll L_D$, i.e., the nonlinear term representing SPM dominates. In the regime where both SPM and GVD are non-negligible (as in Chap. 4), phenomena qualitatively different from those described in this section and the previous section can occur. Both temporal

and spectral broadening can occur simultaneously. In the regime of femtosecond pulse propagation (as in Chap. 4), GVD, third-order dispersion, intrapulse Raman scattering (discussed in Chap. 2) and higher order nonlinear effects have to be taken into account. If the input pulse is asymmetric, then SPM effects dominate over all other effects, as is observed in Chap. 3. In some cases SPM can lead to pulse compression, and in the anomalous dispersion regime ($\beta_2 < 0$), the balance between GVD and SPM can lead to soliton formation.

1.7 Four-wave-mixing

Four-wave-mixing (FWM) [20] is a parametric process involving the interaction between four photons at different frequencies. Two different kinds of four-wave-mixing processes are possible -

$$\omega_4 = \omega_1 + \omega_2 + \omega_3 \quad (1.11)$$

$$\omega_3 + \omega_4 = \omega_1 + \omega_2. \quad (1.12)$$

The former process results in third harmonic generation for the special case when $\omega_1 = \omega_2 = \omega_3$. Both processes require phase matching to occur, in order to be efficient. For the latter case, with the partial degeneracy of $\omega_1 = \omega_2$, it is relatively easy to satisfy the phase matching condition of

$$\Delta k = k_3 + k_4 - k_1 - k_2 = 0. \quad (1.13)$$

This process is of great interest to nonlinear dynamicists as the evolution of the FWM process could constitute a route to chaos further down-stream in the fiber.

It is also of great interest to people working in the field of optical communication systems, as it can cause cross-talk between neighboring channels in a wavelength division multiplexing scheme of communication.

1.8 Cross-Phase Modulation

Cross-phase modulation (XPM) [21] occurs in optical fibers when two or more optical pulses having different central wavelengths propagate simultaneously inside a fiber, interacting through the fiber nonlinearity which couples the two pulses nonlinearly. The evolution of the two pulses depends on the group velocity mismatch between them by virtue of their being centered at different wavelengths, although this is a linear phenomenon. The group velocity mismatch also exists between light pulses traveling along orthogonal polarization axes of a fiber, and centered around identical wavelengths, since the slow axis and fast axis of the fiber have different group velocities. In this case, too, the two polarizations interact nonlinearly [22] through degenerate XPM (degenerate since the central wavelengths are the same). In the case of degenerate XPM the 2nd order and higher dispersion parameters, and the nonlinear parameters (all of which depend only on the wavelength), are also the same unlike in general XPM. The effects of XPM are more pronounced when one of the pulses (the pump) has much higher power than the other (the probe). Otherwise, the effects of self-phase modulation (SPM) tend to dominate.

1.9 Stimulated Inelastic Scattering

Other nonlinear effects (apart from those due to the cubic $\chi^{(3)}$ nonlinearity) arise due to the interaction between the light traveling in the fiber and the fiber medium. Interactions between the light field and the vibrational levels of the fiber medium lead to stimulated Brillouin scattering (SBS) and stimulated Raman scattering (SRS). SRS and SBS were among the first nonlinear effects studied in optical fibers [23, 24, 25]. In a simple quantum mechanical picture [1] applicable to both SRS and SBS, a photon of the incident field (called the pump) is annihilated to create a photon at a lower frequency (belonging to the Stoke's wave) and a phonon to conserve energy and momentum. SBS involves an acoustic phonon whereas SRS involves an optical phonon, thus they have qualitatively different dispersion relations. SBS has a much lower threshold power and manifest itself through a backward propagating wave in contrast to SRS which can involve both forward and backward traveling waves. SBS has a maximum gain at a frequency 10 GHz [26] (down-shifted with respect to the pump) and requires a very narrow bandwidth pump to manifest itself. SRS, in contrast, has a maximum gain at a frequency 13 THz [27] downshifted with respect to the pump. For pulse-bandwidths larger than 13 THz, the phenomenon of Intrapulse Raman Scattering (IRS) manifests itself, involving a self-frequency shift within the pulse from higher frequency components to lower frequency components. Thus, SRS becomes more important for shorter pulses (larger bandwidth) unlike SBS which nearly ceases to occur for pulses shorter than 10 ns. In both SRS and SBS, the optical fiber plays an active role in the nonlinear process, unlike the case of

cross- and self-phase modulation, four-wave-mixing and third harmonic generation, where the fiber plays a passive role by mediating the interaction between several optical waves.

1.10 Outline of Thesis

In Chap. 2, we present the results of a computational study of the influence of stochasticity on the dynamical evolution of multiple four-wave-mixing processes in a single mode optical fiber with spatially and temporally δ -correlated phase noise. A generalized nonlinear Schrödinger equation (NLSE) with stochastic phase fluctuations along the length of the fiber is solved using the Split-step Fourier method (SSFM). Good agreement is obtained with previous experimental and computational results based on a truncated-ODE (Ordinary Differential Equation) model in which stochasticity was seen to play a key role in determining the nature of the dynamics. The full NLSE allows for simulations with high frequency resolution (60 MHz) and frequency span (16 THz) compared to the truncated ODE model (300 GHz and 2.8 THz, respectively), thus enabling a more detailed comparison with observations. A physical basis for this hitherto phenomenological phase noise is discussed and quantified.

In Chap. 3, we discuss the implications of spontaneous and stimulated Raman scattering on the project discussed in Chap. 2, namely, the dynamical evolution of stochastic four-wave-mixing processes in an optical fiber. The following question is asked - can stimulated Raman scattering be a mechanism by which adequate

multiplicative stochastic phase fluctuations are introduced in the electric field of light undergoing four-wave-mixing as? Adequately checked numerical algorithms of stimulated Raman scattering (SRS), spontaneous Raman generation and intrapulse Raman scattering (IRS) are used while exploring this issue. The algorithms are described in detail, as also are the results of the simulations. It is found that a 50-meter length of fiber (as used in the experiments), is too short to see the influence of Raman scattering, which is found to eventually dominate for longer fiber lengths.

In Chap. 4, self- and cross-phase modulation (XPM) of femtosecond pulses (~ 810 nm) propagating through a birefringent single-mode optical fiber (~ 6.9 cm) is studied both experimentally (using GRENOUILLE - Grating Eliminated No Nonsense Observation of Ultrafast Laser Light Electric Fields) and numerically (by solving a set of coupled nonlinear Schrödinger equations or CNLSEs). An optical spectrogram representation is derived from the electric field of the pulses and is linearly juxtaposed with the corresponding optical spectrum and optical time-trace. The effects of intrapulse Raman scattering (IRS) are discussed and the question whether it can be a cause of asymmetric transfer of pulse energies towards longer wavelengths is explored. The simulations are shown to be in good qualitative agreement with the experiments. Measured input pulse asymmetry, when incorporated into the simulations, is found to be the dominant cause of output spectral asymmetry. ² The results indicate that it is possible to modulate short pulses both temporally and spectrally by passage through polarization maintaining optical fibers

²These averages are reported for 45 ‘detailed occupational codes’, which is an intermediate occupational classification (between two and three-digit codes) given by the Current Population Survey (CPS).

with specified orientation and length. The modulation technique is very direct and straightforward. No frequency components of the broadband pulse have to be rejected as the entire spectrum is uniformly modulated. The technique is flexible as the modulation spacing can be varied by varying the fiber length.

Chapter 5 provides the conclusion to the thesis.

1.11 Theorems

Theorem 1.1 *This is my first theorem.*

1.12 Axioms

Axiom 1.1 *This is my first axiom.*

Axiom 1.2 *This is my second axiom in chapter 1.*

1.13 Tables

This is my table.

Table 1.1: Overview of test cases used in this study.

Test case	Quality variable (QV)	Setpoint for QV	Manipulated variables (MVs)
TE AZ	G/H ratio xB(H_2O)	1.226	D-feed SP and Reactor Level SP Reflux flow and 5 th Tray temperature SP

My table is shown above. Normally it is double-spaced but I have inserted a

command (marked in blue) to make it single-spaced and then inserted a command (again in blue) to change the text back to double-spacing.

1.13.1 Adding Extra Space between Text and Horizontal Lines

Table 1.2: Table with Extra Space between the Text and Horizontal Lines.

Test case	Quality variable QV)	Setpoint for QV	Manipulated variables (MVs)
TE	G/H ratio	1.226	D-feed SP and Reactor Level SP
AZ	$x_B(H_2O)$		Reflux flow and 5 th Tray temperature SP

The line

```
\usepackage{tbls}
```

must be inserted in the preamble of your document. The table is set up to be single-spaced by

```
\renewcommand{\baselinestretch}{1} \small\normalsize
```

before

```
\begin{table}
```

. I set the first, second, and fourth columns as paragraphs, .5in, 1in, and 2.25in wide, respectively. I then adjusted the separation between the words and the horizontal lines to 5ex by also adding

```
\setlength{\tablinesep}{5ex}
```

before the

```
\begin{table}
```

command.

After typing the table I change the document to be double-spaced from this point on.

1.14 Figures

The figure on the following page is centered and the figure caption is indented and single-spaced. Make sure you copy the last two lines

```
\renewcommand{\baselinestretch}{2}\  
  
\small\normalsize
```

to return to double-spacing of your text.

The first figure is Fig.1.1. Please note that the figure label should be placed inside the figure caption.

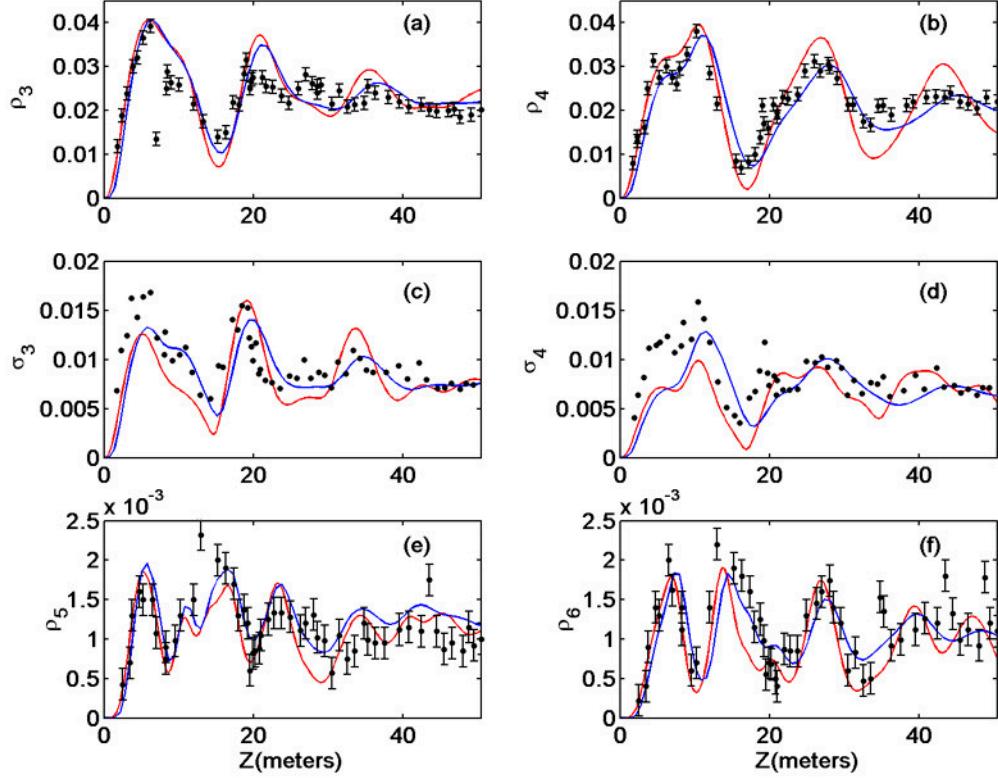


Figure 1.1: This figure caption is indented and single-spaced. Comparison between the experimental measurements [28] (black), the random initial condition NLSE model excluding phase noise (dashed curves) and the stochastic phase noise NLSE model (solid curves) showing the first- and second-order sideband evolution as a function of fiber length for $P_0 = 5.5 \text{ W}$, $\Omega = 366 \text{ GHz}$, $\Delta\nu = 0.5 \text{ GHz}$, $\gamma = 0.019 \text{ W}^{-1}\text{m}^{-1}$, and $\beta^{(2)} = 55 \text{ ps}^2/\text{km}$: dynamical evolution of the: (a) power in the first-order blue-shifted sideband, (b) power in the first-order red-shifted sideband, (c) fluctuations in the first-order blue-shifted sideband, (d) fluctuations in the first-order red-shifted sideband, (e) power in the second-order blue-shifted sideband, (f) power in the second-order red-shifted sideband.

The next figure is placed landscape. It is Fig. 1.2.

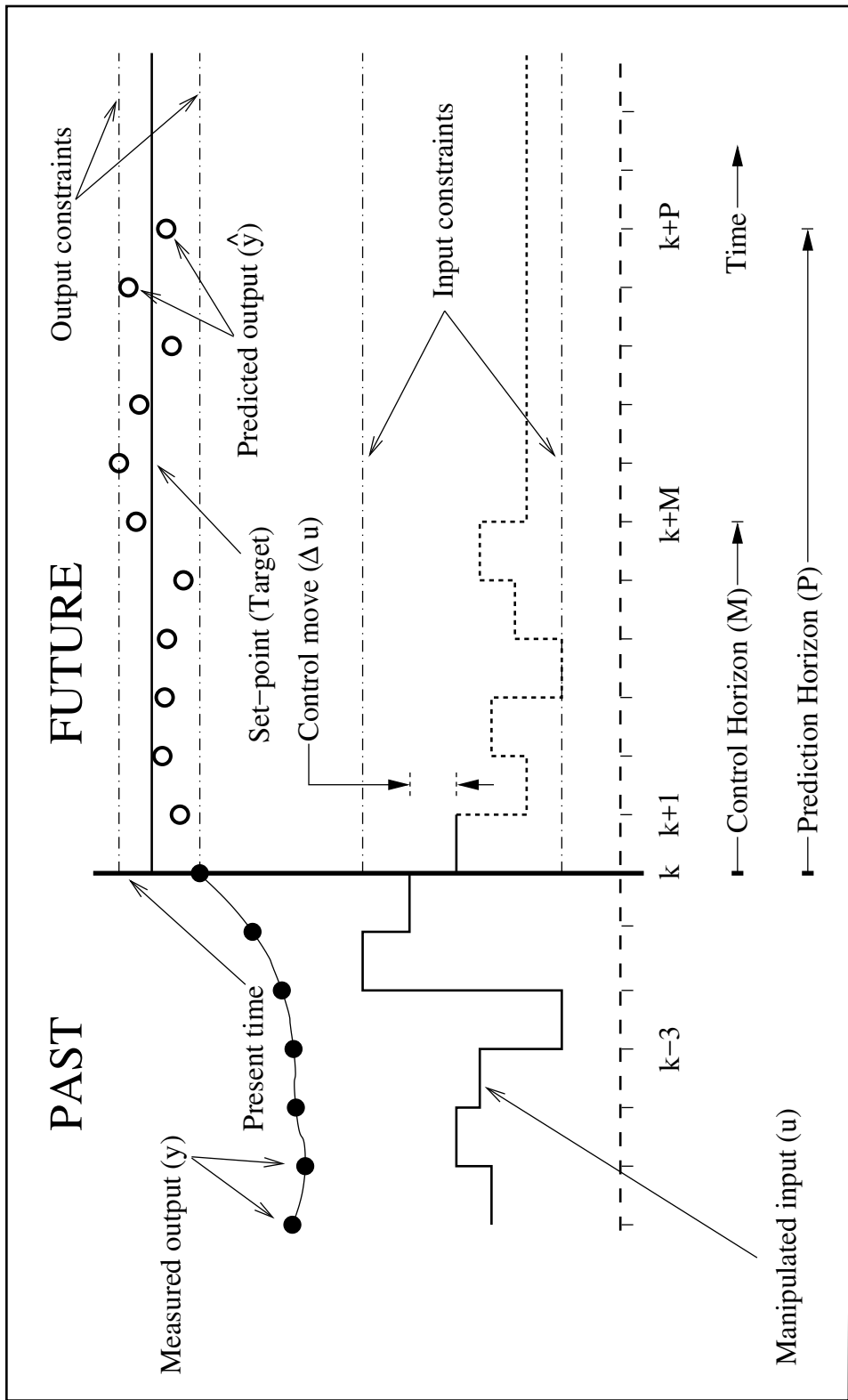


Figure 1.2: Schematic illustrating receding horizon control.

This is a my second figure which was placed landscape. Although I have used the same figure, I have renamed the label to fig:mpc-1. The second figure now becomes Figure 1.3.

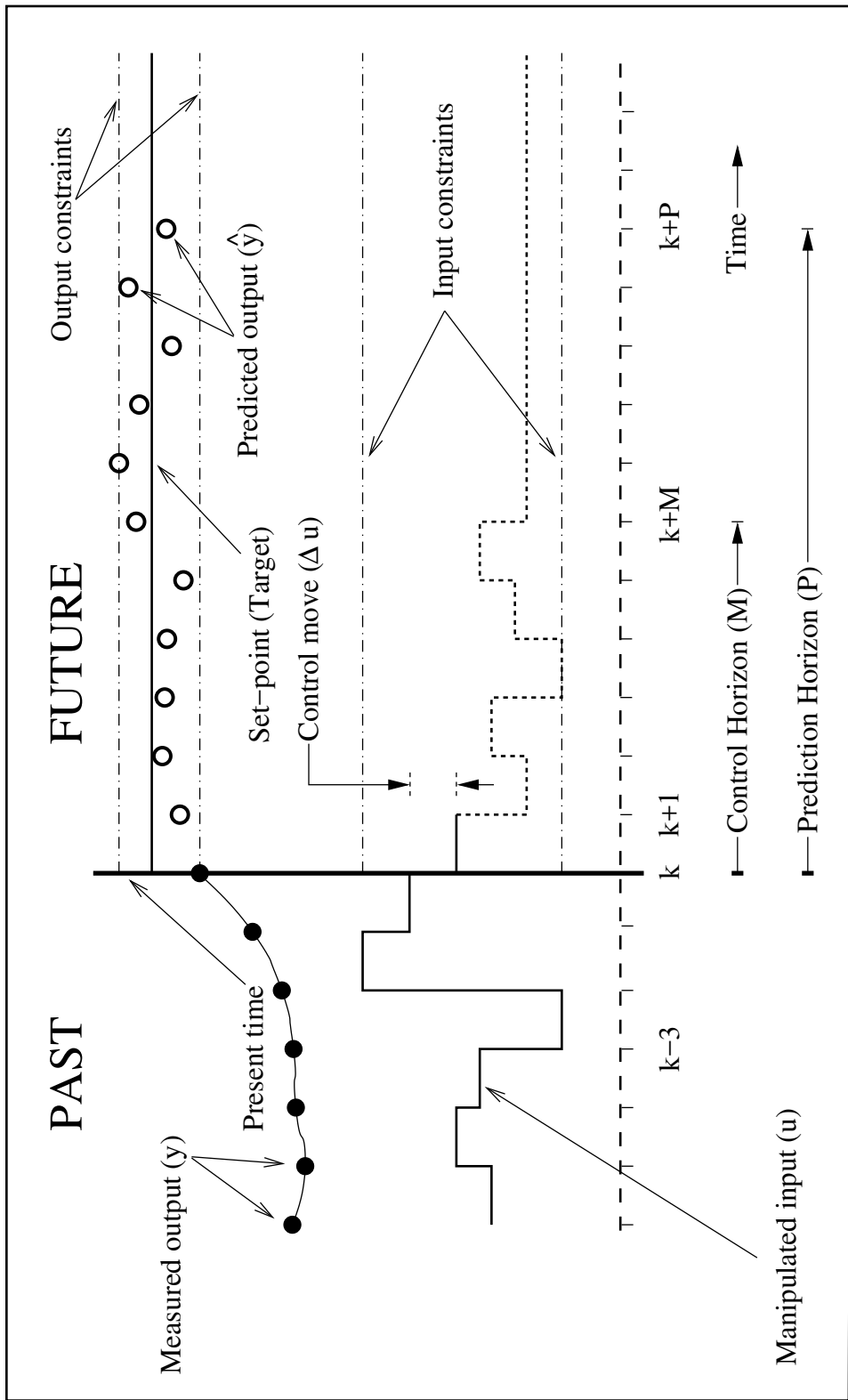


Figure 1.3: Schematic illustrating receding horizon control.

1.14.1 Numbering Figures

If you wish your figures to be numbered 1-100 without any reference to the chapter (e.g., Figure 1.1, 2.1, etc.), change the first line of your mainthesis.tex file to read

```
"\documentclass[12pt]{thesis-2}".
```

1.14.1.1 This is a Subsubsection

This is my first subsubsection in Chapter 1.

1.15 Short Titles in the Table of Contents, List of Figures, or List of Tables

The Table of Contents, List of Figures, or List of Tables usually show the entire title of a section, subsection, etc. or table, or the entire caption of a figure. If you put a short title in square brackets after

```
\section, \table, or \figure,
```

the short title will show in your Table of Contents or lists.

```
\section[Short Title]{Title of Section}  
\subsection[Short Title]{Title of Subsection}
```

or when using a caption in a figure or table

```
\caption[Short Caption]{Full text of the caption.}
```

1.16 Figures on Text Page

Normally figures in the thesis are placed on a page by themselves. The following figure is placed on the page with text before and after the figure by adding `[[!h]` after

```
\begin{figure}[[!h]
```

. Please note that the figure label is placed within the caption.

```
\begin{figure}[[!h]
  \begin{center}
    \includegraphics[width=5in]{mpc}
  \end{center}
  \caption[Short title]{Schematic illustrating receding horizon control.}
  \label{fig:mpc-2}}
\end{figure}
```

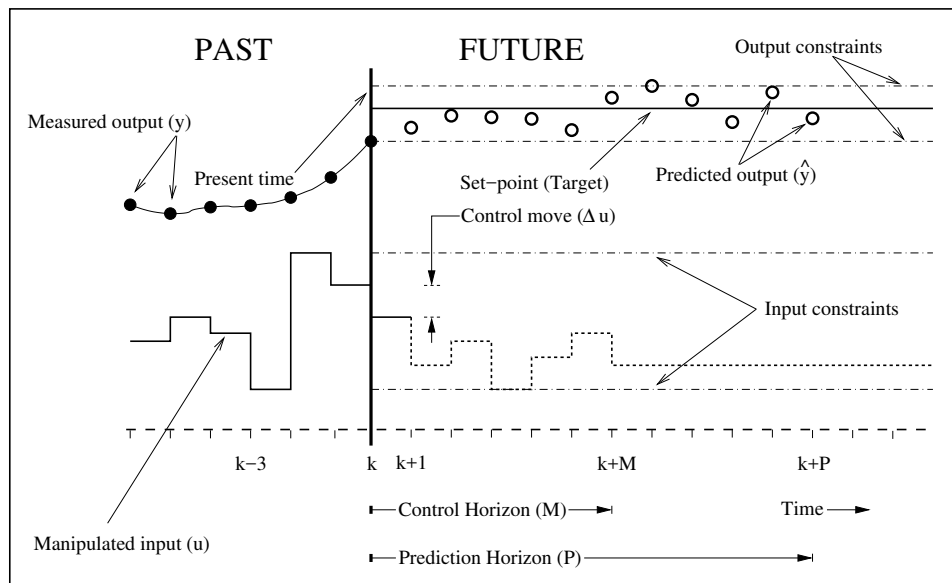


Figure 1.4: Schematic illustrating receding horizon control.

This does not necessarily mean that the text before and after the figure will be exactly what you want. Remember Latex will place the figure where it will fit

on the page the best. The previous figure is Figs. 1.4.

1.17 Wrapping Text around Figure

By way of summary, at the end of the activity, I reminded the class of what we'd done: by considering relatively nearby galaxies whose distance we had measured by some other means, we were able to establish a relationship locally between redshift and distance. By way of summary, at the end of the activity, I reminded the

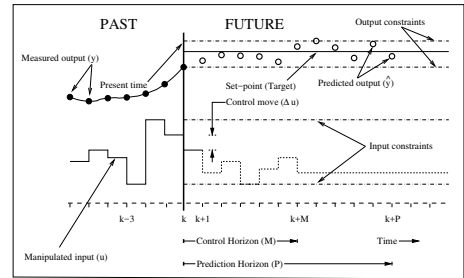


Figure 1.5: Text wrap around figure.

class of what we'd done: by considering relatively nearby galaxies whose distance we had measured by some other means, we were able to establish a relationship locally between redshift and distance. By way of summary, at the end of the activity, I reminded the class of what we'd done: by considering relatively nearby galaxies whose distance we had measured by some other means, we were able to establish a relationship locally between redshift and distance. By way of summary, at the end of the activity, I reminded the class of what we'd done: by considering relatively nearby galaxies whose distance we had measured by some other means, we were able to establish a relationship locally between redshift and distance. See Fig. 1.5.

1.18 LaTeX – A Typesetting Program

A 13-page explanation of some of the features of LaTeX can be downloaded from <http://www.jgsee.kmutt.ac.th/exell/General/LaTeX.html>.

1.19 Using Bibtex

Using Bibtex with Latex documents is not difficult. The bulk of the work is organizing your bibtex file, which is a data base compiled by you of the articles, books, etc. which you use in the bibliographies or reference sections of your publications.

I have linked several files to this webpage, which will be helpful when you are using Bibtex. These files can be downloaded from <http://www.ireap.umd.edu/ireap/theses/bibtex>. Please read the file "BibtexInstructions.pdf". The first two pages explain how to set up and run Bibtex; the remaining pages were taken from a published article and show how the references were cited in the .tex file. The files BibtexInstructions.tex, Galactic.bib, Dottie.bib are the original .tex files used for BibtexInstructions.pdf. The file BibtexSamples.tex contains examples of the information needed for the various publications you wish to reference (e.g., articles in refereed journals, books, unpublished articles, conference proceedings, etc.).

If you have questions concerning Bibtex, please contact me at 301-405-4955 or dbrosius at umd.edu.

1.20 APS Physical Review Style and Notation Guide

The following style guide may be downloaded from The American Physical Society at <http://forms.aps.org/author/styleguide.pdf>: Physical Review Style and Notation Guide, published by The American Physical Society, compiled and edited by Anne Waldron, Peggy Judd, and Valerie Miller, February 1993. It may be old, but it is very useful.

Chapter 2

Stochastic Four-Wave-Mixing

2.1 Overview

The understanding of nonlinear processes in optical fibers is crucial towards extending the capabilities of modern optical communication systems based on wavelength division multiplexing (WDM), where each communication channel is represented by a unique wavelength. One of the nonlinear processes that limits the information carrying capacity of a WDM system is four-wave mixing (FWM), which causes cross-talk between neighboring channels. This places a lower limit on the wavelength separation between adjacent channels and an upper limit on the input power in each channel. In this study, we describe a process by which the evolution of FWM processes in an optical fiber can be used to estimate the inhomogeneities in the fiber core material, in particular the fluctuations in the linear refractive index of the fiber core.

Experiments measuring the evolution of FWM processes along a length of fiber were carried out by Hart *et al.* [28] and are described in detail in Sec. 2.2. In this experiment, two input pump waves at frequencies ω_1 and ω_2 , interacted with each other through the third-order nonlinearity of the fiber material to generate first-order sidebands at frequencies $\omega_3 = 2\omega_1 - \omega_2$ and $\omega_4 = 2\omega_2 - \omega_1$. These waves further interacted to produce second-order sidebands at $\omega_5 = 2\omega_3 - \omega_4$ and $\omega_6 = 2\omega_4 - \omega_3$.

Higher-order sidebands were also generated. The normalized power in the sideband at frequency ω_m was represented by ρ_m . The evolution of the FWM processes was characterized by the evolution of $\rho_m(z)$ as a function of fiber length z .

In the present work, we make a quantitative comparison between these experimental results and our numerical results based on efficient algorithms [8] to solve the nonlinear Schrödinger equation (NLSE) that governs the system. The numerical model, its underlying assumptions and the results are described in Sec. 2.3. A realistic description of a standard single mode optical fiber must take into account the random phase perturbations a light wave undergoes while propagating through it, without disturbing the underlying conservative properties of the system. The NLSE needs to be suitably modified in order to incorporate the stochastic nature of the propagation. In order to preserve the conservative properties of the system, the stochastic terms in the NLSE must necessarily be multiplicative in nature as an additive term acts as a source or a sink. An algorithm that achieves this with linear, Gaussian, δ -correlated noise is outlined in Sec. 2.3. This algorithm preserves the unconditional stability of the system. At the same time, care is taken to transform the stochastic NLSE from its original Ito representation [29] to the computationally feasible Stratanovich representation [30] by compensating for the spurious linear drift that results from integrating such stochastic differential equations [31, 32, 33, 34]. The dominant sources of phase noise are discussed in Sec. 2.4.

Conclusions on the relevance of the experiments of Hart *et al.* [28] and the stochastic modeling presented here are summarized in Sec. 2.5.

2.2 Experimental and Computational Background

In this work, we focus on tracing the evolution of the sidebands, generated through FWM, along a length of optical fiber. The FWM spectral evolution along 50 m of fiber for two input pump power regimes (2.1 W and 5.5 W) was investigated [28]. In the 2.1 W case, the sideband evolution followed a damped sinusoid along the length of the fiber. The experiments also found that the two first-order sidebands (ρ_3 -blueshifted and ρ_4 -redshifted from the two pumps) had different evolutions along the fiber (with different spatial wavelengths). For the 5.5 W case, the evolution of both first- and second-order sidebands was measured. The damping in the first-order sidebands (ρ_3 and ρ_4) occurred faster than in the 2.1 W case. Experiments probing the dependence of the sideband power on the input power (ranging from 2 W to 17 W) were also performed at a fixed output length of 50 m of the fiber. At the same fiber length, the optical spectra for input powers ranging from 2 W to 17 W were also recorded [28]. The spectral envelopes were observed to fit well to a hyperbolic secant function and the fit parameters were recorded. Measurements with a high-resolution wavemeter showed that one of the two pumps consisted of two very closely spaced longitudinal modes ($\Delta\nu \sim 0.5$ GHz) which were not resolved by the spectrometer used to record the FWM spectra. Inclusion of this multimode nature of the pump input in their model was found to alter the sideband dynamics dramatically and partly explained the asymmetry between the blue-shifted and red-shifted sidebands though it did not account for the damping in the sidebands. This was accounted for by adding weak phase fluctuations to the waves as they propagated

along the fiber [28]. The physical source of these phase fluctuations was not known at that time. However, the inclusion of the phase fluctuations into the model gave excellent qualitative and quantitative agreement with experiment. Their model involved integration of a system of coupled ODEs derived from the NLSE [35] by a process of truncation that retained only the leading frequency components (the pumps and the first- and second-order sidebands), a process justified by the fact that the input pump waves are well approximated by a combination of monochromatic waves. Their final numerical results are based on simulations using the truncated-ODE model with Langevin noise terms representing phase fluctuations in the fiber. Another physical source of stochasticity in their experiment was the inherent power fluctuation in the lasers used as the input pumps. The level of fluctuations (5-20%) was measured and incorporated appropriately into their model through stochastic initial conditions. This explained the evolution of the level of observed fluctuations in the sideband trajectories although it was found to be inadequate by itself, to account for the damping of the trajectories. They found that all three physical characteristics mentioned above, namely the multimode nature of the pump input, the stochastic phase fluctuations along the length of the fiber, and the stochastic initial power fluctuations were crucial to explaining the different features of the experimental measurements [28].

2.3 Stochastic NLSE Model

In the present work, we have developed and implemented an unconditionally stable scheme for integrating the NLSE that successfully incorporates phase noise into the SSFM. Thus, we are now in a position to harness the high frequency / time resolution of the SSFM together with its efficient convergence properties. Due to these advances, we are now able to do simulations with much higher frequency resolution (60 MHz as compared to 300 GHz in the ODE model). This high resolution, coupled with an appropriate convolution scheme, enables us to compare these simulated spectra with the composite spectra observed by the spectrometers which had a resolution of ~ 60 GHz. This was not possible with the truncated ODE model as the resolution of the simulated spectra in that case was ~ 300 GHz. For exactly the same levels of phase fluctuations, and initial condition fluctuations as used in Ref. [28], comparisons for the present NLSE model with the experimental sideband evolution functions $\rho_i(z)$ show excellent quantitative agreement. These results, along with the algorithms employed, are described in detail in this section. We have identified linear refractive index fluctuations along the fiber length to be a strong candidate for a physical source of the stochastic phase fluctuations. A comparison between the various possible sources is given in Sec. 2.4.

Under the assumption that the electric field of the light in the fiber has a slowly varying envelope $A(z, \tau)$, and that the fiber medium has an instantaneous nonlinear response, the system is well described by the nonlinear Schrödinger equation (NLSE)

with a linear multiplicative stochastic term

$$\frac{\partial U}{\partial z} + \frac{i\beta^{(2)}}{2T_0^2} \frac{\partial^2 U}{\partial \tau^2} + \frac{\alpha U}{2} + i\Gamma(z, \tau)U - i\gamma P_0 |U|^2 U = 0. \quad (2.1)$$

Z is distance along the length of the fiber, $U(z, \tau) = A(z, \tau)/\sqrt{P_0}$ is the complex electric field envelope $A(z, \tau)$ normalized to the absolute amplitude of the field $\sqrt{P_0}$, P_0 is the total power in the fiber, τ is time normalized to a convenient time scale T_0 (~ 1 ns) measured in a reference frame moving with the group velocity of the pulse [$\tau = (t - z/v_g)/T_0$]. The simulations are carried out for exactly the same physical parameters as the experiments and simulations reported by Hart *et al.* [28], i.e., $\beta^{(2)} = 55$ (ps)²/km, is the group velocity dispersion of the fiber at the operating wavelength $\lambda_0 \sim 632$ nm ($k_0 \sim 10^7$ m⁻¹). A loss of ~ 6 dB/km gives $\alpha = 0.0014$ m⁻¹ as the loss in the fiber at this wavelength. The nonlinearity coefficient $\gamma = 0.019$ W⁻¹m⁻¹ is given by

$$\gamma = \frac{\omega_{ave} n_2^I}{c A_{eff}}, \quad (2.2)$$

where A_{eff} is the effective core area of the fiber, n_2^I is the Kerr coefficient for the intensity-dependent refractive index, and ω_{ave} is the average angular frequency of the wave envelope. $\Gamma(z, \tau)$ is a linear multiplicative phase noise field. In this study the noise field is assumed to be δ -correlated in both space and time. The evolution of the FWM dynamics is found to be sensitive to the strength of this noise field. It can be physically interpreted as phase noise arising due to fluctuations in the linear refractive index of the fiber medium. A detailed discussion of its physical origin is given in Sec. 2.4.

The system was simulated using the Split-Step Fourier Method (SSFM) [8].

An algorithm for appropriately incorporating stochastic phase fluctuations along the length of the fiber in the SSFM was developed and is summarized below.

The NLSE is composed of linear and nonlinear terms, and can be written in operator form as

$$\begin{aligned}
\frac{\partial U}{\partial z} &= (\hat{D} + \hat{S} + \hat{N})U \\
\hat{D} &= \frac{-i\beta^{(2)}}{2T_0^2} \frac{\partial^2}{\partial \tau^2} - \frac{\alpha}{2} \\
\hat{S} &= i\Gamma(z, \tau) \\
\hat{N} &= i\gamma P_0 |U|^2,
\end{aligned} \tag{2.3}$$

where \hat{D} , \hat{S} and \hat{N} are linear (dispersive), nonlinear and stochastic operators, respectively. It has an exact solution for infinitesimal Δz given by -

$$U(z + \Delta z, \tau) = \exp[\Delta z(\hat{D} + \hat{S} + \hat{N})]U(z, \tau), \tag{2.4}$$

which can be approximated by

$$U(z + \Delta z, \tau) \approx \exp[\Delta z \hat{D}] \exp[\Delta z \hat{S}] \exp[\Delta z \hat{N}] U(z, \tau). \tag{2.5}$$

The execution of $\exp[\Delta z \hat{N}]$ is carried out in τ -space:

$$B_1(z, \tau) = \exp[\Delta z \hat{N}] U(z, \tau). \tag{2.6}$$

The execution of $\exp[\Delta z \hat{S}]$ and $\exp[\Delta z \hat{D}]$ is carried out in ω -space.

In particular, the stochastic phase fluctuations are introduced by modifying the phase ϕ_j of each frequency component ω_j of the complex field according to

$$\begin{aligned}
B_2(z, \omega) &= \mathcal{F}[B_1(z, \tau)] \\
B_3(z, \omega_j) &= \exp[i\delta\phi(z, \omega_j)] B_2(z, \omega_j),
\end{aligned} \tag{2.7}$$

where \mathcal{F} represents the Fourier transform operation.

This process only modifies the phase of each complex frequency component, leaving its absolute value unchanged. Thus the algorithm conserves the total power and the unconditional stability of the system.

The stochastic phase fluctuations $\delta\phi(z, \omega_j)$ are taken to be δ -correlated in frequency as well as spatially along the fiber length. The Box-Muller algorithm [36] was used to generate Gaussian random deviates from computer-generated uniform random deviates r_{1j} and r_{2j} at each spatial step and for each frequency component ω_j . The fluctuations are given by

$$\delta\phi(z, \omega_j) = \sqrt{-2\sigma_\phi^2 \Delta z \ln(r_{1j})} \cos(2\pi r_{2j}). \quad (2.8)$$

This is followed by the execution of $\exp[\Delta z \hat{D}]$, which is also carried out in Fourier space, followed by the inverse transform

$$U(z + \Delta z, \tau) = \mathcal{F}^{-1}[\exp[\Delta z \hat{D}(i\omega)] B_3(z, \omega)]. \quad (2.9)$$

$\hat{D}(i\omega)$ is obtained by replacing $(\partial/\partial\tau)$ by $i\omega$.

The basic form of the initial complex wave envelope function is

$$U(0, \tau) = \exp\left(-\frac{\tau^2}{2\tau_p^2}\right) \left\{ \begin{array}{l} \exp\left(\frac{i\Omega\tau}{2}\right) + \\ \exp\left(-\frac{i\Omega\tau}{2}\right) \end{array} \right\}, \quad (2.10)$$

where τ_p is the pulse width $T_p = 5$ ns FWHM, normalized to the time scale T_0 , $\Omega = 366$ GHz is the frequency detuning between the two laser sources normalized to a frequency scale $\Omega_0 = 62.5$ MHz. Figure 2.1(a) shows a plot of this pulse $|U(0, \tau)|^2$. The overall Gaussian envelope has an FWHM of 5 ns, the closely spaced dark lines

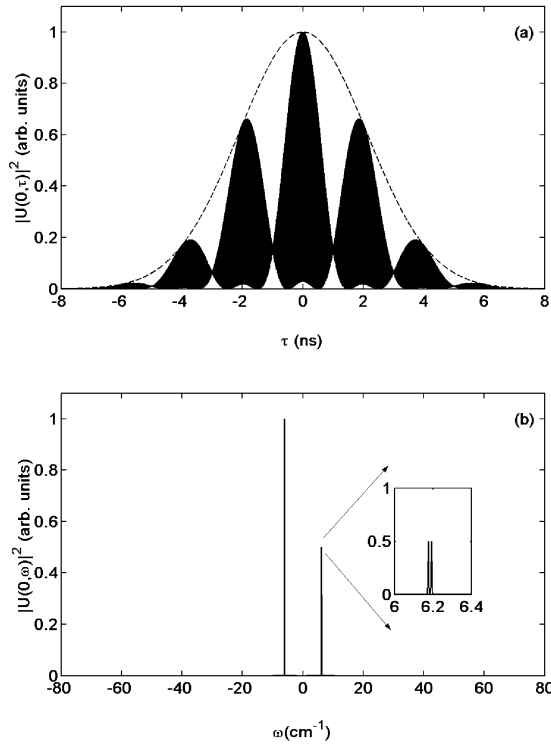


Figure 2.1: Multimode pulse input to the NLSE: (a) input pulse in time domain and (b) input spectrum.

are due to the 366 GHz (~ 3 ps) beating between the two input pump frequencies. The 2 ns modulations on the pulse are due to the 0.5 GHz mode-structure in the blue-shifted pump wave. Figure 2.1(b) shows the input spectrum of this pulse which consists of two highly monochromatic pump waves with a detuning of $\Omega=366$ GHz. The spectrum of the blue-shifted pump, upon magnification, is seen to be composed of two very closely spaced peaks, with a separation of $\Delta\nu=0.5$ GHz. Hart *et al.* [28] did not use pulsed wave functions in their NLSE simulations as the size of the FFT required to do so made it computationally prohibitive at that time. The size of the FFT was chosen such that it would accommodate a time span of 16 ns in order to go sufficiently far into the wings on the Gaussian pulse; and a frequency span of 16 THz in order to accommodate all the sidebands generated and prevent spurious effects due to the reflection boundary conditions implicit in the SSFM algorithm. These considerations dictated the size of the FFT to be $\geq(16 \text{ THz})\cdot(16 \text{ ns}) = 256000$. The nearest power of 2 is $2^{18} = 262144$, which has been used throughout the present work. The incorporation of the pulsed nature of the light was found to be necessary in explaining the dynamics. From the perspective of the coupled amplitude equations used by Hart *et al.* [28], the present model is equivalent to a coupled-ODE model with 2^{18} coupled ODEs.

Upon incorporation of the multimode nature of the blue input pump laser source and the stochastic fluctuations in the initial power in the lasers, the initial

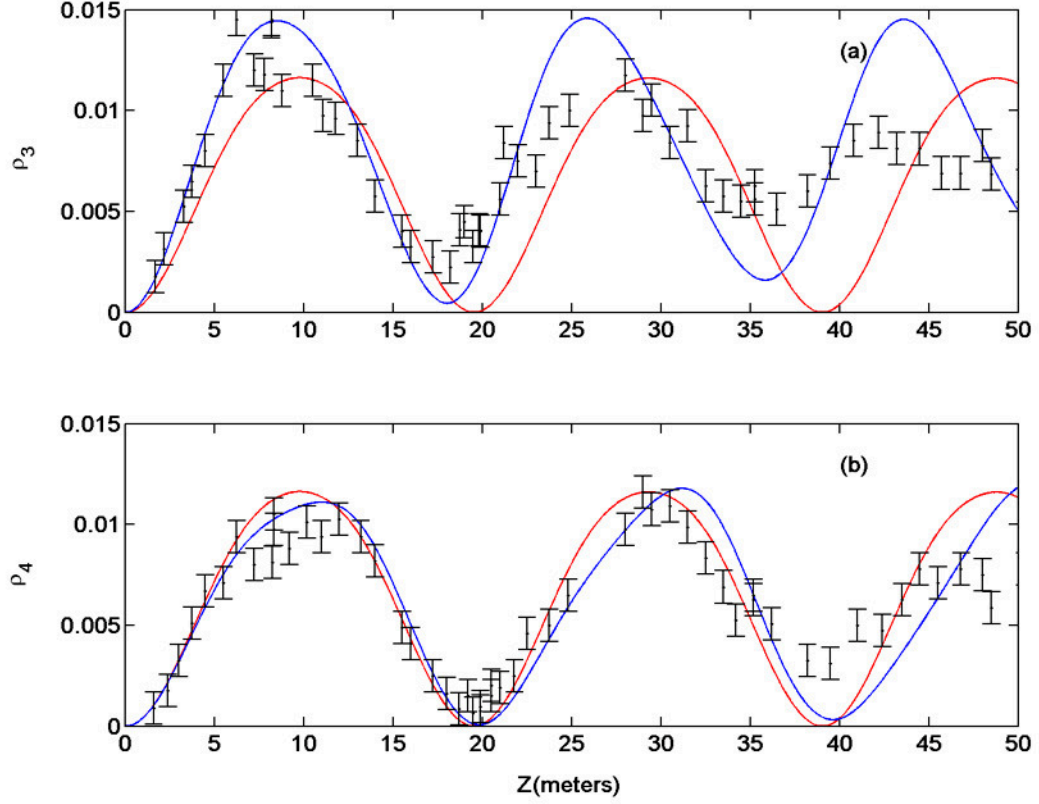


Figure 2.2: Effects of inclusion of the multimode nature ($\Delta\nu = 0.5$ GHz) of the blue-shifted input pump laser on the 1st order sideband evolution as a function of fiber length for $P_0 = 2.1$ W. Dashed curves represent simulations without the multimode nature and solid curves represent simulations with the multimode nature. $\Omega = 366$ GHz, $\gamma = 0.019$ W⁻¹ m⁻¹, and $\beta^{(2)} = 55$ ps²/km (a) power in the blue-shifted sideband, (b) power in the red-shifted sideband.

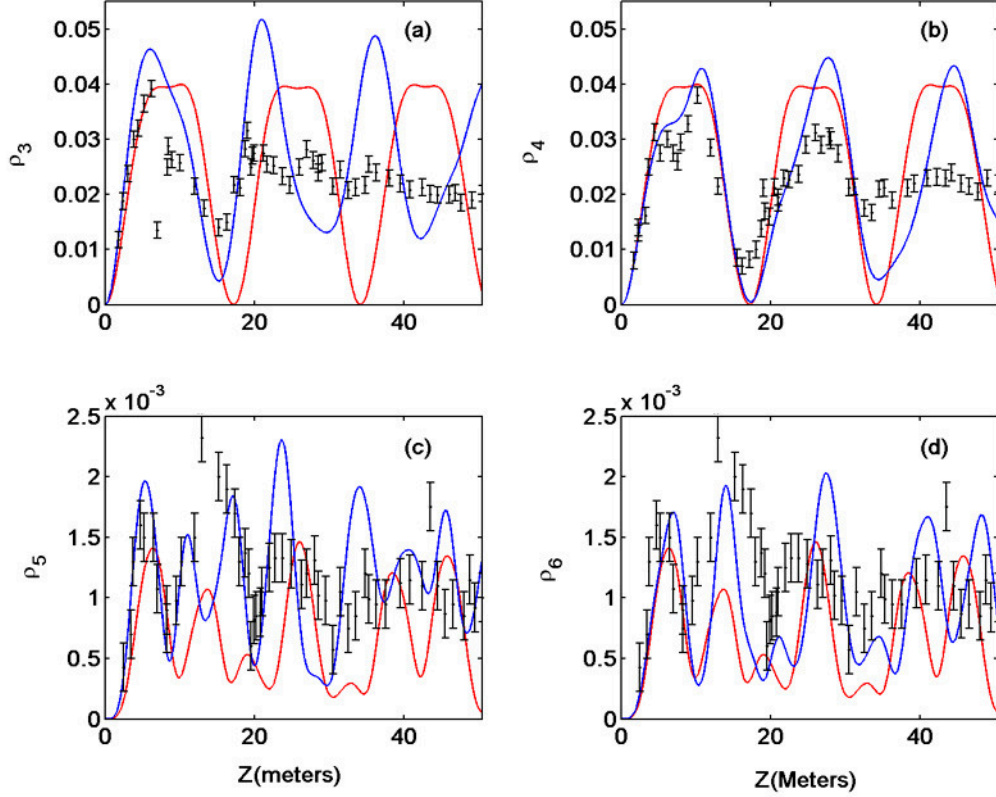


Figure 2.3: Effects of inclusion of the multimode nature ($\Delta\nu = 0.5$ GHz) of the blue-shifted input pump laser on the 1st order sideband evolution as a function of fiber length for $P_0 = 5.5$ W. Dashed curves represent simulations without the multimode nature and solid curves represent simulations with the multimode nature. $\Omega = 366$ GHz, $\gamma = 0.019$ W $^{-1}$ m $^{-1}$, and $\beta^{(2)} = 55$ ps 2 /km (a) power in the first-order blue-shifted sideband, (b) power in the first-order red-shifted sideband, (c) power in the second-order blue-shifted sideband, (d) power in the second-order red-shifted sideband.

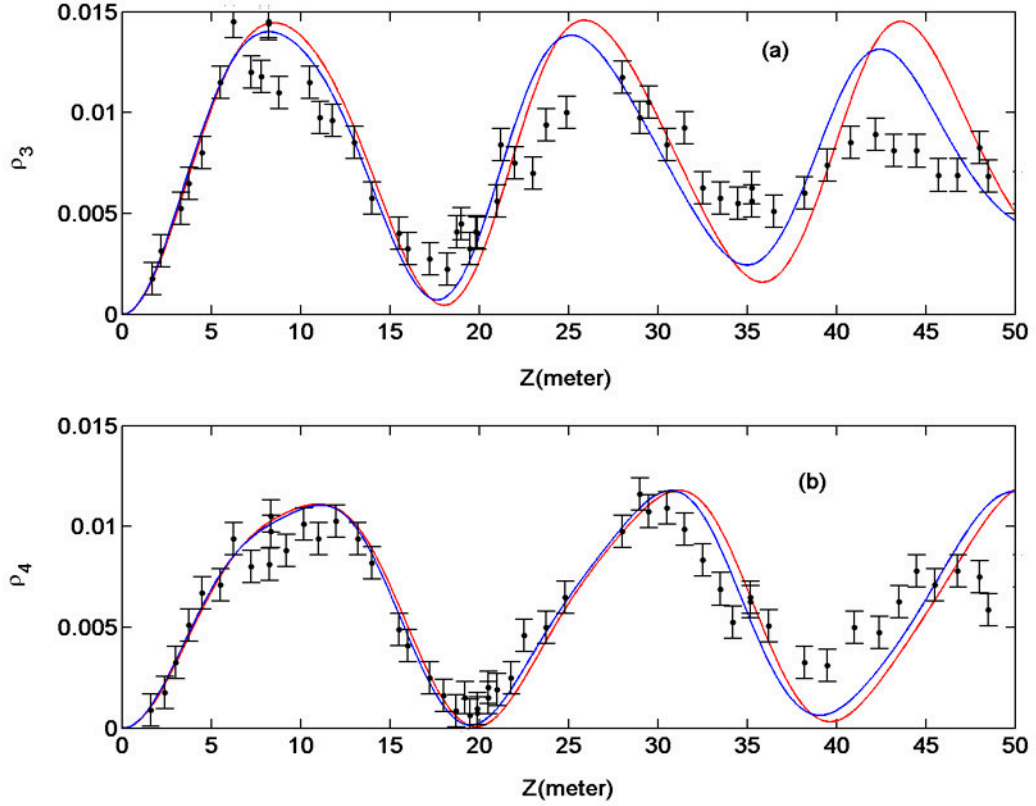


Figure 2.4: Effects of inclusion of the pulsed nature (5 ns FWHM) of the input pump laser light on the first-order sideband evolution as a function of fiber length for $P_0 = 2.1$ W. Dashed curves represent cw simulations and solid curves represent pulsed simulations. $\Omega = 366$ GHz, $\Delta\nu = 0.5$, $\gamma = 0.019$ W $^{-1}$ m $^{-1}$, and $\beta^{(2)} = 55$ ps 2 /km (a) power in the blue-shifted sideband, (b) power in the red-shifted sideband.

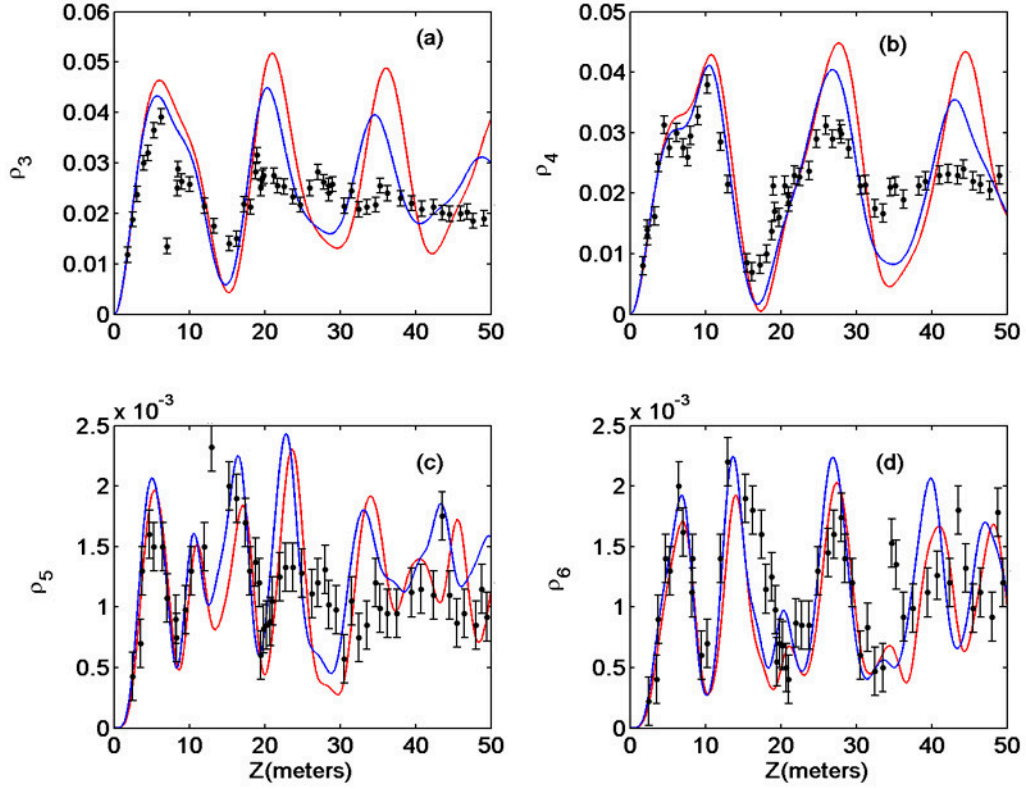


Figure 2.5: Effects of inclusion of the pulsed nature (5 ns FWHM) of the input pump laser on the first- and second-order sideband evolution as a function of fiber length for $P_0 = 5.5$ W. Dashed curves represent cw simulations and solid curves represent pulsed simulations. $\Omega = 366$ GHz, $\Delta\nu = 0.5$, $\gamma = 0.019$ W $^{-1}$ m $^{-1}$, and $\beta^{(2)} = 55$ ps 2 /km (a) power in the first-order blue-shifted sideband, (b) power in the first-order red-shifted sideband, (c) power in the second-order blue-shifted sideband, (d) power in the second-order red-shifted sideband.

wave function takes the form

$$U(0, \tau) = \exp\left(-\frac{\tau^2}{2\tau_p^2}\right) \left\{ \begin{array}{l} \sqrt{\frac{1+\delta\rho_1}{2}} \left[\begin{array}{l} \exp\left(\frac{i(\Omega+\Delta\nu)\tau}{2}\right) + \\ \exp\left(\frac{i(\Omega-\Delta\nu)\tau}{2}\right) \end{array} \right] \\ + \sqrt{1+\delta\rho_2} \exp\left(-\frac{i\Omega\tau}{2}\right) \end{array} \right\}. \quad (2.11)$$

$\Delta\nu = 0.5$ GHz is the frequency separation between the two longitudinal modes in the blue-shifted pump. $\delta\rho_1$ and $\delta\rho_2$ are Gaussian random deviates (generated using the Box-Muller algorithm [36]) that represent the initial power fluctuations in each of the pump laser sources. Their standard deviations were taken to be, $\sigma_{\rho_1} = 0.2$, $\sigma_{\rho_2} = 0.11$ for simulations from 0 m to 20 m, $\sigma_{\rho_1} = 0.12$, $\sigma_{\rho_2} = 0.05$ for simulations from 20 m to 50 m along the length of the fiber. This is exactly the same prescription used by Hart *et al.* [28] in their simulations and is dictated by their experimental measurements of the fluctuations in the pump laser intensities.

At this point it is worth noting the effects of the inclusion of two attributes of the input laser light, namely, the multimode nature of the blue-shifted pump, and the pulsed nature of the input light (assumed to be cw in the simulations reported by Hart *et al.* [28]).

Figure 2.2 shows a comparison between simulations with (solid curves) and without (dashed curves) the multimode nature for an input pump power of 2.1 Watts. The simulations with the mode structure show the asymmetry between the blue- and red-shifted sideband evolution, in particular, the difference in spatial wavelength between the two, and a non-return to zero nature of the evolution, as observed in the experimental data (black dots with error bars). These features are

absent in the simulations without mode-structure. ρ_3 and ρ_4 stands for the first order blue- and red-shifted sidebands respectively. Figure 2.3 shows the corresponding comparison for the case of 5.5 Watts of input pump power. Here, too, the simulations incorporating the multimode nature of the blue-shifted pump (solid curves) are seen to be an improvement over those not incorporating it (dashed curves). A feature of the experimental data (black dots with errorbars) is that for the ρ_3 sideband, the initial part of the evolution involves a peak followed by a shoulder, while for the ρ_4 sideband, the initial part of the evolution involves a shoulder followed by a peak. This feature, too, is seen to occur as a result of the inclusion of the multimode nature of the blue-shifted pump.

The effect of inclusion of the pulsed nature of the input beam is seen in Fig. 2.4 (for the 2.1 Watt case) and Fig. 2.5 (for the 5.5 Watt case). The solid dashes represent simulations for a cw input beam and the solid curves represent those for a pulsed input beam. The incorporation of the pulsed nature clearly results in damping of the sideband trajectories which are seen to come closer to the experimental data [28] (black dots with error bars).

Use of the FFT algorithm makes evaluation relatively fast compared to other finite-difference schemes. The computational error is $O(\Delta z^2)$, thus the solution converges with decreasing spatial step-size Δz .

The simulations were tested for the conservation of total power along the fiber length (by setting the loss α to zero) and for the conservation of asymmetry [35, 28]

given by

$$C(Z) = \sum_{i=1}^{\infty} (2i - 1) [\rho_{2i-1}(Z) - \rho_{2i}(Z)]. \quad (2.12)$$

A clearer picture of the evolution of the sidebands is obtained by plotting both the power in the sidebands and their standard deviations as a function of length along the fiber. Figures 2.6(a) and 2.6(b) show a comparison between simulation and experiment of the evolution of the first-order blue-shifted (ρ_3) and red-shifted (ρ_4) sidebands, respectively, for an input power of 2.1 W. The dashed curves represent NLSE simulations which include the stochastic nature of the input powers of the pump lasers but exclude the stochastic phase fluctuations added along the length of the fiber, an attribute which is included in the simulations represented by the solid curves. The black dots with error bars represent the experimental data. The measured sideband power, normalized to the total power in the fiber, is periodic in length but appears to be damping to a constant value. The measured data also show a clear difference between the spatial wavelengths of oscillation of the blue-shifted (ρ_3) and red-shifted (ρ_4) sidebands trajectories, respectively. Both these features are captured well by both the simulations. Figures 2.6(c) and 2.6(d) compare experimental and simulated measures of the evolution of the standard deviation in the sideband power along the fiber length. It is clearly observed that simulations with phase noise added to the light field along the length of the fiber (solid curves) are closer to the experimental data as compared to those that exclude this feature (dashed curves). This indicates the instrumental nature of the phase fluctuations in explaining key features of the dynamics.

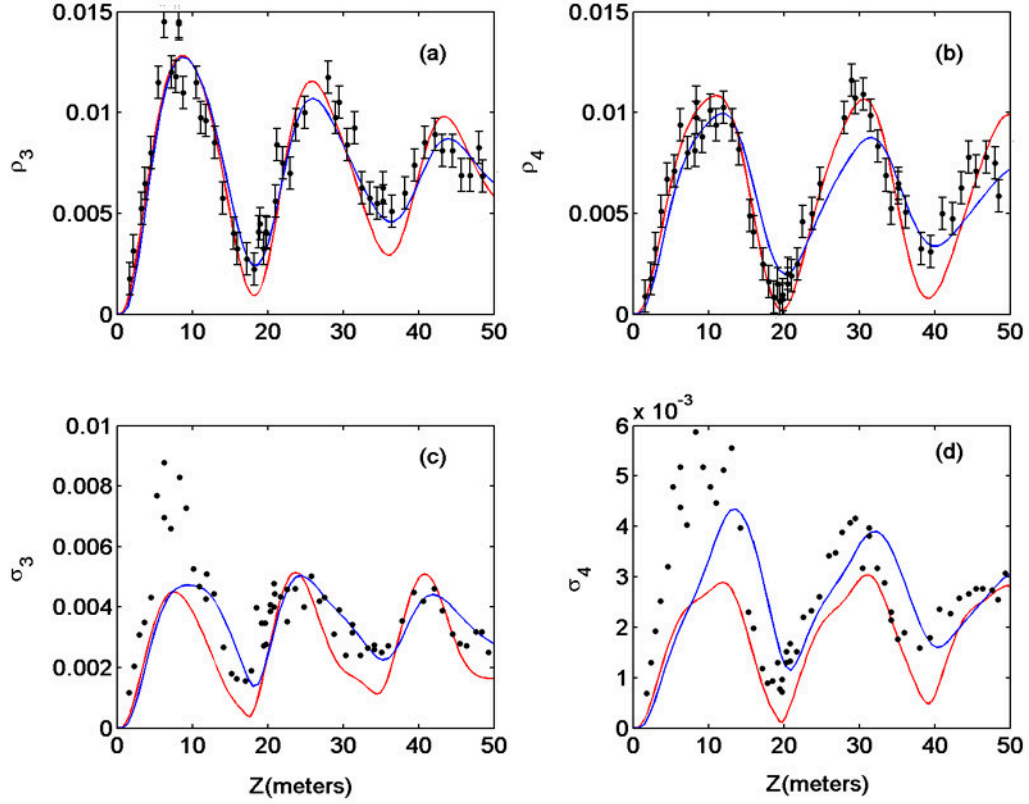


Figure 2.6: Comparison between the experimental measurements [28](black), the random initial condition NLSE model excluding phase noise (dashed curves) and the stochastic phase noise NLSE model (solid curves) showing the first-order sideband evolution as a function of fiber length for $P_0 = 2.1 \text{ W}$, $\Omega = 366 \text{ GHz}$, $\Delta\nu = 0.5 \text{ GHz}$, $\gamma = 0.019 \text{ W}^{-1}\text{m}^{-1}$, and $\beta^{(2)} = 55\text{ps}^2/\text{km}$: dynamical evolution of the: (a) power in the blue-shifted sideband, (b) power in the red-shifted sideband, (c) fluctuations in the blue-shifted sideband, (d) fluctuations in the red-shifted sideband.

The apparent damping of the periodic sideband trajectory is seen more dramatically in Figs. 2.7(a) and 2.7(b), which show the evolution of the first-order sideband power along the fiber for an input power of 5.5 W. The two first-order sidebands evolve differently. They appear to damp to a constant value at a faster rate than for the case with an input pump power of 2.1 W. Here again, NLSE simulations that incorporate phase noise along the length of the fiber (solid curves) are much more successful in accurately capturing the dynamical features of the system than NLSE simulations that do not take this feature into account (dashed curves). Figures 2.7(c) and 2.7(d) show a comparison between the simulated and measured standard deviations. Comparisons for the second-order blue-shifted (ρ_5) and red-shifted (ρ_6) sidebands, respectively, are shown in Figs. 2.7(e) and 2.7(f).

The observed dynamical evolution of the sidebands is found to depend sensitively on the strength of the stochastic phase fluctuations. Yet, best agreement with the experimental results of Hart *et al.* [28] is achieved with exactly the same noise strength σ_ϕ^2 as used in their truncated ODE model, namely, $\sigma_\phi^2 = 0.0067 \text{ m}^{-1}$. They report that including phase noise in their FWM calculations resulted in a spurious linear drift in the trajectories for the sideband power with length. To remove this artifact of the computations, they added a linear loss to their coupled ODEs. They set the loss coefficient $\alpha = 0.0046 \text{ m}^{-1}$ by finding the value that removed this increasing slope. We have observed exactly the same secular growth phenomenon for a wide range of the noise strength σ_ϕ^2 and have arrived at an empirical prescription for α namely, $\alpha \sim \sigma_\phi^2$, where σ_ϕ^2 is the variance of the added phase noise. This indicates the general nature of dynamics resulting from the addition of stochastic,

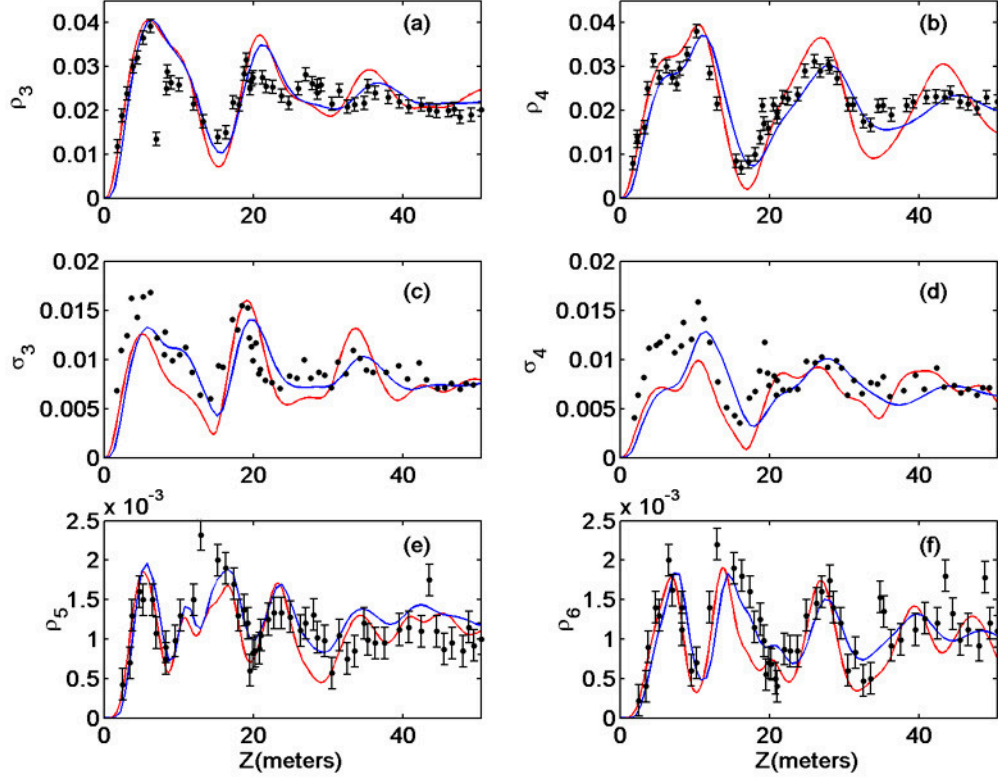


Figure 2.7: This figure caption is indented and single-spaced. Comparison between the experimental measurements [28] (black), the random initial condition NLSE model excluding phase noise (dashed curves) and the stochastic phase noise NLSE model (solid curves) showing the first- and second-order sideband evolution as a function of fiber length for $P_0 = 5.5$ W, $\Omega = 366$ GHz, $\Delta\nu = 0.5$ GHz, $\gamma = 0.019$ W $^{-1}$ m $^{-1}$, and $\beta^{(2)} = 55$ ps 2 /km: dynamical evolution of the: (a) power in the first-order blue-shifted sideband, (b) power in the first-order red-shifted sideband, (c) fluctuations in the first-order blue-shifted sideband, (d) fluctuations in the first-order red-shifted sideband, (e) power in the second-order blue-shifted sideband, (f) power in the second-order red-shifted sideband.

δ -correlated phase fluctuations to systems governed by nonlinear partial differential equations [31].

It is remarkable that the strength of the phase noise required is the same in both the 2.1 W and the 5.5 W cases. Further, it is worth noting that exactly the same noise strength was used by Hart *et al.* [28], the difference being that they introduced phase noise only in the pump frequencies, whereas we have introduced it in all the Fourier modes ($\sim 2^{18}$). As a confirmation of this result, they also performed experiments and numerical simulations examining the sideband power dependence on the input power at a fixed length of 50.4 m of the same fiber. We have repeated these simulations with the stochastic NLSE model and the results are shown in Figs. 2.8(a) (blue-shifted sideband) and 2.8(b) (red-shifted sideband). The experimental measurements of the sideband powers are represented by filled squares and the results of numerical simulations are represented by triangles (without phase noise) and by circles (with phase noise). The simulations are seen to follow the general trend seen in the experiments. As the pump power is increased, the triangles (without phase noise) start to disagree with experiment, whereas the circles (with phase noise) are much closer to experiment. The phase noise strength used in these simulations was exactly the same as that used in the simulations depicted in Figs. 2.6 and 2.7. The agreement between the phase noise simulations and the experimental data was (once again) highly sensitive to the noise strength. Since this experiment (unlike those shown in Figs. 2.2 - 2.7) is non-destructive, it can be used to deduce the strength of phase noise processes in a given optical fiber. It will be shown in Sec. 2.4 that a likely cause of the phase noise is fluctuation in the linear refractive

index of the fiber. The noise strength deduced from the present computational study corresponds to a refractive index inhomogeneity of $\langle \Delta n^2 \rangle \sim 10^{-16}$.

Till now the comparisons between our simulations of the full NLSE and the truncated ODE model give basically the same results, although with much better agreement with experiment. However, the full NLSE can also provide a detailed comparison with the experimental spectra. This was not available from the truncated ODE model. The simulations reported in this work were carried out with a very high frequency and time resolution in order to incorporate the fact that the input light was not cw, but was composed of ~ 5 ns long pulses; and that the number of sidebands generated required the frequency spread of the FFT to be ~ 16 THz, while resolving a longitudinal mode-structure of $\Delta\nu \sim 0.5$ GHz. The spectral resolution used was ~ 0.05 GHz, whereas the spectrometer used to observe the spectra had a resolution 1000 times larger (~ 50 GHz). To account for this difference, the simulated spectra were first convolved with a Gaussian of unit peak and 62 GHz FWHM, before they were compared with the observed spectra.

Figures 2.9(a) and 2.9(b) show three-dimensional plots of the average experimental FWM output spectrum along the length of the fiber for input pump powers of 2.1 W and 5.5 W, respectively (courtesy Hart *et al.* [28]). The vertical axis represents the intensity, normalized to the peak power in one of the input pumps, plotted on a logarithmic scale. The pump frequencies are centered on $\pm \Omega/2$ and the fiber length is increasing into the page. Figures 9(c) and 9(d) show the corresponding comparisons based on simulations using the stochastic-NLSE model. The basic features of the spectral evolution are captured by the simulations.

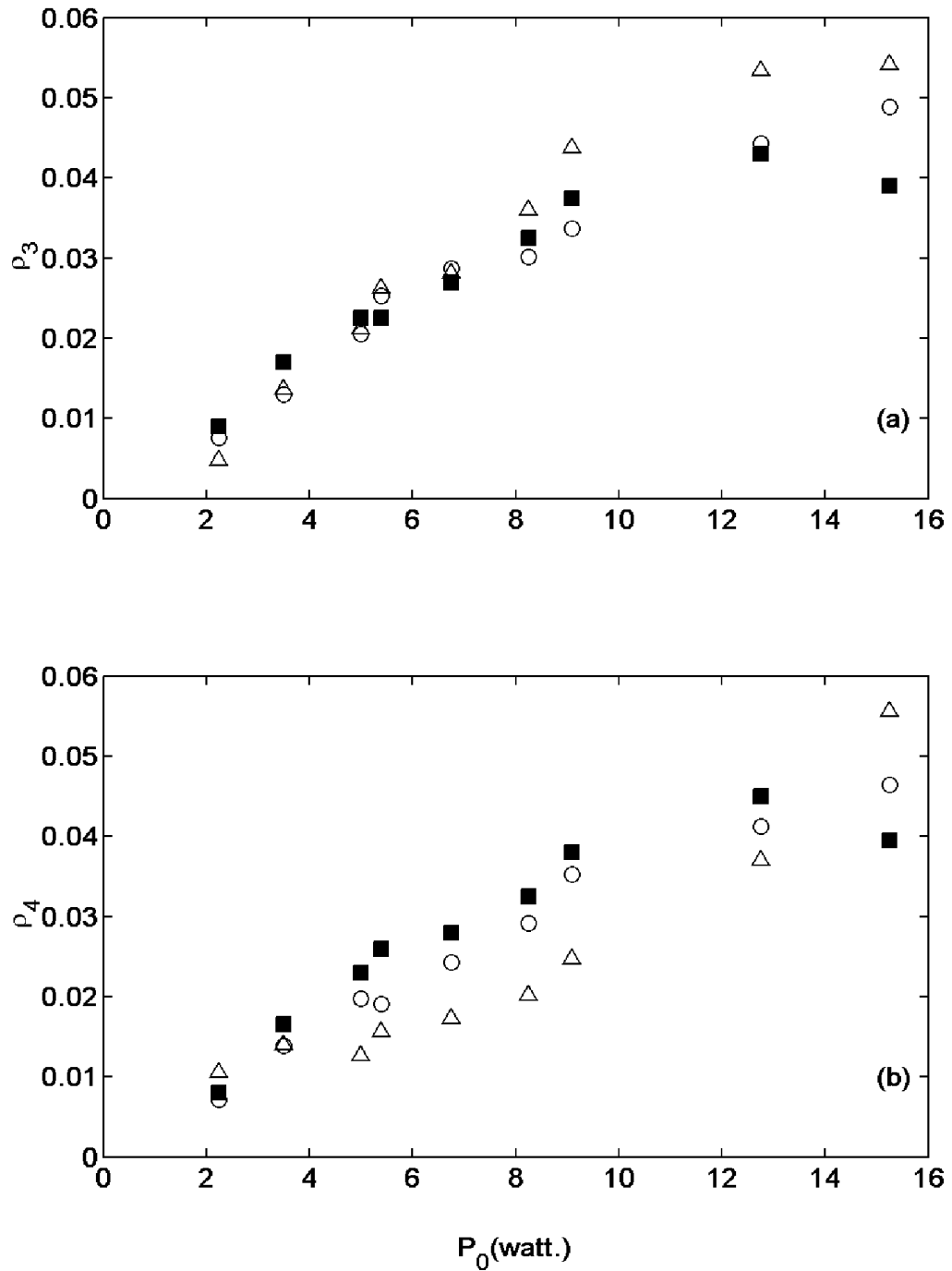


Figure 2.8: Comparison between the experimental measurements (filled squares), simulations without stochastic phase fluctuations (open triangles) and with stochastic phase fluctuations (open circles) of the first-order sideband power versus pump input power for $L=50.39$ m, and $\Omega = 366$ GHz: power in the (a) blue-shifted sideband and (b) red-shifted sideband.

Figure 2.9: Evolution of the FWM spectrum along the fiber (a) $P=2.1$ W, experiment, (b) $P=5.5$ W, experiment, (c) $P=2.1$ W, stochastic-NLSE model, (d) $P=5.5$ W, stochastic-NLSE model.

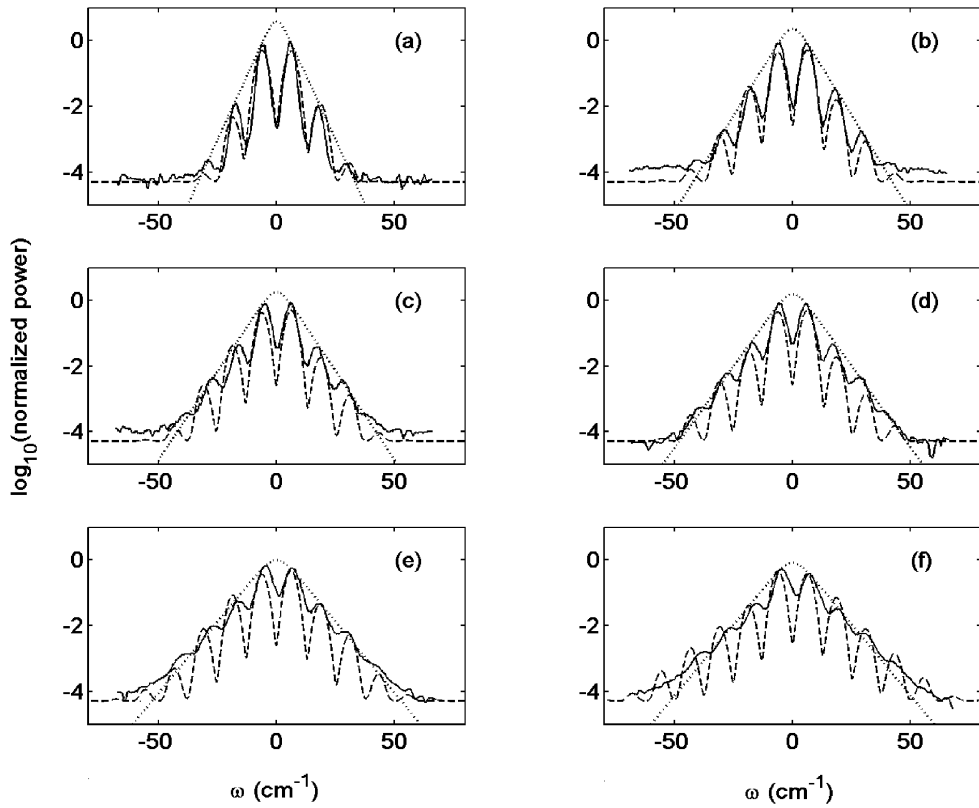


Figure 2.10: Experimental FWM output spectrum (solid line), convolved spectra from simulations of the stochastic NLSE model (dashed line), and hyperbolic secant envelope fit (dotted line) for pump input powers P_0 of (a) 2.1 W, (b) 5.5 W, (c) 6.7 W, (d) 8.3 W, (e) 12.7 W, (f) 17.4 W, fiber length $L=50.39$ m, $\Omega=366$ GHz, $\Delta\nu=0.5$ GHz, $\gamma=0.019$ $\text{W}^{-1}\text{m}^{-1}$, and $\beta^{(2)}=55$ ps^2/km .

Hart *et al.* [28] also documented the experimentally observed FWM output spectra for a fixed fiber length of 50.39 meters for 6 different input pump powers. They state the coefficients A and B of the hyperbolic secant envelopes that best fit the output spectra which are given by

$$f(\omega) = A \operatorname{sech}(B\omega), \quad (2.13)$$

where A and B are the experimental fit parameters.

The hyperbolic secant parameters A and B, that best fit the simulated spectra are exactly the same as those that best fit the experimental spectra [28] for all the 6 cases of input power considered. Figure 2.10 shows an overlap of the simulated spectra (dashed line), with the experimental spectra (solid line) and the experimental hyperbolic secant envelope (dotted line) for 6 different pump powers, namely, (a) 2.1 W, (b) 5.5 W, (c) 6.7 W, (d) 8.3 W, (e) 12.7 W, (f) 17.4 W. The hyperbolic secant parameters for each of these pump powers are (a) A=3.85 and B=0.36, (b) A=2.26 and B=0.27, (c) A=1.81, B=0.25, (d) A=1.56 and B=0.23, (e) A=0.98, B=0.20, and (f) A=0.81 and B=0.20. The exact shapes of the simulated spectra match very well with the experimental spectra for low input pump powers (2.1 W and 5.5 W), but tend to lack the "filled-in" character of the experimental spectra at higher powers (6.7 W, 8.3 W, 12.7 W and 17.4 W).

2.4 Discussion

Hart *et al.* [28] postulated that strong candidates for the possible physical sources of the phase fluctuations are stimulated Brillouin scattering, stimulated

Raman scattering and fiber medium inhomogeneities. Brillouin scattering was eliminated as a source, since a backward propagating wave, which is a signature of Brillouin scattering in optical fibers, was not observed in the experiments. We have modeled stimulated Raman scattering [27, 37] for our system and have found no evidence to support the hypothesis that it could be a possible source of the stochastic phase fluctuations for fiber lengths up to 50 meters and pump power levels up to 5.5 Watts. A more detailed discussion of the Raman scattering simulations performed is given in Chap. 3. Apart from these, quantum phase fluctuations are another well known, though extremely weak, source of phase noise in optical fibers [8, 38].

Fiber medium inhomogeneities were identified as the major cause of the stochastic phase fluctuations. These inhomogeneities can manifest themselves through spatial and/or temporal fluctuations in the fiber parameters, namely, the linear refractive index n_0 , the group velocity v_g , the group velocity dispersion $\beta^{(2)}$ and the nonlinearity γ [39]. Of these, the fluctuation in the linear refractive index was found to be the only source of phase fluctuation that had a significant effect on the dynamics. A relationship between the level of refractive index fluctuations and the corresponding level of phase fluctuations has been arrived at. It is found that refractive index fluctuations as small as $\sigma_n^2 \sim 10^{-17} \text{ m}^{-1}$ can cause the desired phase fluctuations. Possible sources of these refractive index fluctuations are discussed below.

Consider the modified nonlinear Schrödinger equation (NLSE) which is stated below, with the linear multiplicative noise term represented in terms of spatial and

temporal fluctuations in the refractive index of the fiber.

$$\frac{\partial U}{\partial z} + \frac{i\beta^{(2)}}{2T_0^2} \frac{\partial^2 U}{\partial \tau^2} + \frac{\alpha U}{2} + ik_0 \delta n(z, \tau) U - i\gamma P_0 |U|^2 U = 0, \quad (2.14)$$

where $\delta n(z, \tau)$ is the spatial and temporal variation of the refractive index along the fiber. It can be caused by temperature and density fluctuations in the fiber [40].

The thermodynamic estimate for Δn is given by [40]

$$\langle \Delta n^2 \rangle = \frac{-kT\rho^2}{V^2} \left(\frac{\partial V}{\partial P} \right)_T \left(\frac{\partial n}{\partial \rho} \right)_T^2 + \frac{kT^2}{\rho V C_v} \left(\frac{\partial n}{\partial T} \right)_\rho^2. \quad (2.15)$$

This gives the mean-square index fluctuation in terms of the properties of the material. It can be rewritten as

$$\langle \Delta n^2 \rangle = \frac{V_\rho + V_T}{V} = \langle \Delta n^2 \rangle_\rho + \langle \Delta n^2 \rangle_T. \quad (2.16)$$

For a fiber of length $z=1$ m and radius $r=2.82 \mu\text{m}$ (Volume $V=2.5 \times 10^{-12} \text{m}^3$), these have been calculated to be

$$\begin{aligned} \langle \Delta n^2 \rangle_\rho &\sim 10^{-21} \quad \equiv \quad \langle \Delta \rho^2 \rangle \sim 10^{-14} \frac{kg^2}{m^6}, \\ \langle \Delta n^2 \rangle_T &\sim 10^{-23} \quad \equiv \quad \langle \Delta T^2 \rangle \sim 10^{-12} \text{ }^\circ\text{C}^2. \end{aligned} \quad (2.17)$$

It should be noted that $\langle \Delta n^2 \rangle \propto (1/z) \Rightarrow \delta n \propto (1/\sqrt{z})$. The corresponding phase fluctuation that this would lead to in the NLSE is given by $\delta\phi = k_0 \delta n z \propto \sqrt{z}$, which is equivalent to the prescription for incorporating phase fluctuations into the stochastic NLSE model described in Sec. 2.3, namely, $\langle \Delta \phi^2 \rangle = 6.7 \times 10^{-3} z$. Hart *et al.* [28] used the same prescription and the same noise strength in their truncated-ODE model. From this we can estimate the level of refractive index fluctuation that

corresponds to the noise strength used in the simulations described in Sec. 2.3

$$\begin{aligned} \langle \Delta n^2 \rangle &= \frac{6.7 \times 10^{-3}}{k_0^2} = 6.78 \times 10^{-17} \\ &\equiv \langle \Delta T^2 \rangle \sim 10^{-6} \text{ }^\circ\text{C}^2 \equiv \Delta T \sim 10^{-3} \text{ }^\circ\text{C} \end{aligned} \quad (2.18)$$

The temperature coefficient of the refractive index of silica [40], $(\partial n / \partial T)_\rho \sim 10^{-5} \text{ }^\circ\text{C}^{-1}$. Thus even small spatio-temporal temperature fluctuations of $\sim 10^{-3} \text{ }^\circ\text{C}$ are enough to cause the inferred level of refractive index fluctuations.

The refractive index fluctuations could also be due to inhomogeneities in the density of the fiber material, frozen in at the time of manufacture of the fiber. The simulations were averaged over ~ 600 iterations to get a good estimate of the power fluctuations in the sidebands. Initially, simulations were performed with a different phase noise distribution for each iteration. Later, a particular (arbitrary) phase noise distribution was selected and frozen for all the iterations. This did not reduce the level of damping observed in the sideband trajectories provided that the strength of the phase noise was kept the same, thus indicating that density fluctuations induced during fiber manufacture could be a possible source. The phase noise was modeled as δ -correlated in both space and time. A more realistic approach would be to use correlated noise. Numerical methods to incorporate linear multiplicative correlated noise into the NLSE have been developed by M.J. Werner *et al.* [32].

2.5 Conclusions

The role of stochasticity in the dynamical evolution of four-wave-mixing processes in an optical fiber has been investigated. This research consisted of theoretical

and numerical computations. It focuses on tracing the evolution of the sidebands, generated through FWM, along a length of optical fiber. Detailed comparisons were made with the experimental results of Hart *et al.* [28] and the agreement was excellent. The present work uses numerical techniques that have much higher resolution and better efficiency, and it presents a theoretical basis for the role of the stochasticity in the dynamics. The system is known to be governed by the nonlinear Schrödinger equation (NLSE) to a very good approximation [8].

A powerful technique that can be used for simulations of the stochastic NLSE is the Split-step Fourier Method (SSFM) [8]. An algorithm for the direct implementation of stochastic processes along the length of the fiber in the SSFM has been developed. The advantages of this approach with respect to the coupled-ODE approach are that we can carry out simulations with much higher frequency and time resolution without sacrificing computational efficiency.

The physical sources of these stochastic phase fluctuations are investigated quantitatively and are identified to be due to fluctuations in the linear refractive index of the fiber. Strong candidates for the causes of these refractive index fluctuations are temperature fluctuations in the fiber medium caused by the fluctuating temperature of the fiber environment, density fluctuations in the fiber medium frozen into the fiber during manufacture, and intrinsic thermodynamic fluctuations in the temperature and density of the fiber.

The experiments performed by Hart *et al.* [28] can be used to determine the level of these refractive index fluctuations in commercial fibers. Results described in Figs. 2 and 3 represent a destructive experiment that measures the sideband

evolution with fiber length for a fixed input pump power, necessarily requiring the fiber to be cut repeatedly. The level of refractive index fluctuations can be used as a parameter in the simulations to best fit the experimental results. Alternatively, Fig. 4 represents a non-destructive experiment that measures the sideband evolution with input pump power for a fixed fiber length. These experiments are found to be effective for estimating the refractive index fluctuations, as the dynamics is observed to be sensitively dependent on the strength of the phase fluctuations.

Chapter 3

Stochastic Four-Wave-Mixing

3.1 Overview

The understanding of nonlinear processes in optical fibers is crucial towards extending the capabilities of modern optical communication systems based on wavelength division multiplexing (WDM), where each communication channel is represented by a unique wavelength. One of the nonlinear processes that limits the information carrying capacity of a WDM system is four-wave mixing (FWM), which causes cross-talk between neighboring channels. This places a lower limit on the wavelength separation between adjacent channels and an upper limit on the input power in each channel. In this study, we describe a process by which the evolution of FWM processes in an optical fiber can be used to estimate the inhomogeneities in the fiber core material, in particular the fluctuations in the linear refractive index of the fiber core.

Experiments measuring the evolution of FWM processes along a length of fiber were carried out by Hart *et al.* [28] and are described in detail in Sec. 2.2. In this experiment, two input pump waves at frequencies ω_1 and ω_2 , interacted with each other through the third-order nonlinearity of the fiber material to generate first-order sidebands at frequencies $\omega_3 = 2\omega_1 - \omega_2$ and $\omega_4 = 2\omega_2 - \omega_1$. These waves further interacted to produce second-order sidebands at $\omega_5 = 2\omega_3 - \omega_4$ and $\omega_6 = 2\omega_4 - \omega_3$.

Higher-order sidebands were also generated. The normalized power in the sideband at frequency ω_m was represented by ρ_m . The evolution of the FWM processes was characterized by the evolution of $\rho_m(z)$ as a function of fiber length z .

In the present work, we make a quantitative comparison between these experimental results and our numerical results based on efficient algorithms [8] to solve the nonlinear Schrödinger equation (NLSE) that governs the system. The numerical model, its underlying assumptions and the results are described in Sec. 3.3. A realistic description of a standard single mode optical fiber must take into account the random phase perturbations a light wave undergoes while propagating through it, without disturbing the underlying conservative properties of the system. The NLSE needs to be suitably modified in order to incorporate the stochastic nature of the propagation. In order to preserve the conservative properties of the system, the stochastic terms in the NLSE must necessarily be multiplicative in nature as an additive term acts as a source or a sink. An algorithm that achieves this with linear, Gaussian, δ -correlated noise is outlined in Sec. 3.3. This algorithm preserves the unconditional stability of the system. At the same time, care is taken to transform the stochastic NLSE from its original Ito representation [29] to the computationally feasible Stratanovich representation [30] by compensating for the spurious linear drift that results from integrating such stochastic differential equations [31, 32, 33, 34]. The dominant sources of phase noise are discussed in Sec. 3.4.

Conclusions on the relevance of the experiments of Hart *et al.* [28] and the stochastic modeling presented here are summarized in Sec. 2.5.

3.2 Experimental and Computational Background

In this work, we focus on tracing the evolution of the sidebands, generated through FWM, along a length of optical fiber. The FWM spectral evolution along 50 m of fiber for two input pump power regimes (2.1 W and 5.5 W) was investigated [28]. In the 2.1 W case, the sideband evolution followed a damped sinusoid along the length of the fiber. The experiments also found that the two first-order sidebands (ρ_3 -blueshifted and ρ_4 -redshifted from the two pumps) had different evolutions along the fiber (with different spatial wavelengths). For the 5.5 W case, the evolution of both first- and second-order sidebands was measured. The damping in the first-order sidebands (ρ_3 and ρ_4) occurred faster than in the 2.1 W case. Experiments probing the dependence of the sideband power on the input power (ranging from 2 W to 17 W) were also performed at a fixed output length of 50 m of the fiber. At the same fiber length, the optical spectra for input powers ranging from 2 W to 17 W were also recorded [28]. The spectral envelopes were observed to fit well to a hyperbolic secant function and the fit parameters were recorded. Measurements with a high-resolution wavemeter showed that one of the two pumps consisted of two very closely spaced longitudinal modes ($\Delta\nu \sim 0.5$ GHz) which were not resolved by the spectrometer used to record the FWM spectra. Inclusion of this multimode nature of the pump input in their model was found to alter the sideband dynamics dramatically and partly explained the asymmetry between the blue-shifted and red-shifted sidebands though it did not account for the damping in the sidebands. This was accounted for by adding weak phase fluctuations to the waves as they propagated

along the fiber [28]. The physical source of these phase fluctuations was not known at that time. However, the inclusion of the phase fluctuations into the model gave excellent qualitative and quantitative agreement with experiment. Their model involved integration of a system of coupled ODEs derived from the NLSE [35] by a process of truncation that retained only the leading frequency components (the pumps and the first- and second-order sidebands), a process justified by the fact that the input pump waves are well approximated by a combination of monochromatic waves. Their final numerical results are based on simulations using the truncated-ODE model with Langevin noise terms representing phase fluctuations in the fiber. Another physical source of stochasticity in their experiment was the inherent power fluctuation in the lasers used as the input pumps. The level of fluctuations (5-20%) was measured and incorporated appropriately into their model through stochastic initial conditions. This explained the evolution of the level of observed fluctuations in the sideband trajectories although it was found to be inadequate by itself, to account for the damping of the trajectories. They found that all three physical characteristics mentioned above, namely the multimode nature of the pump input, the stochastic phase fluctuations along the length of the fiber, and the stochastic initial power fluctuations were crucial to explaining the different features of the experimental measurements [28].

3.3 Stochastic NLSE Model

In the present work, we have developed and implemented an unconditionally stable scheme for integrating the NLSE that successfully incorporates phase noise into the SSFM. Thus, we are now in a position to harness the high frequency / time resolution of the SSFM together with its efficient convergence properties. Due to these advances, we are now able to do simulations with much higher frequency resolution (60 MHz as compared to 300 GHz in the ODE model). This high resolution, coupled with an appropriate convolution scheme, enables us to compare these simulated spectra with the composite spectra observed by the spectrometers which had a resolution of ~ 60 GHz. This was not possible with the truncated ODE model as the resolution of the simulated spectra in that case was ~ 300 GHz. For exactly the same levels of phase fluctuations, and initial condition fluctuations as used in Ref. [28], comparisons for the present NLSE model with the experimental sideband evolution functions $\rho_i(z)$ show excellent quantitative agreement. These results, along with the algorithms employed, are described in detail in this section. We have identified linear refractive index fluctuations along the fiber length to be a strong candidate for a physical source of the stochastic phase fluctuations. A comparison between the various possible sources is given in Sec. 3.4.

Under the assumption that the electric field of the light in the fiber has a slowly varying envelope $A(z, \tau)$, and that the fiber medium has an instantaneous nonlinear response, the system is well described by the nonlinear Schrödinger equation (NLSE)

with a linear multiplicative stochastic term

$$\frac{\partial U}{\partial z} + \frac{i\beta^{(2)}}{2T_0^2} \frac{\partial^2 U}{\partial \tau^2} + \frac{\alpha U}{2} + i\Gamma(z, \tau)U - i\gamma P_0 |U|^2 U = 0. \quad (3.1)$$

Z is distance along the length of the fiber, $U(z, \tau) = A(z, \tau)/\sqrt{P_0}$ is the complex electric field envelope $A(z, \tau)$ normalized to the absolute amplitude of the field $\sqrt{P_0}$, P_0 is the total power in the fiber, τ is time normalized to a convenient time scale T_0 (~ 1 ns) measured in a reference frame moving with the group velocity of the pulse [$\tau = (t - z/v_g)/T_0$]. The simulations are carried out for exactly the same physical parameters as the experiments and simulations reported by Hart *et al.* [28], i.e., $\beta^{(2)} = 55$ (ps)²/km, is the group velocity dispersion of the fiber at the operating wavelength $\lambda_0 \sim 632$ nm ($k_0 \sim 10^7$ m⁻¹). A loss of ~ 6 dB/km gives $\alpha = 0.0014$ m⁻¹ as the loss in the fiber at this wavelength. The nonlinearity coefficient $\gamma = 0.019$ W⁻¹m⁻¹ is given by

$$\gamma = \frac{\omega_{ave} n_2^I}{c A_{eff}}, \quad (3.2)$$

where A_{eff} is the effective core area of the fiber, n_2^I is the Kerr coefficient for the intensity-dependent refractive index, and ω_{ave} is the average angular frequency of the wave envelope. $\Gamma(z, \tau)$ is a linear multiplicative phase noise field. In this study the noise field is assumed to be δ -correlated in both space and time. The evolution of the FWM dynamics is found to be sensitive to the strength of this noise field. It can be physically interpreted as phase noise arising due to fluctuations in the linear refractive index of the fiber medium. A detailed discussion of its physical origin is given in Sec. 3.4.

The system was simulated using the Split-Step Fourier Method (SSFM) [8].

An algorithm for appropriately incorporating stochastic phase fluctuations along the length of the fiber in the SSFM was developed and is summarized below.

The NLSE is composed of linear and nonlinear terms, and can be written in operator form as

$$\begin{aligned}
\frac{\partial U}{\partial z} &= (\hat{D} + \hat{S} + \hat{N})U \\
\hat{D} &= \frac{-i\beta^{(2)}}{2T_0^2} \frac{\partial^2}{\partial \tau^2} - \frac{\alpha}{2} \\
\hat{S} &= i\Gamma(z, \tau) \\
\hat{N} &= i\gamma P_0 |U|^2,
\end{aligned} \tag{3.3}$$

where \hat{D} , \hat{S} and \hat{N} are linear (dispersive), nonlinear and stochastic operators, respectively. It has an exact solution for infinitesimal Δz given by -

$$U(z + \Delta z, \tau) = \exp[\Delta z(\hat{D} + \hat{S} + \hat{N})]U(z, \tau), \tag{3.4}$$

which can be approximated by

$$U(z + \Delta z, \tau) \approx \exp[\Delta z \hat{D}] \exp[\Delta z \hat{S}] \exp[\Delta z \hat{N}] U(z, \tau). \tag{3.5}$$

The execution of $\exp[\Delta z \hat{N}]$ is carried out in τ -space:

$$B_1(z, \tau) = \exp[\Delta z \hat{N}] U(z, \tau). \tag{3.6}$$

The execution of $\exp[\Delta z \hat{S}]$ and $\exp[\Delta z \hat{D}]$ is carried out in ω -space.

In particular, the stochastic phase fluctuations are introduced by modifying the phase ϕ_j of each frequency component ω_j of the complex field according to

$$\begin{aligned}
B_2(z, \omega) &= \mathcal{F}[B_1(z, \tau)] \\
B_3(z, \omega_j) &= \exp[i\delta\phi(z, \omega_j)] B_2(z, \omega_j),
\end{aligned} \tag{3.7}$$

where \mathcal{F} represents the Fourier transform operation.

This process only modifies the phase of each complex frequency component, leaving its absolute value unchanged. Thus the algorithm conserves the total power and the unconditional stability of the system.

The stochastic phase fluctuations $\delta\phi(z, \omega_j)$ are taken to be δ -correlated in frequency as well as spatially along the fiber length. The Box-Muller algorithm [36] was used to generate Gaussian random deviates from computer-generated uniform random deviates r_{1j} and r_{2j} at each spatial step and for each frequency component ω_j . The fluctuations are given by

$$\delta\phi(z, \omega_j) = \sqrt{-2\sigma_\phi^2 \Delta z \ln(r_{1j})} \cos(2\pi r_{2j}). \quad (3.8)$$

This is followed by the execution of $\exp[\Delta z \hat{D}]$, which is also carried out in Fourier space, followed by the inverse transform

$$U(z + \Delta z, \tau) = \mathcal{F}^{-1}[\exp[\Delta z \hat{D}(i\omega)] B_3(z, \omega)]. \quad (3.9)$$

$\hat{D}(i\omega)$ is obtained by replacing $(\partial/\partial\tau)$ by $i\omega$.

The basic form of the initial complex wave envelope function is

$$U(0, \tau) = \exp\left(-\frac{\tau^2}{2\tau_p^2}\right) \left\{ \begin{array}{l} \exp\left(\frac{i\Omega\tau}{2}\right) + \\ \exp\left(-\frac{i\Omega\tau}{2}\right) \end{array} \right\}, \quad (3.10)$$

where τ_p is the pulse width $T_p = 5$ ns FWHM, normalized to the time scale T_0 , $\Omega = 366$ GHz is the frequency detuning between the two laser sources normalized to a frequency scale $\Omega_0 = 62.5$ MHz. Figure 3.1(a) shows a plot of this pulse $|U(0, \tau)|^2$. The overall Gaussian envelope has an FWHM of 5 ns, the closely spaced dark lines

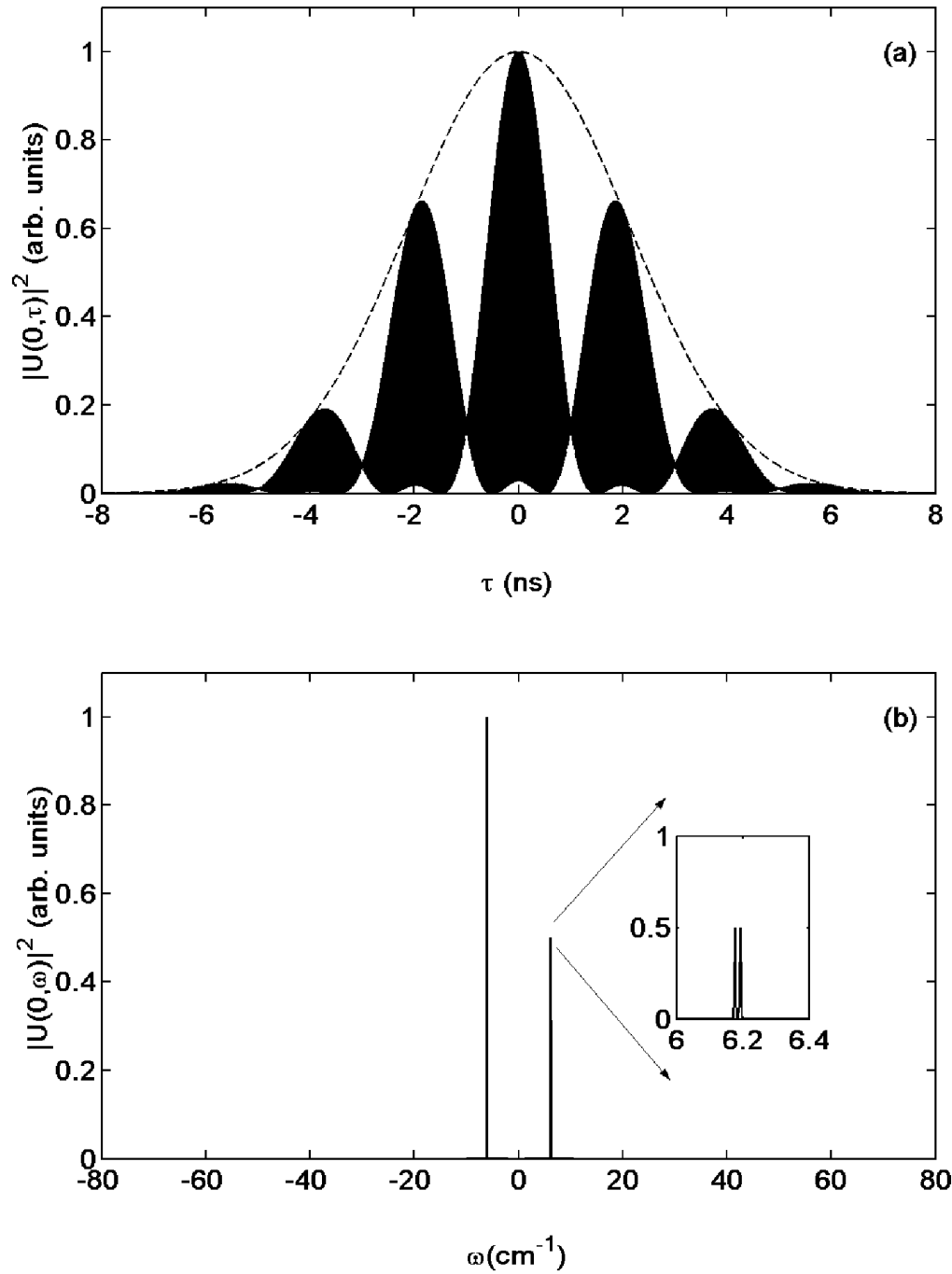


Figure 3.1: Multimode pulse input to the NLSE: (a) input pulse in time domain and (b) input spectrum.

are due to the 366 GHz (~ 3 ps) beating between the two input pump frequencies. The 2 ns modulations on the pulse are due to the 0.5 GHz mode-structure in the blue-shifted pump wave. Figure 3.1(b) shows the input spectrum of this pulse which consists of two highly monochromatic pump waves with a detuning of $\Omega=366$ GHz. The spectrum of the blue-shifted pump, upon magnification, is seen to be composed of two very closely spaced peaks, with a separation of $\Delta\nu=0.5$ GHz. Hart *et al.* [28] did not use pulsed wave functions in their NLSE simulations as the size of the FFT required to do so made it computationally prohibitive at that time. The size of the FFT was chosen such that it would accommodate a time span of 16 ns in order to go sufficiently far into the wings on the Gaussian pulse; and a frequency span of 16 THz in order to accommodate all the sidebands generated and prevent spurious effects due to the reflection boundary conditions implicit in the SSFM algorithm. These considerations dictated the size of the FFT to be $\geq(16 \text{ THz})\cdot(16 \text{ ns}) = 256000$. The nearest power of 2 is $2^{18} = 262144$, which has been used throughout the present work. The incorporation of the pulsed nature of the light was found to be necessary in explaining the dynamics. From the perspective of the coupled amplitude equations used by Hart *et al.* [28], the present model is equivalent to a coupled-ODE model with 2^{18} coupled ODEs.

Upon incorporation of the multimode nature of the blue input pump laser source and the stochastic fluctuations in the initial power in the lasers, the initial

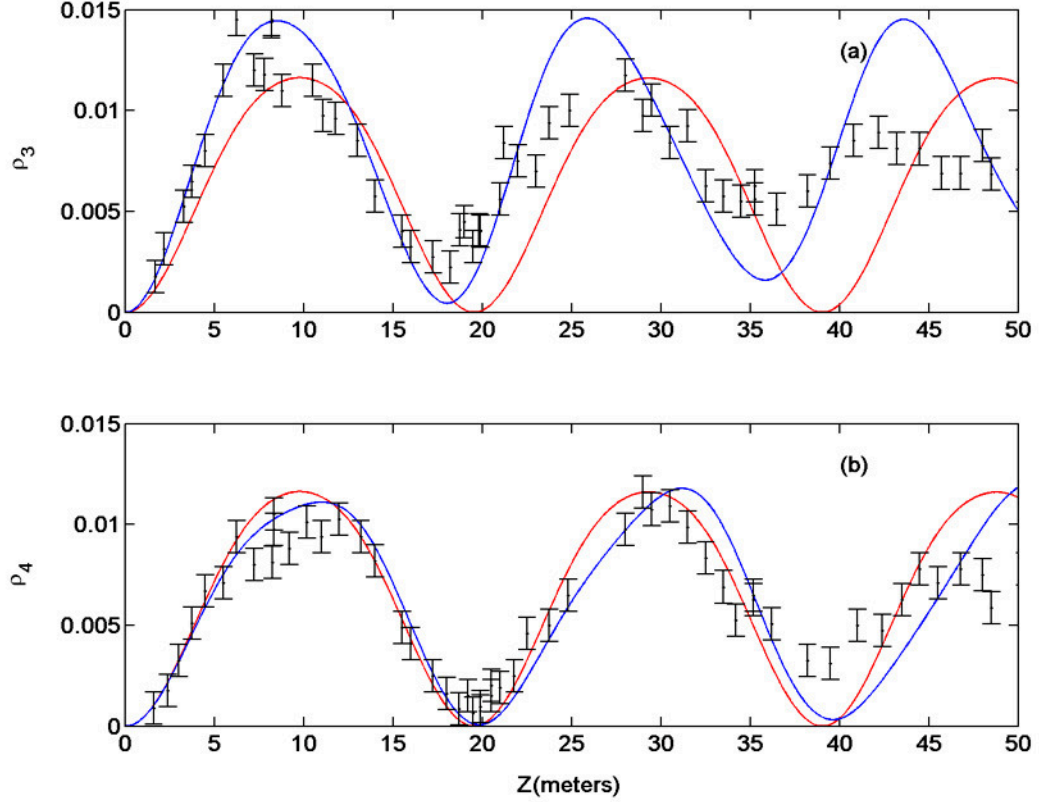


Figure 3.2: Effects of inclusion of the multimode nature ($\Delta\nu = 0.5$ GHz) of the blue-shifted input pump laser on the 1st order sideband evolution as a function of fiber length for $P_0 = 2.1$ W. Dashed curves represent simulations without the multimode nature and solid curves represent simulations with the multimode nature. $\Omega = 366$ GHz, $\gamma = 0.019$ W⁻¹ m⁻¹, and $\beta^{(2)} = 55$ ps²/km (a) power in the blue-shifted sideband, (b) power in the red-shifted sideband.

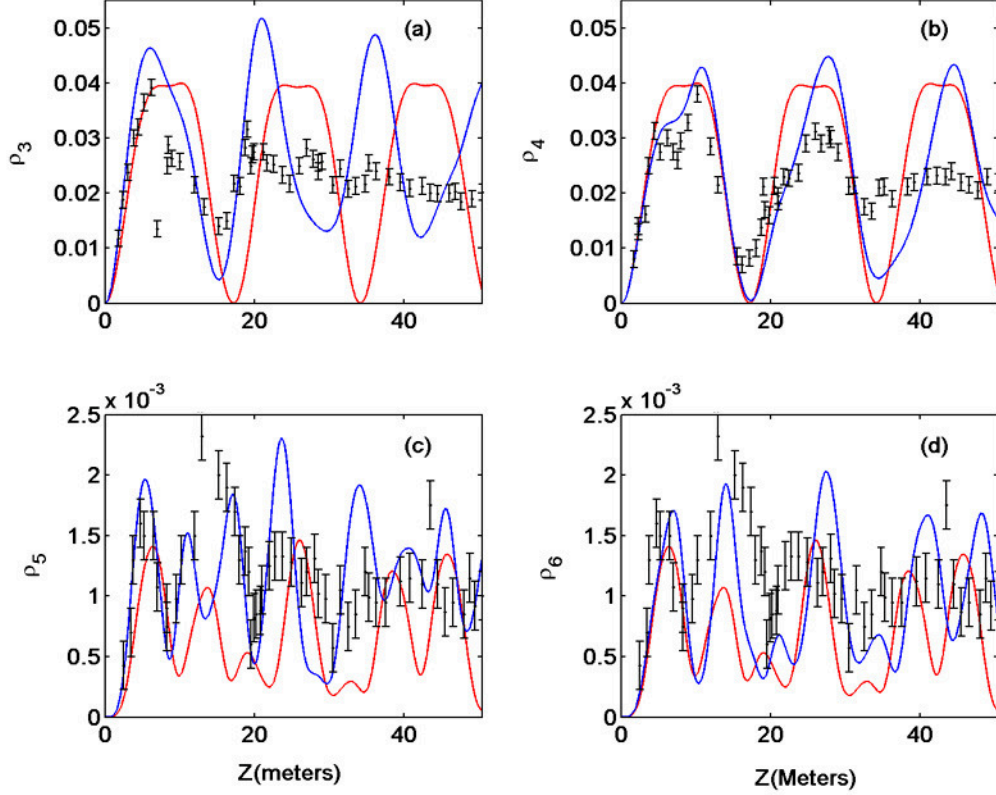


Figure 3.3: Effects of inclusion of the multimode nature ($\Delta\nu = 0.5$ GHz) of the blue-shifted input pump laser on the 1st order sideband evolution as a function of fiber length for $P_0 = 5.5$ W. Dashed curves represent simulations without the multimode nature and solid curves represent simulations with the multimode nature. $\Omega = 366$ GHz, $\gamma = 0.019$ W $^{-1}$ m $^{-1}$, and $\beta^{(2)} = 55$ ps 2 /km (a) power in the first-order blue-shifted sideband, (b) power in the first-order red-shifted sideband, (c) power in the second-order blue-shifted sideband, (d) power in the second-order red-shifted sideband.

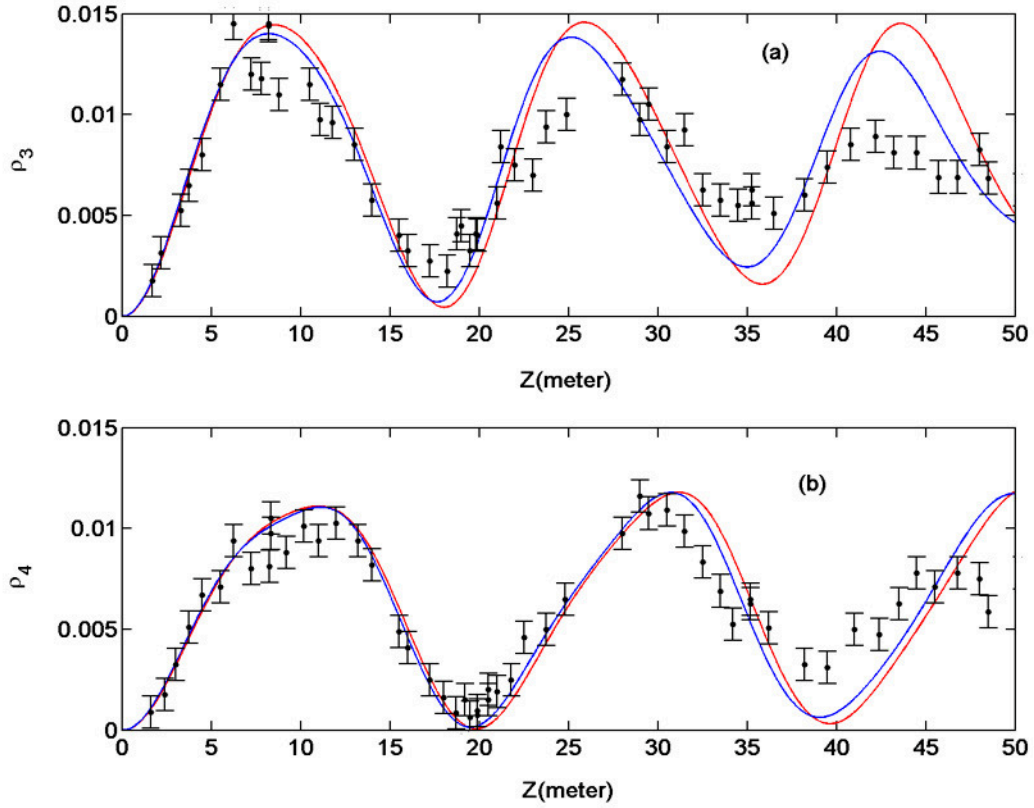


Figure 3.4: Effects of inclusion of the pulsed nature (5 ns FWHM) of the input pump laser light on the first-order sideband evolution as a function of fiber length for $P_0 = 2.1$ W. Dashed curves represent cw simulations and solid curves represent pulsed simulations. $\Omega = 366$ GHz, $\Delta\nu = 0.5$, $\gamma = 0.019$ W⁻¹m⁻¹, and $\beta^{(2)} = 55$ ps²/km (a) power in the blue-shifted sideband, (b) power in the red-shifted sideband.

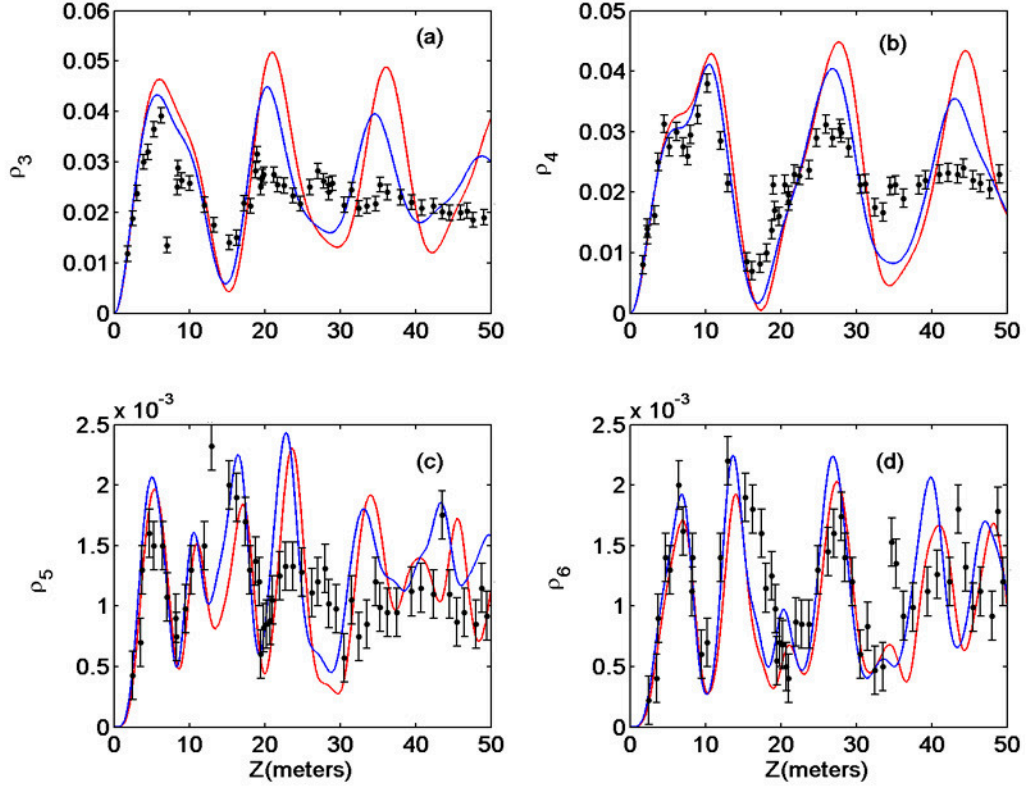


Figure 3.5: Effects of inclusion of the pulsed nature (5 ns FWHM) of the input pump laser on the first- and second-order sideband evolution as a function of fiber length for $P_0 = 5.5$ W. Dashed curves represent cw simulations and solid curves represent pulsed simulations. $\Omega = 366$ GHz, $\Delta\nu = 0.5$, $\gamma = 0.019$ W $^{-1}$ m $^{-1}$, and $\beta^{(2)} = 55$ ps 2 /km (a) power in the first-order blue-shifted sideband, (b) power in the first-order red-shifted sideband, (c) power in the second-order blue-shifted sideband, (d) power in the second-order red-shifted sideband.

wave function takes the form

$$U(0, \tau) = \exp\left(-\frac{\tau^2}{2\tau_p^2}\right) \left\{ \begin{array}{l} \sqrt{\frac{1+\delta\rho_1}{2}} \left[\begin{array}{l} \exp\left(\frac{i(\Omega+\Delta\nu)\tau}{2}\right) + \\ \exp\left(\frac{i(\Omega-\Delta\nu)\tau}{2}\right) \end{array} \right] \\ + \sqrt{1+\delta\rho_2} \exp\left(-\frac{i\Omega\tau}{2}\right) \end{array} \right\}. \quad (3.11)$$

$\Delta\nu = 0.5$ GHz is the frequency separation between the two longitudinal modes in the blue-shifted pump. $\delta\rho_1$ and $\delta\rho_2$ are Gaussian random deviates (generated using the Box-Muller algorithm [36]) that represent the initial power fluctuations in each of the pump laser sources. Their standard deviations were taken to be, $\sigma_{\rho_1} = 0.2$, $\sigma_{\rho_2} = 0.11$ for simulations from 0 m to 20 m, $\sigma_{\rho_1} = 0.12$, $\sigma_{\rho_2} = 0.05$ for simulations from 20 m to 50 m along the length of the fiber. This is exactly the same prescription used by Hart *et al.* [28] in their simulations and is dictated by their experimental measurements of the fluctuations in the pump laser intensities.

At this point it is worth noting the effects of the inclusion of two attributes of the input laser light, namely, the multimode nature of the blue-shifted pump, and the pulsed nature of the input light (assumed to be cw in the simulations reported by Hart *et al.* [28]).

Figure 3.2 shows a comparison between simulations with (solid curves) and without (dashed curves) the multimode nature for an input pump power of 2.1 Watts. The simulations with the mode structure show the asymmetry between the blue- and red-shifted sideband evolution, in particular, the difference in spatial wavelength between the two, and a non-return to zero nature of the evolution, as observed in the experimental data (black dots with error bars). These features are

absent in the simulations without mode-structure. ρ_3 and ρ_4 stands for the first order blue- and red-shifted sidebands respectively. Figure 3.3 shows the corresponding comparison for the case of 5.5 Watts of input pump power. Here, too, the simulations incorporating the multimode nature of the blue-shifted pump (solid curves) are seen to be an improvement over those not incorporating it (dashed curves). A feature of the experimental data (black dots with errorbars) is that for the ρ_3 sideband, the initial part of the evolution involves a peak followed by a shoulder, while for the ρ_4 sideband, the initial part of the evolution involves a shoulder followed by a peak. This feature, too, is seen to occur as a result of the inclusion of the multimode nature of the blue-shifted pump.

The effect of inclusion of the pulsed nature of the input beam is seen in Fig. 3.4 (for the 2.1 Watt case) and Fig. 3.5 (for the 5.5 Watt case). The solid dashes represent simulations for a cw input beam and the solid curves represent those for a pulsed input beam. The incorporation of the pulsed nature clearly results in damping of the sideband trajectories which are seen to come closer to the experimental data [28] (black dots with error bars).

Use of the FFT algorithm makes evaluation relatively fast compared to other finite-difference schemes. The computational error is $O(\Delta z^2)$, thus the solution converges with decreasing spatial step-size Δz .

The simulations were tested for the conservation of total power along the fiber length (by setting the loss α to zero) and for the conservation of asymmetry [35, 28]

given by

$$C(Z) = \sum_{i=1}^{\infty} (2i - 1) [\rho_{2i-1}(Z) - \rho_{2i}(Z)]. \quad (3.12)$$

A clearer picture of the evolution of the sidebands is obtained by plotting both the power in the sidebands and their standard deviations as a function of length along the fiber. Figures 3.6(a) and 3.6(b) show a comparison between simulation and experiment of the evolution of the first-order blue-shifted (ρ_3) and red-shifted (ρ_4) sidebands, respectively, for an input power of 2.1 W. The dashed curves represent NLSE simulations which include the stochastic nature of the input powers of the pump lasers but exclude the stochastic phase fluctuations added along the length of the fiber, an attribute which is included in the simulations represented by the solid curves. The black dots with error bars represent the experimental data. The measured sideband power, normalized to the total power in the fiber, is periodic in length but appears to be damping to a constant value. The measured data also show a clear difference between the spatial wavelengths of oscillation of the blue-shifted (ρ_3) and red-shifted (ρ_4) sidebands trajectories, respectively. Both these features are captured well by both the simulations. Figures 3.6(c) and 2.6(d) compare experimental and simulated measures of the evolution of the standard deviation in the sideband power along the fiber length. It is clearly observed that simulations with phase noise added to the light field along the length of the fiber (solid curves) are closer to the experimental data as compared to those that exclude this feature (dashed curves). This indicates the instrumental nature of the phase fluctuations in explaining key features of the dynamics.

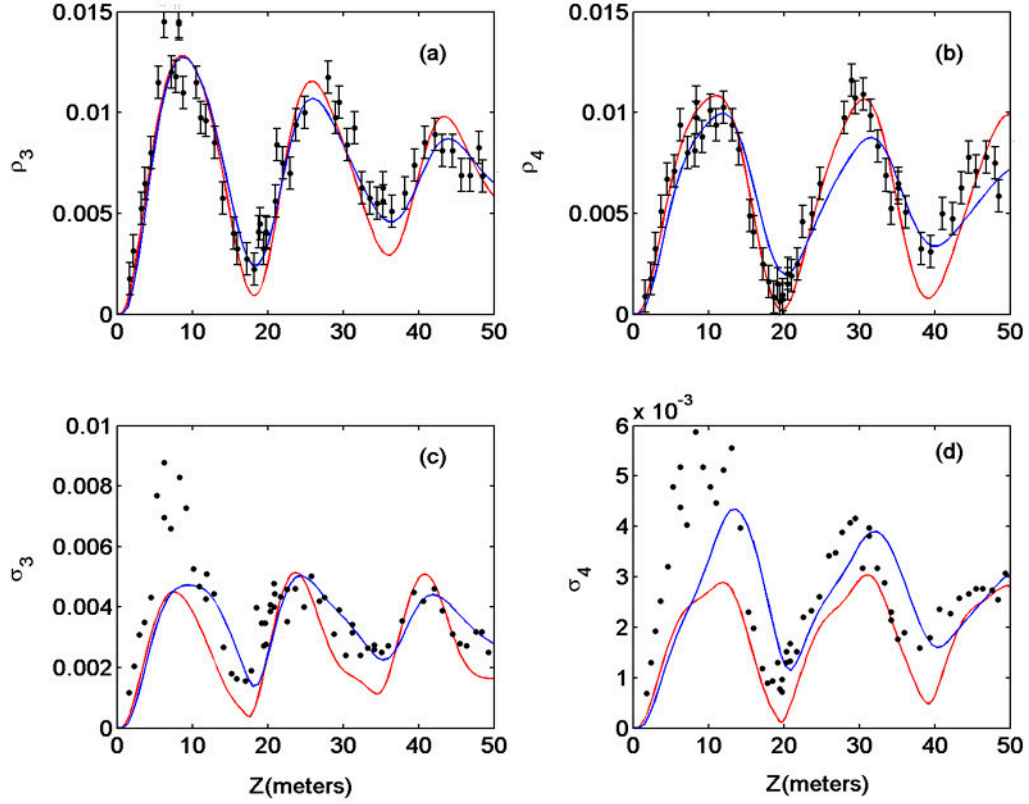


Figure 3.6: Comparison between the experimental measurements [28](black), the random initial condition NLSE model excluding phase noise (dashed curves) and the stochastic phase noise NLSE model (solid curves) showing the first-order sideband evolution as a function of fiber length for $P_0 = 2.1 \text{ W}$, $\Omega = 366 \text{ GHz}$, $\Delta\nu = 0.5 \text{ GHz}$, $\gamma = 0.019 \text{ W}^{-1}\text{m}^{-1}$, and $\beta^{(2)} = 55\text{ps}^2/\text{km}$: dynamical evolution of the: (a) power in the blue-shifted sideband, (b) power in the red-shifted sideband, (c) fluctuations in the blue-shifted sideband, (d) fluctuations in the red-shifted sideband.

The apparent damping of the periodic sideband trajectory is seen more dramatically in Figs. 3.7(a) and 3.7(b), which show the evolution of the first-order sideband power along the fiber for an input power of 5.5 W. The two first-order sidebands evolve differently. They appear to damp to a constant value at a faster rate than for the case with an input pump power of 2.1 W. Here again, NLSE simulations that incorporate phase noise along the length of the fiber (solid curves) are much more successful in accurately capturing the dynamical features of the system than NLSE simulations that do not take this feature into account (dashed curves). Figures 3.7(c) and 3.7(d) show a comparison between the simulated and measured standard deviations. Comparisons for the second-order blue-shifted (ρ_5) and red-shifted (ρ_6) sidebands, respectively, are shown in Figs. 3.7(e) and 3.7(f).

The observed dynamical evolution of the sidebands is found to depend sensitively on the strength of the stochastic phase fluctuations. Yet, best agreement with the experimental results of Hart *et al.* [28] is achieved with exactly the same noise strength σ_ϕ^2 as used in their truncated ODE model, namely, $\sigma_\phi^2 = 0.0067 \text{ m}^{-1}$. They report that including phase noise in their FWM calculations resulted in a spurious linear drift in the trajectories for the sideband power with length. To remove this artifact of the computations, they added a linear loss to their coupled ODEs. They set the loss coefficient $\alpha = 0.0046 \text{ m}^{-1}$ by finding the value that removed this increasing slope. We have observed exactly the same secular growth phenomenon for a wide range of the noise strength σ_ϕ^2 and have arrived at an empirical prescription for α namely, $\alpha \sim \sigma_\phi^2$, where σ_ϕ^2 is the variance of the added phase noise. This indicates the general nature of dynamics resulting from the addition of stochastic,

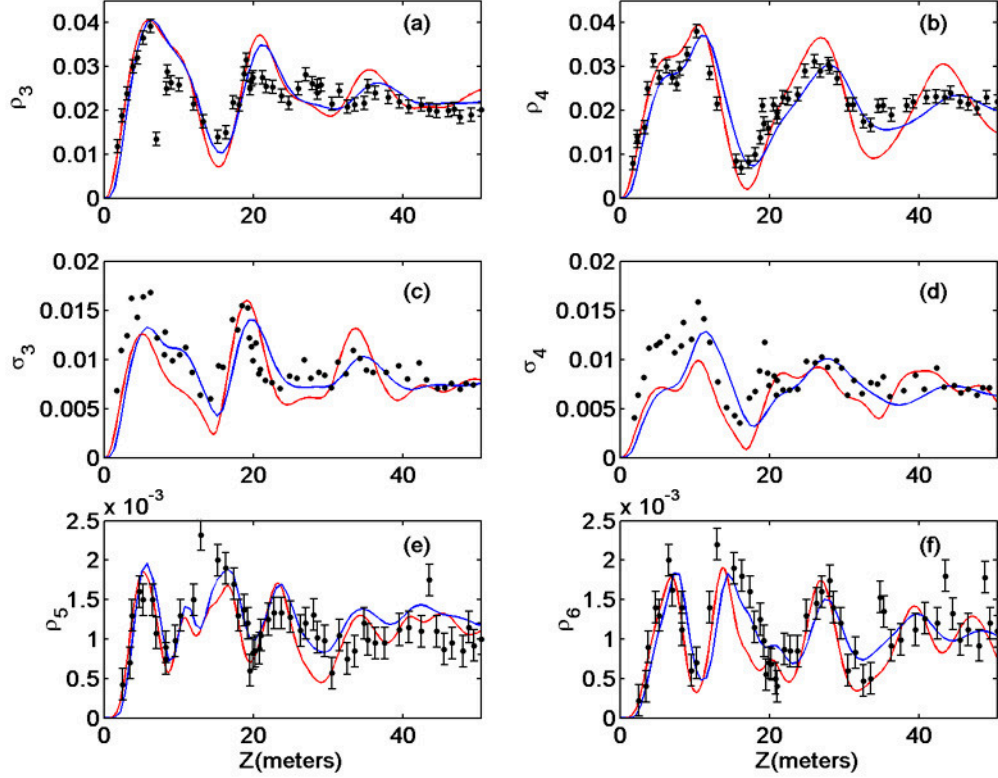


Figure 3.7: This figure caption is indented and single-spaced. Comparison between the experimental measurements [28] (black), the random initial condition NLSE model excluding phase noise (dashed curves) and the stochastic phase noise NLSE model (solid curves) showing the first- and second-order sideband evolution as a function of fiber length for $P_0 = 5.5 \text{ W}$, $\Omega = 366 \text{ GHz}$, $\Delta\nu = 0.5 \text{ GHz}$, $\gamma = 0.019 \text{ W}^{-1}\text{m}^{-1}$, and $\beta^{(2)} = 55 \text{ ps}^2/\text{km}$: dynamical evolution of the: (a) power in the first-order blue-shifted sideband, (b) power in the first-order red-shifted sideband, (c) fluctuations in the first-order blue-shifted sideband, (d) fluctuations in the first-order red-shifted sideband, (e) power in the second-order blue-shifted sideband, (f) power in the second-order red-shifted sideband.

δ -correlated phase fluctuations to systems governed by nonlinear partial differential equations [31].

It is remarkable that the strength of the phase noise required is the same in both the 2.1 W and the 5.5 W cases. Further, it is worth noting that exactly the same noise strength was used by Hart *et al.* [28], the difference being that they introduced phase noise only in the pump frequencies, whereas we have introduced it in all the Fourier modes ($\sim 2^{18}$). As a confirmation of this result, they also performed experiments and numerical simulations examining the sideband power dependence on the input power at a fixed length of 50.4 m of the same fiber. We have repeated these simulations with the stochastic NLSE model and the results are shown in Figs. 3.8(a) (blue-shifted sideband) and 3.8(b) (red-shifted sideband). The experimental measurements of the sideband powers are represented by filled squares and the results of numerical simulations are represented by triangles (without phase noise) and by circles (with phase noise). The simulations are seen to follow the general trend seen in the experiments. As the pump power is increased, the triangles (without phase noise) start to disagree with experiment, whereas the circles (with phase noise) are much closer to experiment. The phase noise strength used in these simulations was exactly the same as that used in the simulations depicted in Figs. 3.6 and 3.7. The agreement between the phase noise simulations and the experimental data was (once again) highly sensitive to the noise strength. Since this experiment (unlike those shown in Figs. 3.2 - 3.7) is non-destructive, it can be used to deduce the strength of phase noise processes in a given optical fiber. It will be shown in Sec. 3.4 that a likely cause of the phase noise is fluctuation in the linear refractive

index of the fiber. The noise strength deduced from the present computational study corresponds to a refractive index inhomogeneity of $\langle \Delta n^2 \rangle \sim 10^{-16}$.

Till now the comparisons between our simulations of the full NLSE and the truncated ODE model give basically the same results, although with much better agreement with experiment. However, the full NLSE can also provide a detailed comparison with the experimental spectra. This was not available from the truncated ODE model. The simulations reported in this work were carried out with a very high frequency and time resolution in order to incorporate the fact that the input light was not cw, but was composed of ~ 5 ns long pulses; and that the number of sidebands generated required the frequency spread of the FFT to be ~ 16 THz, while resolving a longitudinal mode-structure of $\Delta\nu \sim 0.5$ GHz. The spectral resolution used was ~ 0.05 GHz, whereas the spectrometer used to observe the spectra had a resolution 1000 times larger (~ 50 GHz). To account for this difference, the simulated spectra were first convolved with a Gaussian of unit peak and 62 GHz FWHM, before they were compared with the observed spectra.

Figures 3.9(a) and 3.9(b) show three-dimensional plots of the average experimental FWM output spectrum along the length of the fiber for input pump powers of 2.1 W and 5.5 W, respectively (courtesy Hart *et al.* [28]). The vertical axis represents the intensity, normalized to the peak power in one of the input pumps, plotted on a logarithmic scale. The pump frequencies are centered on $\pm \Omega/2$ and the fiber length is increasing into the page. Figures 9(c) and 9(d) show the corresponding comparisons based on simulations using the stochastic-NLSE model. The basic features of the spectral evolution are captured by the simulations.

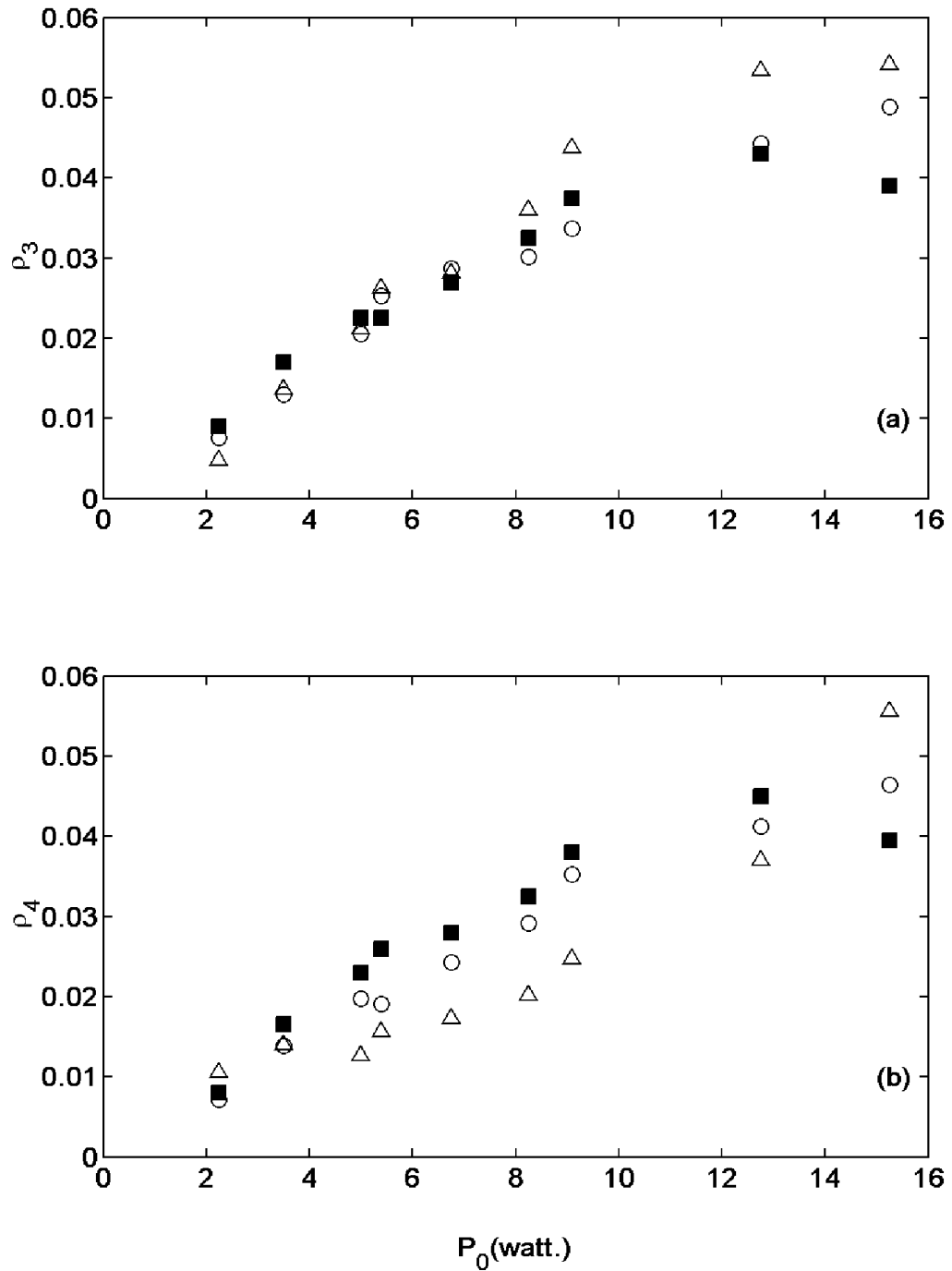


Figure 3.8: Comparison between the experimental measurements (filled squares), simulations without stochastic phase fluctuations (open triangles) and with stochastic phase fluctuations (open circles) of the first-order sideband power versus pump input power for $L=50.39$ m, and

Figure 3.9: Evolution of the FWM spectrum along the fiber (a) $P=2.1$ W, experiment, (b) $P=5.5$ W, experiment, (c) $P=2.1$ W, stochastic-NLSE model, (d) $P=5.5$ W, stochastic-NLSE model.

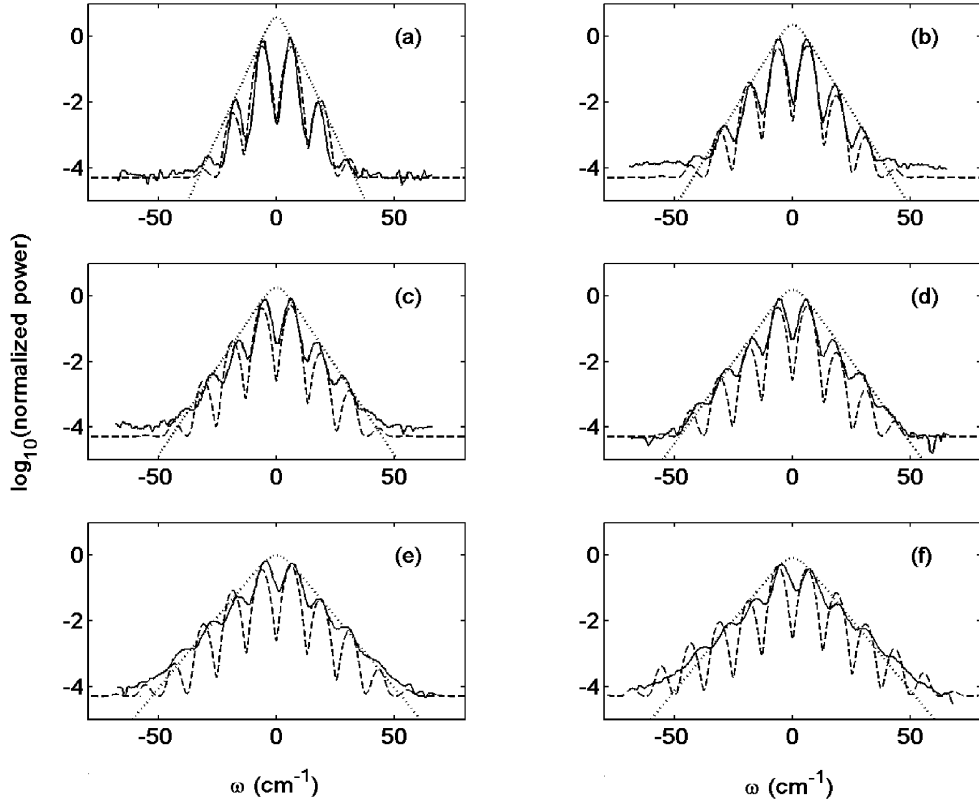


Figure 3.10: Experimental FWM output spectrum (solid line), convolved spectra from simulations of the stochastic NLSE model (dashed line), and hyperbolic secant envelope fit (dotted line) for pump input powers P_0 of (a) 2.1 W, (b) 5.5 W, (c) 6.7 W, (d) 8.3 W, (e) 12.7 W, (f) 17.4 W, fiber length $L= 50.39$ m, $\Omega = 366$ GHz, $\Delta\nu = 0.5$ GHz, $\gamma = 0.019$ W $^{-1}$ m $^{-1}$, and $\beta^{(2)} = 55$ ps 2 /km.

Hart *et al.* [28] also documented the experimentally observed FWM output spectra for a fixed fiber length of 50.39 meters for 6 different input pump powers. They state the coefficients A and B of the hyperbolic secant envelopes that best fit the output spectra which are given by

$$f(\omega) = A \operatorname{sech}(B\omega), \quad (3.13)$$

where A and B are the experimental fit parameters.

The hyperbolic secant parameters A and B, that best fit the simulated spectra are exactly the same as those that best fit the experimental spectra [28] for all the 6 cases of input power considered. Figure 2.10 shows an overlap of the simulated spectra (dashed line), with the experimental spectra (solid line) and the experimental hyperbolic secant envelope (dotted line) for 6 different pump powers, namely, (a) 2.1 W, (b) 5.5 W, (c) 6.7 W, (d) 8.3 W, (e) 12.7 W, (f) 17.4 W. The hyperbolic secant parameters for each of these pump powers are (a) A=3.85 and B=0.36, (b) A=2.26 and B=0.27, (c) A=1.81, B=0.25, (d) A=1.56 and B=0.23, (e) A=0.98, B=0.20, and (f) A=0.81 and B=0.20. The exact shapes of the simulated spectra match very well with the experimental spectra for low input pump powers (2.1 W and 5.5 W), but tend to lack the "filled-in" character of the experimental spectra at higher powers (6.7 W, 8.3 W, 12.7 W and 17.4 W).

3.4 Discussion

Hart *et al.* [28] postulated that strong candidates for the possible physical sources of the phase fluctuations are stimulated Brillouin scattering, stimulated

Raman scattering and fiber medium inhomogeneities. Brillouin scattering was eliminated as a source, since a backward propagating wave, which is a signature of Brillouin scattering in optical fibers, was not observed in the experiments. We have modeled stimulated Raman scattering [27, 37] for our system and have found no evidence to support the hypothesis that it could be a possible source of the stochastic phase fluctuations for fiber lengths up to 50 meters and pump power levels up to 5.5 Watts. A more detailed discussion of the Raman scattering simulations performed is given in Chap. 3. Apart from these, quantum phase fluctuations are another well known, though extremely weak, source of phase noise in optical fibers [8, 38].

Fiber medium inhomogeneities were identified as the major cause of the stochastic phase fluctuations. These inhomogeneities can manifest themselves through spatial and/or temporal fluctuations in the fiber parameters, namely, the linear refractive index n_0 , the group velocity v_g , the group velocity dispersion $\beta^{(2)}$ and the nonlinearity γ [39]. Of these, the fluctuation in the linear refractive index was found to be the only source of phase fluctuation that had a significant effect on the dynamics. A relationship between the level of refractive index fluctuations and the corresponding level of phase fluctuations has been arrived at. It is found that refractive index fluctuations as small as $\sigma_n^2 \sim 10^{-17} \text{ m}^{-1}$ can cause the desired phase fluctuations. Possible sources of these refractive index fluctuations are discussed below.

Consider the modified nonlinear Schrödinger equation (NLSE) which is stated below, with the linear multiplicative noise term represented in terms of spatial and

temporal fluctuations in the refractive index of the fiber.

$$\frac{\partial U}{\partial z} + \frac{i\beta^{(2)}}{2T_0^2} \frac{\partial^2 U}{\partial \tau^2} + \frac{\alpha U}{2} + ik_0 \delta n(z, \tau) U - i\gamma P_0 |U|^2 U = 0, \quad (3.14)$$

where $\delta n(z, \tau)$ is the spatial and temporal variation of the refractive index along the fiber. It can be caused by temperature and density fluctuations in the fiber [40].

The thermodynamic estimate for Δn is given by [40]

$$\langle \Delta n^2 \rangle = \frac{-kT\rho^2}{V^2} \left(\frac{\partial V}{\partial P} \right)_T \left(\frac{\partial n}{\partial \rho} \right)_T^2 + \frac{kT^2}{\rho V C_v} \left(\frac{\partial n}{\partial T} \right)_\rho^2. \quad (3.15)$$

This gives the mean-square index fluctuation in terms of the properties of the material. It can be rewritten as

$$\langle \Delta n^2 \rangle = \frac{V_\rho + V_T}{V} = \langle \Delta n^2 \rangle_\rho + \langle \Delta n^2 \rangle_T. \quad (3.16)$$

For a fiber of length $z=1$ m and radius $r=2.82 \mu\text{m}$ (Volume $V=2.5 \times 10^{-12} \text{m}^3$), these have been calculated to be

$$\begin{aligned} \langle \Delta n^2 \rangle_\rho &\sim 10^{-21} \quad \equiv \quad \langle \Delta \rho^2 \rangle \sim 10^{-14} \frac{kg^2}{m^6}, \\ \langle \Delta n^2 \rangle_T &\sim 10^{-23} \quad \equiv \quad \langle \Delta T^2 \rangle \sim 10^{-12} \text{ }^\circ\text{C}^2. \end{aligned} \quad (3.17)$$

It should be noted that $\langle \Delta n^2 \rangle \propto (1/z) \Rightarrow \delta n \propto (1/\sqrt{z})$. The corresponding phase fluctuation that this would lead to in the NLSE is given by $\delta\phi = k_0 \delta n z \propto \sqrt{z}$, which is equivalent to the prescription for incorporating phase fluctuations into the stochastic NLSE model described in Sec. 2.3, namely, $\langle \Delta \phi^2 \rangle = 6.7 \times 10^{-3} z$. Hart *et al.* [28] used the same prescription and the same noise strength in their truncated-ODE model. From this we can estimate the level of refractive index fluctuation that

corresponds to the noise strength used in the simulations described in Sec. 3.3

$$\begin{aligned} \langle \Delta n^2 \rangle &= \frac{6.7 \times 10^{-3}}{k_0^2} = 6.78 \times 10^{-17} \\ &\equiv \langle \Delta T^2 \rangle \sim 10^{-6} \text{ }^\circ\text{C}^2 \equiv \Delta T \sim 10^{-3} \text{ }^\circ\text{C} \end{aligned} \quad (3.18)$$

The temperature coefficient of the refractive index of silica [40], $(\partial n / \partial T)_\rho \sim 10^{-5} \text{ }^\circ\text{C}^{-1}$. Thus even small spatio-temporal temperature fluctuations of $\sim 10^{-3} \text{ }^\circ\text{C}$ are enough to cause the inferred level of refractive index fluctuations.

The refractive index fluctuations could also be due to inhomogeneities in the density of the fiber material, frozen in at the time of manufacture of the fiber. The simulations were averaged over ~ 600 iterations to get a good estimate of the power fluctuations in the sidebands. Initially, simulations were performed with a different phase noise distribution for each iteration. Later, a particular (arbitrary) phase noise distribution was selected and frozen for all the iterations. This did not reduce the level of damping observed in the sideband trajectories provided that the strength of the phase noise was kept the same, thus indicating that density fluctuations induced during fiber manufacture could be a possible source. The phase noise was modeled as δ -correlated in both space and time. A more realistic approach would be to use correlated noise. Numerical methods to incorporate linear multiplicative correlated noise into the NLSE have been developed by M.J. Werner *et al.* [32].

3.5 Conclusions

The role of stochasticity in the dynamical evolution of four-wave-mixing processes in an optical fiber has been investigated. This research consisted of theoretical

and numerical computations. It focuses on tracing the evolution of the sidebands, generated through FWM, along a length of optical fiber. Detailed comparisons were made with the experimental results of Hart *et al.* [28] and the agreement was excellent. The present work uses numerical techniques that have much higher resolution and better efficiency, and it presents a theoretical basis for the role of the stochasticity in the dynamics. The system is known to be governed by the nonlinear Schrödinger equation (NLSE) to a very good approximation [8].

A powerful technique that can be used for simulations of the stochastic NLSE is the Split-step Fourier Method (SSFM) [8]. An algorithm for the direct implementation of stochastic processes along the length of the fiber in the SSFM has been developed. The advantages of this approach with respect to the coupled-ODE approach are that we can carry out simulations with much higher frequency and time resolution without sacrificing computational efficiency.

The physical sources of these stochastic phase fluctuations are investigated quantitatively and are identified to be due to fluctuations in the linear refractive index of the fiber. Strong candidates for the causes of these refractive index fluctuations are temperature fluctuations in the fiber medium caused by the fluctuating temperature of the fiber environment, density fluctuations in the fiber medium frozen into the fiber during manufacture, and intrinsic thermodynamic fluctuations in the temperature and density of the fiber.

The experiments performed by Hart *et al.* [28] can be used to determine the level of these refractive index fluctuations in commercial fibers. Results described in Figs. 2 and 3 represent a destructive experiment that measures the sideband

evolution with fiber length for a fixed input pump power, necessarily requiring the fiber to be cut repeatedly. The level of refractive index fluctuations can be used as a parameter in the simulations to best fit the experimental results. Alternatively, Fig. 4 represents a non-destructive experiment that measures the sideband evolution with input pump power for a fixed fiber length. These experiments are found to be effective for estimating the refractive index fluctuations, as the dynamics is observed to be sensitively dependent on the strength of the phase fluctuations.

Appendix A

Overview

The understanding of nonlinear processes in optical fibers is crucial towards extending the capabilities of modern optical communication systems based on wavelength division multiplexing (WDM), where each communication channel is represented by a unique wavelength. One of the nonlinear processes that limits the information carrying capacity of a WDM system is four-wave mixing (FWM), which causes cross-talk between neighboring channels. This places a lower limit on the wavelength separation between adjacent channels and an upper limit on the input power in each channel. In this study, we describe a process by which the evolution of FWM processes in an optical fiber can be used to estimate the inhomogeneities in the fiber core material, in particular the fluctuations in the linear refractive index of the fiber core.

Experiments measuring the evolution of FWM processes along a length of fiber were carried out by Hart *et al.* [28] and are described in detail in Sec. 2.2. In this experiment, two input pump waves at frequencies ω_1 and ω_2 , interacted with each other through the third-order nonlinearity of the fiber material to generate first-order sidebands at frequencies $\omega_3 = 2\omega_1 - \omega_2$ and $\omega_4 = 2\omega_2 - \omega_1$. These waves further interacted to produce second-order sidebands at $\omega_5 = 2\omega_3 - \omega_4$ and $\omega_6 = 2\omega_4 - \omega_3$. Higher-order sidebands were also generated. The normalized power in the sideband

at frequency ω_m was represented by ρ_m . The evolution of the FWM processes was characterized by the evolution of $\rho_m(z)$ as a function of fiber length z .

In the present work, we make a quantitative comparison between these experimental results and our numerical results based on efficient algorithms [8] to solve the nonlinear Schrödinger equation (NLSE) that governs the system. The numerical model, its underlying assumptions and the results are described in Sec. 2.3. A realistic description of a standard single mode optical fiber must take into account the random phase perturbations a light wave undergoes while propagating through it, without disturbing the underlying conservative properties of the system. The NLSE needs to be suitably modified in order to incorporate the stochastic nature of the propagation. In order to preserve the conservative properties of the system, the stochastic terms in the NLSE must necessarily be multiplicative in nature as an additive term acts as a source or a sink. An algorithm that achieves this with linear, Gaussian, δ -correlated noise is outlined in Sec. 2.3. This algorithm preserves the unconditional stability of the system. At the same time, care is taken to transform the stochastic NLSE from its original Ito representation [29] to the computationally feasible Stratanovich representation [30] by compensating for the spurious linear drift that results from integrating such stochastic differential equations [31, 32, 33, 34]. The dominant sources of phase noise are discussed in Sec. 2.4.

Conclusions on the relevance of the experiments of Hart *et al.* [28] and the stochastic modeling presented here are summarized in Sec. 2.5.

A.1 Experimental and Computational Background

In this work, we focus on tracing the evolution of the sidebands, generated through FWM, along a length of optical fiber. The FWM spectral evolution along 50 m of fiber for two input pump power regimes (2.1 W and 5.5 W) was investigated [28]. In the 2.1 W case, the sideband evolution followed a damped sinusoid along the length of the fiber. The experiments also found that the two first-order sidebands (ρ_3 -blueshifted and ρ_4 -redshifted from the two pumps) had different evolutions along the fiber (with different spatial wavelengths). For the 5.5 W case, the evolution of both first- and second-order sidebands was measured. The damping in the first-order sidebands (ρ_3 and ρ_4) occurred faster than in the 2.1 W case. Experiments probing the dependence of the sideband power on the input power (ranging from 2 W to 17 W) were also performed at a fixed output length of 50 m of the fiber. At the same fiber length, the optical spectra for input powers ranging from 2 W to 17 W were also recorded [28]. The spectral envelopes were observed to fit well to a hyperbolic secant function and the fit parameters were recorded. Measurements with a high-resolution wavemeter showed that one of the two pumps consisted of two very closely spaced longitudinal modes ($\Delta\nu \sim 0.5$ GHz) which were not resolved by the spectrometer used to record the FWM spectra. Inclusion of this multimode nature of the pump input in their model was found to alter the sideband dynamics dramatically and partly explained the asymmetry between the blue-shifted and red-shifted sidebands though it did not account for the damping in the sidebands. This was accounted for by adding weak phase fluctuations to the waves as they propagated

along the fiber [28]. The physical source of these phase fluctuations was not known at that time. However, the inclusion of the phase fluctuations into the model gave excellent qualitative and quantitative agreement with experiment. Their model involved integration of a system of coupled ODEs derived from the NLSE [35] by a process of truncation that retained only the leading frequency components (the pumps and the first- and second-order sidebands), a process justified by the fact that the input pump waves are well approximated by a combination of monochromatic waves. Their final numerical results are based on simulations using the truncated-ODE model with Langevin noise terms representing phase fluctuations in the fiber. Another physical source of stochasticity in their experiment was the inherent power fluctuation in the lasers used as the input pumps. The level of fluctuations (5-20%) was measured and incorporated appropriately into their model through stochastic initial conditions. This explained the evolution of the level of observed fluctuations in the sideband trajectories although it was found to be inadequate by itself, to account for the damping of the trajectories. They found that all three physical characteristics mentioned above, namely the multimode nature of the pump input, the stochastic phase fluctuations along the length of the fiber, and the stochastic initial power fluctuations were crucial to explaining the different features of the experimental measurements [28].

A.2 Stochastic NLSE Model

In the present work, we have developed and implemented an unconditionally stable scheme for integrating the NLSE that successfully incorporates phase noise into the SSFM. Thus, we are now in a position to harness the high frequency / time resolution of the SSFM together with its efficient convergence properties. Due to these advances, we are now able to do simulations with much higher frequency resolution (60 MHz as compared to 300 GHz in the ODE model). This high resolution, coupled with an appropriate convolution scheme, enables us to compare these simulated spectra with the composite spectra observed by the spectrometers which had a resolution of ~ 60 GHz. This was not possible with the truncated ODE model as the resolution of the simulated spectra in that case was ~ 300 GHz. For exactly the same levels of phase fluctuations, and initial condition fluctuations as used in Ref. [28], comparisons for the present NLSE model with the experimental sideband evolution functions $\rho_i(z)$ show excellent quantitative agreement. These results, along with the algorithms employed, are described in detail in this section. We have identified linear refractive index fluctuations along the fiber length to be a strong candidate for a physical source of the stochastic phase fluctuations. A comparison between the various possible sources is given in Sec. 2.4.

Under the assumption that the electric field of the light in the fiber has a slowly varying envelope $A(z, \tau)$, and that the fiber medium has an instantaneous nonlinear response, the system is well described by the nonlinear Schrödinger equation (NLSE)

with a linear multiplicative stochastic term

$$\frac{\partial U}{\partial z} + \frac{i\beta^{(2)}}{2T_0^2} \frac{\partial^2 U}{\partial \tau^2} + \frac{\alpha U}{2} + i\Gamma(z, \tau)U - i\gamma P_0 |U|^2 U = 0. \quad (\text{A.1})$$

Z is distance along the length of the fiber, $U(z, \tau) = A(z, \tau)/\sqrt{P_0}$ is the complex electric field envelope $A(z, \tau)$ normalized to the absolute amplitude of the field $\sqrt{P_0}$, P_0 is the total power in the fiber, τ is time normalized to a convenient time scale T_0 (~ 1 ns) measured in a reference frame moving with the group velocity of the pulse [$\tau = (t - z/v_g)/T_0$]. The simulations are carried out for exactly the same physical parameters as the experiments and simulations reported by Hart *et al.* [28], i.e., $\beta^{(2)} = 55$ (ps)²/km, is the group velocity dispersion of the fiber at the operating wavelength $\lambda_0 \sim 632$ nm ($k_0 \sim 10^7$ m⁻¹). A loss of ~ 6 dB/km gives $\alpha = 0.0014$ m⁻¹ as the loss in the fiber at this wavelength. The nonlinearity coefficient $\gamma = 0.019$ W⁻¹m⁻¹ is given by

$$\gamma = \frac{\omega_{ave} n_2^I}{c A_{eff}}, \quad (\text{A.2})$$

where A_{eff} is the effective core area of the fiber, n_2^I is the Kerr coefficient for the intensity-dependent refractive index, and ω_{ave} is the average angular frequency of the wave envelope. $\Gamma(z, \tau)$ is a linear multiplicative phase noise field. In this study the noise field is assumed to be δ -correlated in both space and time. The evolution of the FWM dynamics is found to be sensitive to the strength of this noise field. It can be physically interpreted as phase noise arising due to fluctuations in the linear refractive index of the fiber medium. A detailed discussion of its physical origin is given in Sec. 2.4.

The system was simulated using the Split-Step Fourier Method (SSFM) [8].

An algorithm for appropriately incorporating stochastic phase fluctuations along the length of the fiber in the SSFM was developed and is summarized below.

The NLSE is composed of linear and nonlinear terms, and can be written in operator form as

$$\begin{aligned}
\frac{\partial U}{\partial z} &= (\hat{D} + \hat{S} + \hat{N})U \\
\hat{D} &= \frac{-i\beta^{(2)}}{2T_0^2} \frac{\partial^2}{\partial \tau^2} - \frac{\alpha}{2} \\
\hat{S} &= i\Gamma(z, \tau) \\
\hat{N} &= i\gamma P_0 |U|^2,
\end{aligned} \tag{A.3}$$

where \hat{D} , \hat{S} and \hat{N} are linear (dispersive), nonlinear and stochastic operators, respectively. It has an exact solution for infinitesimal Δz given by -

$$U(z + \Delta z, \tau) = \exp[\Delta z(\hat{D} + \hat{S} + \hat{N})]U(z, \tau), \tag{A.4}$$

which can be approximated by

$$U(z + \Delta z, \tau) \approx \exp[\Delta z \hat{D}] \exp[\Delta z \hat{S}] \exp[\Delta z \hat{N}] U(z, \tau). \tag{A.5}$$

The execution of $\exp[\Delta z \hat{N}]$ is carried out in τ -space:

$$B_1(z, \tau) = \exp[\Delta z \hat{N}] U(z, \tau). \tag{A.6}$$

The execution of $\exp[\Delta z \hat{S}]$ and $\exp[\Delta z \hat{D}]$ is carried out in ω -space.

In particular, the stochastic phase fluctuations are introduced by modifying the phase ϕ_j of each frequency component ω_j of the complex field according to

$$\begin{aligned}
B_2(z, \omega) &= \mathcal{F}[B_1(z, \tau)] \\
B_3(z, \omega_j) &= \exp[i\delta\phi(z, \omega_j)] B_2(z, \omega_j),
\end{aligned} \tag{A.7}$$

where \mathcal{F} represents the Fourier transform operation.

This process only modifies the phase of each complex frequency component, leaving its absolute value unchanged. Thus the algorithm conserves the total power and the unconditional stability of the system.

The stochastic phase fluctuations $\delta\phi(z, \omega_j)$ are taken to be δ -correlated in frequency as well as spatially along the fiber length. The Box-Muller algorithm [36] was used to generate Gaussian random deviates from computer-generated uniform random deviates r_{1j} and r_{2j} at each spatial step and for each frequency component ω_j . The fluctuations are given by

$$\delta\phi(z, \omega_j) = \sqrt{-2\sigma_\phi^2 \Delta z \ln(r_{1j})} \cos(2\pi r_{2j}). \quad (\text{A.8})$$

This is followed by the execution of $\exp[\Delta z \hat{D}]$, which is also carried out in Fourier space, followed by the inverse transform

$$U(z + \Delta z, \tau) = \mathcal{F}^{-1}[\exp[\Delta z \hat{D}(i\omega)] B_3(z, \omega)]. \quad (\text{A.9})$$

$\hat{D}(i\omega)$ is obtained by replacing $(\partial/\partial\tau)$ by $i\omega$.

The basic form of the initial complex wave envelope function is

$$U(0, \tau) = \exp\left(-\frac{\tau^2}{2\tau_p^2}\right) \left\{ \begin{array}{l} \exp\left(\frac{i\Omega\tau}{2}\right) + \\ \exp\left(-\frac{i\Omega\tau}{2}\right) \end{array} \right\}, \quad (\text{A.10})$$

where τ_p is the pulse width $T_p = 5$ ns FWHM, normalized to the time scale T_0 , $\Omega = 366$ GHz is the frequency detuning between the two laser sources normalized to a frequency scale $\Omega_0 = 62.5$ MHz. Figure A.1(a) shows a plot of this pulse $|U(0, \tau)|^2$. The overall Gaussian envelope has an FWHM of 5 ns, the closely spaced dark lines

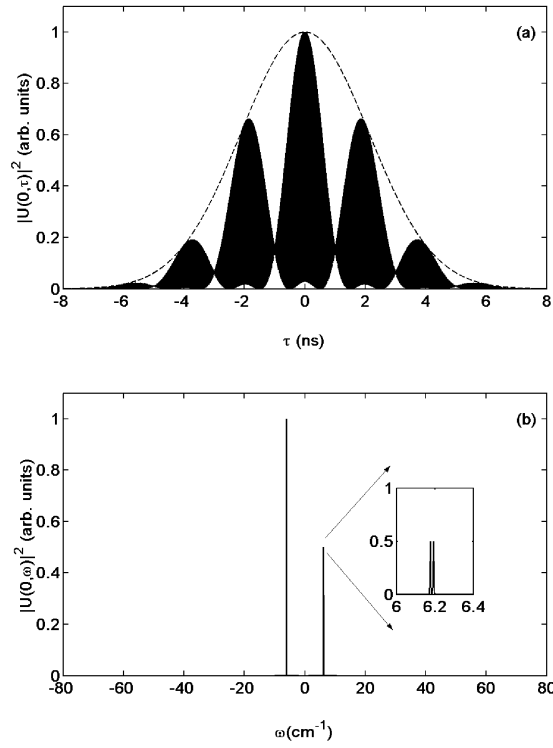


Figure A.1: Multimode pulse input to the NLSE: (a) input pulse in time domain and (b) input spectrum.

are due to the 366 GHz (~ 3 ps) beating between the two input pump frequencies. The 2 ns modulations on the pulse are due to the 0.5 GHz mode-structure in the blue-shifted pump wave. Figure A.1(b) shows the input spectrum of this pulse which consists of two highly monochromatic pump waves with a detuning of $\Omega=366$ GHz. The spectrum of the blue-shifted pump, upon magnification, is seen to be composed of two very closely spaced peaks, with a separation of $\Delta\nu=0.5$ GHz. Hart *et al.* [28] did not use pulsed wave functions in their NLSE simulations as the size of the FFT required to do so made it computationally prohibitive at that time. The size of the FFT was chosen such that it would accommodate a time span of 16 ns in order to go sufficiently far into the wings on the Gaussian pulse; and a frequency span of 16 THz in order to accommodate all the sidebands generated and prevent spurious effects due to the reflection boundary conditions implicit in the SSFM algorithm. These considerations dictated the size of the FFT to be $\geq(16 \text{ THz})\cdot(16 \text{ ns}) = 256000$. The nearest power of 2 is $2^{18} = 262144$, which has been used throughout the present work. The incorporation of the pulsed nature of the light was found to be necessary in explaining the dynamics. From the perspective of the coupled amplitude equations used by Hart *et al.* [28], the present model is equivalent to a coupled-ODE model with 2^{18} coupled ODEs.

Upon incorporation of the multimode nature of the blue input pump laser source and the stochastic fluctuations in the initial power in the lasers, the initial

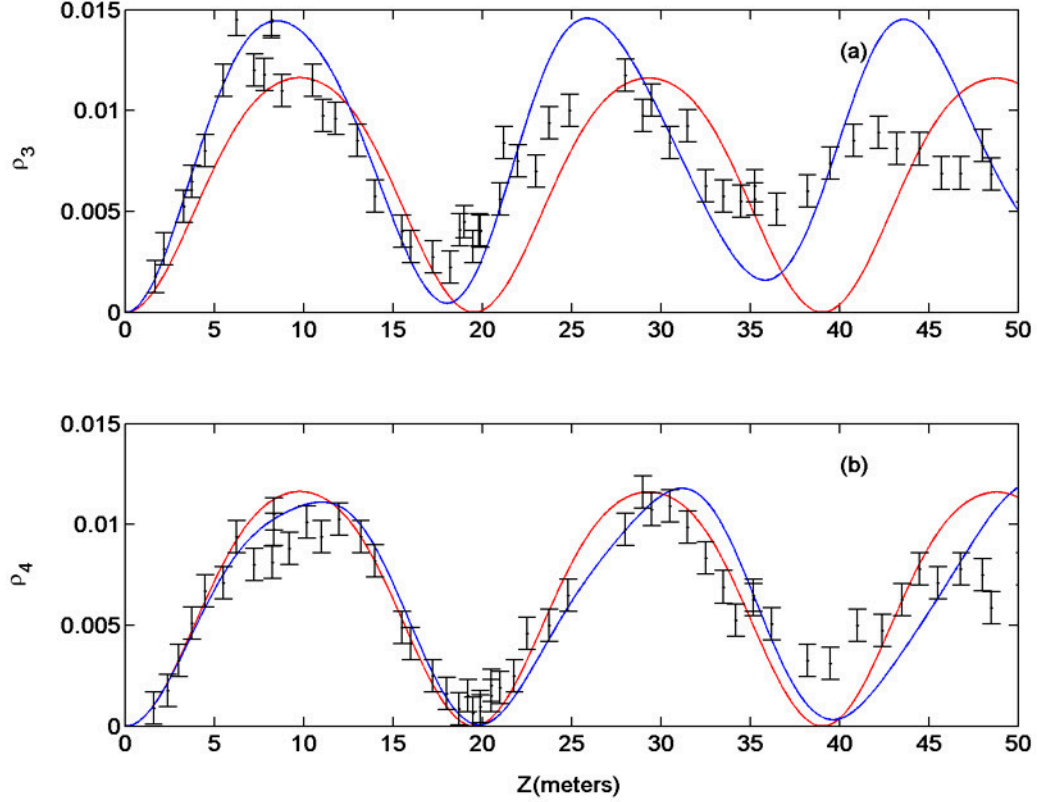


Figure A.2: Effects of inclusion of the multimode nature ($\Delta\nu = 0.5$ GHz) of the blue-shifted input pump laser on the 1st order sideband evolution as a function of fiber length for $P_0 = 2.1$ W. Dashed curves represent simulations without the multimode nature and solid curves represent simulations with the multimode nature. $\Omega = 366$ GHz, $\gamma = 0.019$ W $^{-1}$ m $^{-1}$, and $\beta^{(2)} = 55$ ps 2 /km (a) power in the blue-shifted sideband, (b) power in the red-shifted sideband.

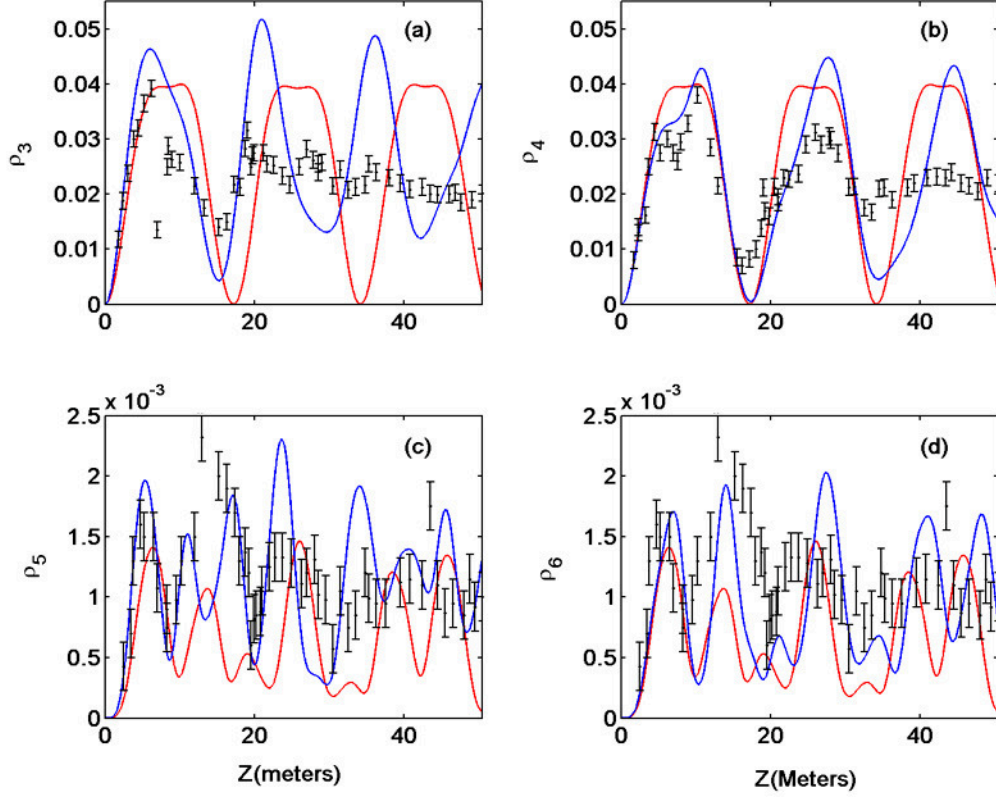


Figure A.3: Effects of inclusion of the multimode nature ($\Delta\nu = 0.5$ GHz) of the blue-shifted input pump laser on the 1st order sideband evolution as a function of fiber length for $P_0 = 5.5$ W. Dashed curves represent simulations without the multimode nature and solid curves represent simulations with the multimode nature. $\Omega = 366$ GHz, $\gamma = 0.019$ W $^{-1}$ m $^{-1}$, and $\beta^{(2)} = 55$ ps 2 /km (a) power in the first-order blue-shifted sideband, (b) power in the first-order red-shifted sideband, (c) power in the second-order blue-shifted sideband, (d) power in the second-order red-shifted sideband.

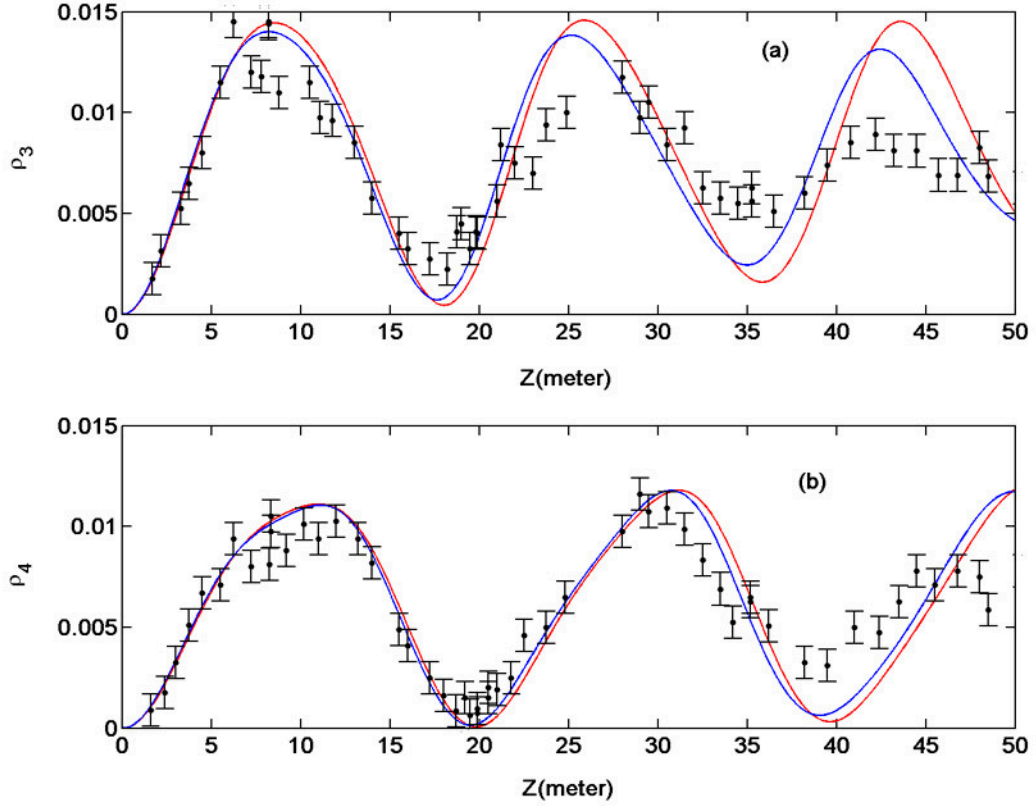


Figure A.4: Effects of inclusion of the pulsed nature (5 ns FWHM) of the input pump laser light on the first-order sideband evolution as a function of fiber length for $P_0 = 2.1$ W. Dashed curves represent cw simulations and solid curves represent pulsed simulations. $\Omega = 366$ GHz, $\Delta\nu = 0.5$, $\gamma = 0.019$ W $^{-1}$ m $^{-1}$, and $\beta^{(2)} = 55$ ps 2 /km (a) power in the blue-shifted sideband, (b) power in the red-shifted sideband.

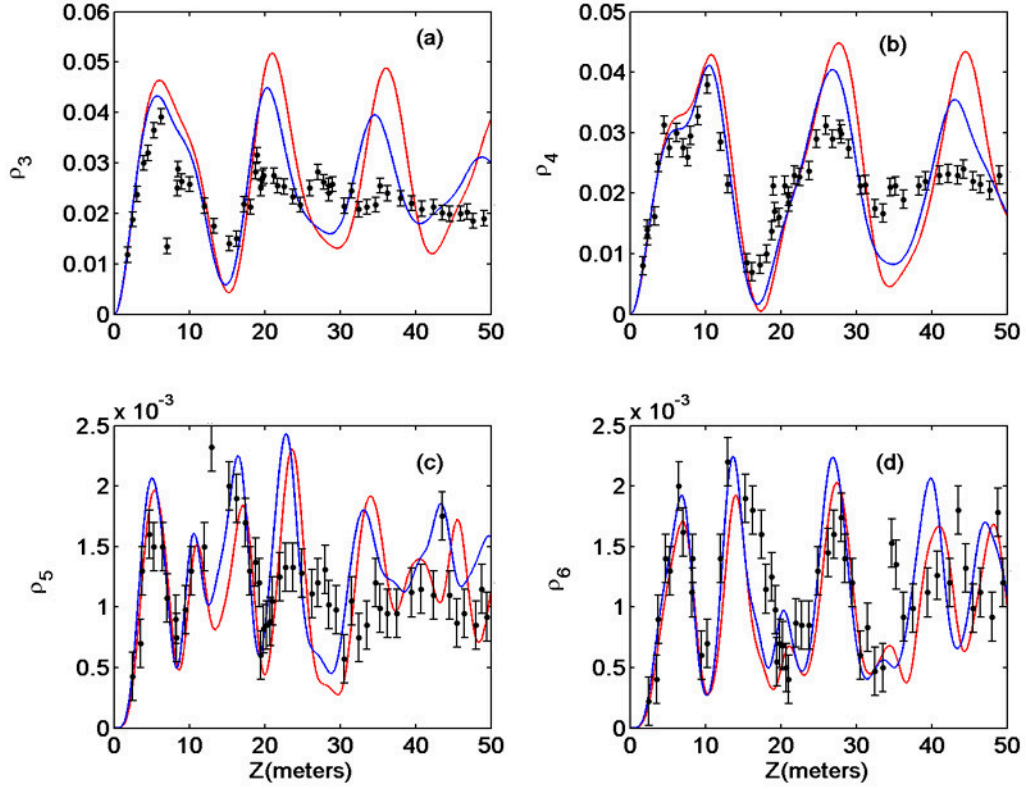


Figure A.5: Effects of inclusion of the pulsed nature (5 ns FWHM) of the input pump laser on the first- and second-order sideband evolution as a function of fiber length for $P_0 = 5.5$ W. Dashed curves represent cw simulations and solid curves represent pulsed simulations. $\Omega = 366$ GHz, $\Delta\nu = 0.5$, $\gamma = 0.019$ W $^{-1}$ m $^{-1}$, and $\beta^{(2)} = 55$ ps 2 /km (a) power in the first-order blue-shifted sideband, (b) power in the first-order red-shifted sideband, (c) power in the second-order blue-shifted sideband, (d) power in the second-order red-shifted sideband.

wave function takes the form

$$U(0, \tau) = \exp\left(-\frac{\tau^2}{2\tau_p^2}\right) \left\{ \begin{array}{l} \sqrt{\frac{1+\delta\rho_1}{2}} \left[\begin{array}{l} \exp\left(\frac{i(\Omega+\Delta\nu)\tau}{2}\right) + \\ \exp\left(\frac{i(\Omega-\Delta\nu)\tau}{2}\right) \end{array} \right] \\ + \sqrt{1+\delta\rho_2} \exp\left(-\frac{i\Omega\tau}{2}\right) \end{array} \right\}. \quad (\text{A.11})$$

$\Delta\nu = 0.5$ GHz is the frequency separation between the two longitudinal modes in the blue-shifted pump. $\delta\rho_1$ and $\delta\rho_2$ are Gaussian random deviates (generated using the Box-Muller algorithm [36]) that represent the initial power fluctuations in each of the pump laser sources. Their standard deviations were taken to be, $\sigma_{\rho_1} = 0.2$, $\sigma_{\rho_2} = 0.11$ for simulations from 0 m to 20 m, $\sigma_{\rho_1} = 0.12$, $\sigma_{\rho_2} = 0.05$ for simulations from 20 m to 50 m along the length of the fiber. This is exactly the same prescription used by Hart *et al.* [28] in their simulations and is dictated by their experimental measurements of the fluctuations in the pump laser intensities.

At this point it is worth noting the effects of the inclusion of two attributes of the input laser light, namely, the multimode nature of the blue-shifted pump, and the pulsed nature of the input light (assumed to be cw in the simulations reported by Hart *et al.* [28]).

Figure A.2 shows a comparison between simulations with (solid curves) and without (dashed curves) the multimode nature for an input pump power of 2.1 Watts. The simulations with the mode structure show the asymmetry between the blue- and red-shifted sideband evolution, in particular, the difference in spatial wavelength between the two, and a non-return to zero nature of the evolution, as observed in the experimental data (black dots with error bars). These features are

absent in the simulations without mode-structure. ρ_3 and ρ_4 stands for the first order blue- and red-shifted sidebands respectively. Figure 2.3 shows the corresponding comparison for the case of 5.5 Watts of input pump power. Here, too, the simulations incorporating the multimode nature of the blue-shifted pump (solid curves) are seen to be an improvement over those not incorporating it (dashed curves). A feature of the experimental data (black dots with errorbars) is that for the ρ_3 sideband, the initial part of the evolution involves a peak followed by a shoulder, while for the ρ_4 sideband, the initial part of the evolution involves a shoulder followed by a peak. This feature, too, is seen to occur as a result of the inclusion of the multimode nature of the blue-shifted pump.

The effect of inclusion of the pulsed nature of the input beam is seen in Fig. A.4 (for the 2.1 Watt case) and Fig. A.5 (for the 5.5 Watt case). The solid dashes represent simulations for a cw input beam and the solid curves represent those for a pulsed input beam. The incorporation of the pulsed nature clearly results in damping of the sideband trajectories which are seen to come closer to the experimental data [28] (black dots with error bars).

Use of the FFT algorithm makes evaluation relatively fast compared to other finite-difference schemes. The computational error is $O(\Delta z^2)$, thus the solution converges with decreasing spatial step-size Δz .

The simulations were tested for the conservation of total power along the fiber length (by setting the loss α to zero) and for the conservation of asymmetry [35, 28]

given by

$$C(Z) = \sum_{i=1}^{\infty} (2i - 1) [\rho_{2i-1}(Z) - \rho_{2i}(Z)]. \quad (\text{A.12})$$

A clearer picture of the evolution of the sidebands is obtained by plotting both the power in the sidebands and their standard deviations as a function of length along the fiber. Figures A.6(a) and A.6(b) show a comparison between simulation and experiment of the evolution of the first-order blue-shifted (ρ_3) and red-shifted (ρ_4) sidebands, respectively, for an input power of 2.1 W. The dashed curves represent NLSE simulations which include the stochastic nature of the input powers of the pump lasers but exclude the stochastic phase fluctuations added along the length of the fiber, an attribute which is included in the simulations represented by the solid curves. The black dots with error bars represent the experimental data. The measured sideband power, normalized to the total power in the fiber, is periodic in length but appears to be damping to a constant value. The measured data also show a clear difference between the spatial wavelengths of oscillation of the blue-shifted (ρ_3) and red-shifted (ρ_4) sidebands trajectories, respectively. Both these features are captured well by both the simulations. Figures A.6(c) and A.6(d) compare experimental and simulated measures of the evolution of the standard deviation in the sideband power along the fiber length. It is clearly observed that simulations with phase noise added to the light field along the length of the fiber (solid curves) are closer to the experimental data as compared to those that exclude this feature (dashed curves). This indicates the instrumental nature of the phase fluctuations in explaining key features of the dynamics.

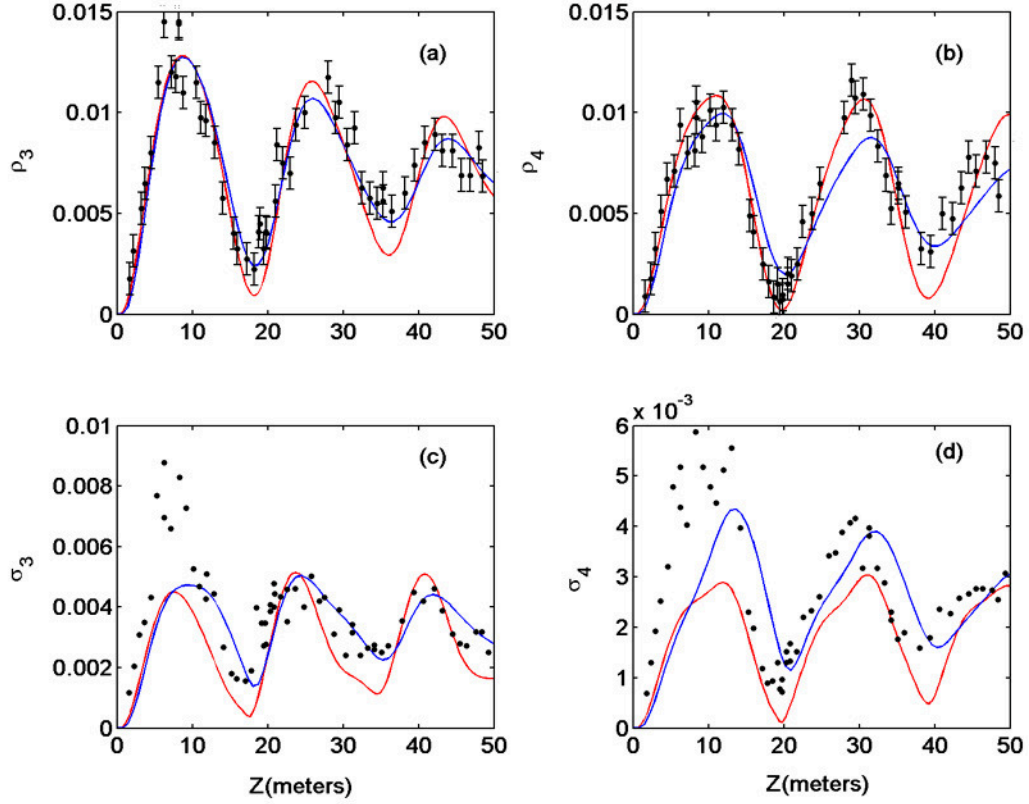


Figure A.6: Comparison between the experimental measurements [28](black), the random initial condition NLSE model excluding phase noise (dashed curves) and the stochastic phase noise NLSE model (solid curves) showing the first-order sideband evolution as a function of fiber length for $P_0 = 2.1$ W, $\Omega = 366$ GHz, $\Delta\nu = 0.5$ GHz, $\gamma = 0.019$ W⁻¹m⁻¹, and $\beta^{(2)} = 55$ ps²/km: dynamical evolution of the: (a) power in the blue-shifted sideband, (b) power in the red-shifted sideband, (c) fluctuations in the blue-shifted sideband, (d) fluctuations in the red-shifted sideband.

The apparent damping of the periodic sideband trajectory is seen more dramatically in Figs. A.7(a) and A.7(b), which show the evolution of the first-order sideband power along the fiber for an input power of 5.5 W. The two first-order sidebands evolve differently. They appear to damp to a constant value at a faster rate than for the case with an input pump power of 2.1 W. Here again, NLSE simulations that incorporate phase noise along the length of the fiber (solid curves) are much more successful in accurately capturing the dynamical features of the system than NLSE simulations that do not take this feature into account (dashed curves). Figures A.7(c) and A.7(d) show a comparison between the simulated and measured standard deviations. Comparisons for the second-order blue-shifted (ρ_5) and red-shifted (ρ_6) sidebands, respectively, are shown in Figs. A.7(e) and A.7(f).

The observed dynamical evolution of the sidebands is found to depend sensitively on the strength of the stochastic phase fluctuations. Yet, best agreement with the experimental results of Hart *et al.* [28] is achieved with exactly the same noise strength σ_ϕ^2 as used in their truncated ODE model, namely, $\sigma_\phi^2 = 0.0067 \text{ m}^{-1}$. They report that including phase noise in their FWM calculations resulted in a spurious linear drift in the trajectories for the sideband power with length. To remove this artifact of the computations, they added a linear loss to their coupled ODEs. They set the loss coefficient $\alpha = 0.0046 \text{ m}^{-1}$ by finding the value that removed this increasing slope. We have observed exactly the same secular growth phenomenon for a wide range of the noise strength σ_ϕ^2 and have arrived at an empirical prescription for α namely, $\alpha \sim \sigma_\phi^2$, where σ_ϕ^2 is the variance of the added phase noise. This indicates the general nature of dynamics resulting from the addition of stochastic,

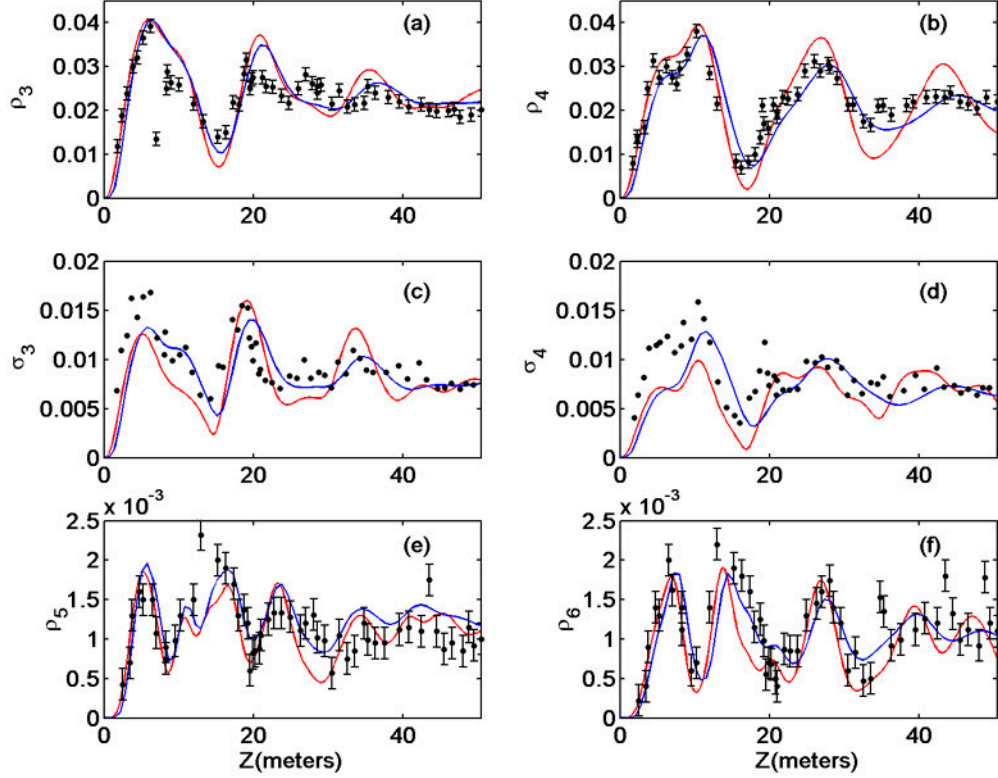


Figure A.7: This figure caption is indented and single-spaced. Comparison between the experimental measurements [28] (black), the random initial condition NLSE model excluding phase noise (dashed curves) and the stochastic phase noise NLSE model (solid curves) showing the first- and second-order sideband evolution as a function of fiber length for $P_0 = 5.5$ W, $\Omega = 366$ GHz, $\Delta\nu = 0.5$ GHz, $\gamma = 0.019$ W $^{-1}$ m $^{-1}$, and $\beta^{(2)} = 55$ ps 2 /km: dynamical evolution of the: (a) power in the first-order blue-shifted sideband, (b) power in the first-order red-shifted sideband, (c) fluctuations in the first-order blue-shifted sideband, (d) fluctuations in the first-order red-shifted sideband, (e) power in the second-order blue-shifted sideband, (f) power in the second-order red-shifted sideband.

δ -correlated phase fluctuations to systems governed by nonlinear partial differential equations [31].

It is remarkable that the strength of the phase noise required is the same in both the 2.1 W and the 5.5 W cases. Further, it is worth noting that exactly the same noise strength was used by Hart *et al.* [28], the difference being that they introduced phase noise only in the pump frequencies, whereas we have introduced it in all the Fourier modes ($\sim 2^{18}$). As a confirmation of this result, they also performed experiments and numerical simulations examining the sideband power dependence on the input power at a fixed length of 50.4 m of the same fiber. We have repeated these simulations with the stochastic NLSE model and the results are shown in Figs. 2.8(a) (blue-shifted sideband) and 2.8(b) (red-shifted sideband). The experimental measurements of the sideband powers are represented by filled squares and the results of numerical simulations are represented by triangles (without phase noise) and by circles (with phase noise). The simulations are seen to follow the general trend seen in the experiments. As the pump power is increased, the triangles (without phase noise) start to disagree with experiment, whereas the circles (with phase noise) are much closer to experiment. The phase noise strength used in these simulations was exactly the same as that used in the simulations depicted in Figs. A.6 and A.7. The agreement between the phase noise simulations and the experimental data was (once again) highly sensitive to the noise strength. Since this experiment (unlike those shown in Figs. A.2 - A.7) is non-destructive, it can be used to deduce the strength of phase noise processes in a given optical fiber. It will be shown in Sec. 2.4 that a likely cause of the phase noise is fluctuation in the linear refractive

index of the fiber. The noise strength deduced from the present computational study corresponds to a refractive index inhomogeneity of $\langle \Delta n^2 \rangle \sim 10^{-16}$.

Till now the comparisons between our simulations of the full NLSE and the truncated ODE model give basically the same results, although with much better agreement with experiment. However, the full NLSE can also provide a detailed comparison with the experimental spectra. This was not available from the truncated ODE model. The simulations reported in this work were carried out with a very high frequency and time resolution in order to incorporate the fact that the input light was not cw, but was composed of ~ 5 ns long pulses; and that the number of sidebands generated required the frequency spread of the FFT to be ~ 16 THz, while resolving a longitudinal mode-structure of $\Delta\nu \sim 0.5$ GHz. The spectral resolution used was ~ 0.05 GHz, whereas the spectrometer used to observe the spectra had a resolution 1000 times larger (~ 50 GHz). To account for this difference, the simulated spectra were first convolved with a Gaussian of unit peak and 62 GHz FWHM, before they were compared with the observed spectra.

Figures A.9(a) and A.9(b) show three-dimensional plots of the average experimental FWM output spectrum along the length of the fiber for input pump powers of 2.1 W and 5.5 W, respectively (courtesy Hart *et al.* [28]). The vertical axis represents the intensity, normalized to the peak power in one of the input pumps, plotted on a logarithmic scale. The pump frequencies are centered on $\pm \Omega/2$ and the fiber length is increasing into the page. Figures 9(c) and 9(d) show the corresponding comparisons based on simulations using the stochastic-NLSE model. The basic features of the spectral evolution are captured by the simulations.

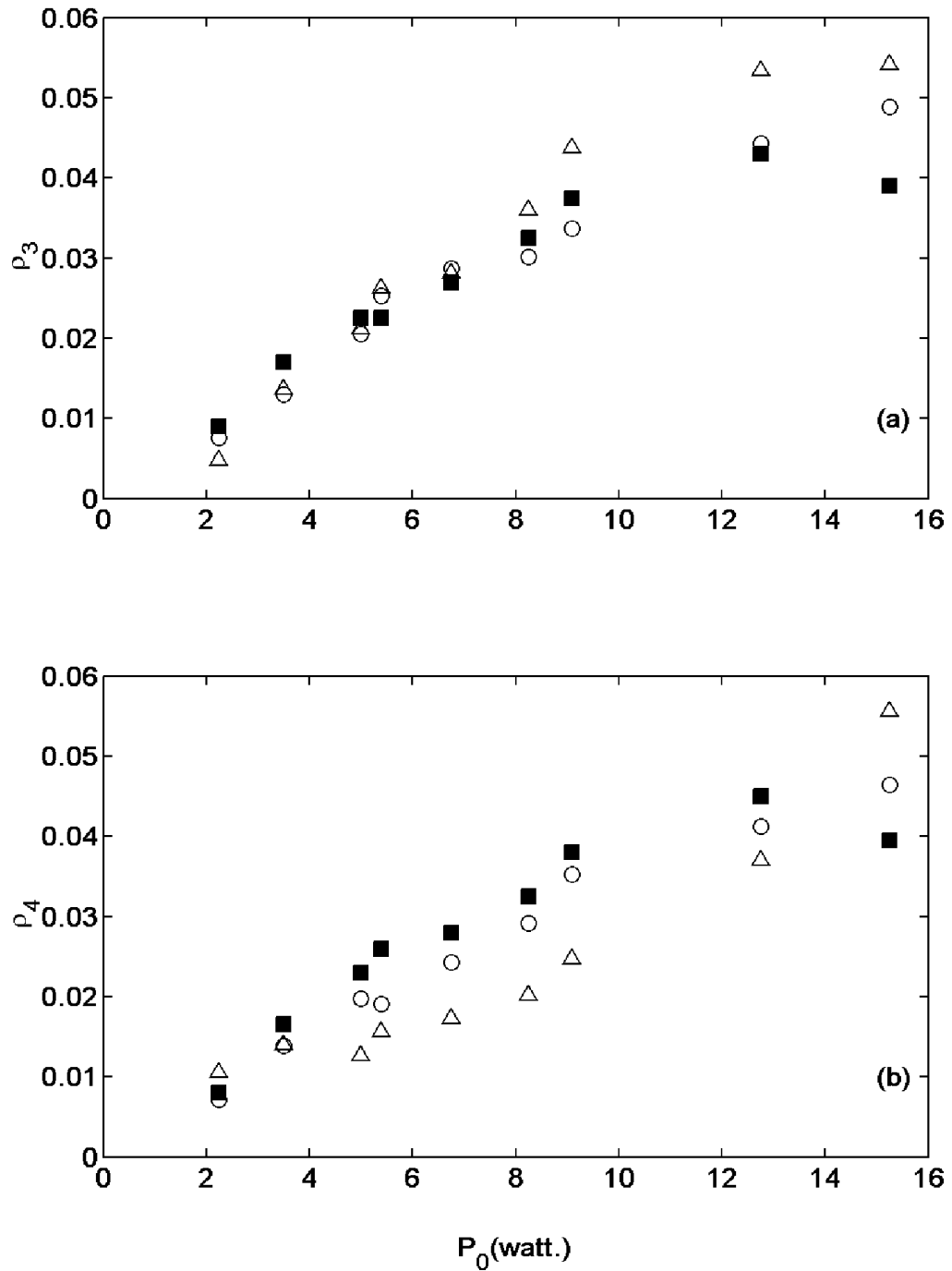


Figure A.8: Comparison between the experimental measurements (filled squares), simulations without stochastic phase fluctuations (open triangles) and with stochastic phase fluctuations (open circles) of the first-order sideband power versus pump input power for $L=50.39$ m, and $\Omega = 366$ GHz: power in the (a) blue-shifted sideband and (b) red-shifted sideband.

Figure A.9: Evolution of the FWM spectrum along the fiber (a) $P=2.1$ W, experiment, (b) $P=5.5$ W, experiment, (c) $P=2.1$ W, stochastic-NLSE model, (d) $P=5.5$ W, stochastic-NLSE model.

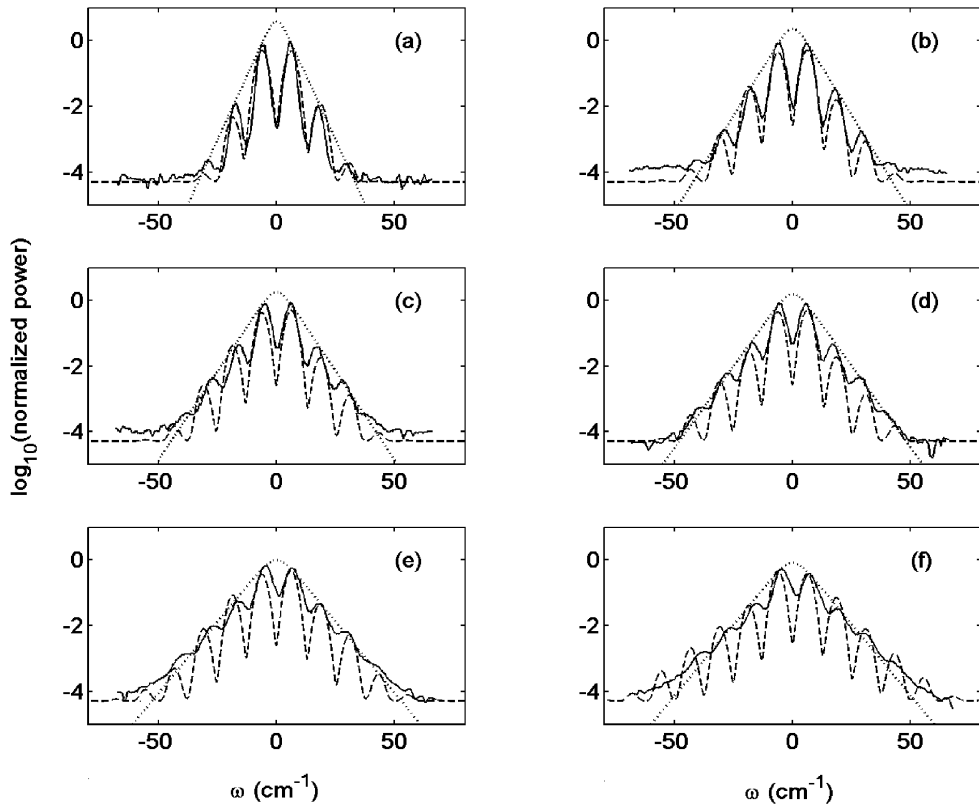


Figure A.10: Experimental FWM output spectrum (solid line), convolved spectra from simulations of the stochastic NLSE model (dashed line), and hyperbolic secant envelope fit (dotted line) for pump input powers P_0 of (a) 2.1 W, (b) 5.5 W, (c) 6.7 W, (d) 8.3 W, (e) 12.7 W, (f) 17.4 W, fiber length $L= 50.39$ m, $\Omega = 366$ GHz, $\Delta\nu = 0.5$ GHz, $\gamma = 0.019 \text{ W}^{-1}\text{m}^{-1}$, and $\beta^{(2)} = 55 \text{ ps}^2/\text{km}$.

Hart *et al.* [28] also documented the experimentally observed FWM output spectra for a fixed fiber length of 50.39 meters for 6 different input pump powers. They state the coefficients A and B of the hyperbolic secant envelopes that best fit the output spectra which are given by

$$f(\omega) = A \operatorname{sech}(B\omega), \quad (\text{A.13})$$

where A and B are the experimental fit parameters.

The hyperbolic secant parameters A and B, that best fit the simulated spectra are exactly the same as those that best fit the experimental spectra [28] for all the 6 cases of input power considered. Figure 2.10 shows an overlap of the simulated spectra (dashed line), with the experimental spectra (solid line) and the experimental hyperbolic secant envelope (dotted line) for 6 different pump powers, namely, (a) 2.1 W, (b) 5.5 W, (c) 6.7 W, (d) 8.3 W, (e) 12.7 W, (f) 17.4 W. The hyperbolic secant parameters for each of these pump powers are (a) A=3.85 and B=0.36, (b) A=2.26 and B=0.27, (c) A=1.81, B=0.25, (d) A=1.56 and B=0.23, (e) A=0.98, B=0.20, and (f) A=0.81 and B=0.20. The exact shapes of the simulated spectra match very well with the experimental spectra for low input pump powers (2.1 W and 5.5 W), but tend to lack the "filled-in" character of the experimental spectra at higher powers (6.7 W, 8.3 W, 12.7 W and 17.4 W).

A.3 Discussion

Hart *et al.* [28] postulated that strong candidates for the possible physical sources of the phase fluctuations are stimulated Brillouin scattering, stimulated

Raman scattering and fiber medium inhomogeneities. Brillouin scattering was eliminated as a source, since a backward propagating wave, which is a signature of Brillouin scattering in optical fibers, was not observed in the experiments. We have modeled stimulated Raman scattering [27, 37] for our system and have found no evidence to support the hypothesis that it could be a possible source of the stochastic phase fluctuations for fiber lengths up to 50 meters and pump power levels up to 5.5 Watts. A more detailed discussion of the Raman scattering simulations performed is given in Chap. 3. Apart from these, quantum phase fluctuations are another well known, though extremely weak, source of phase noise in optical fibers [8, 38].

Fiber medium inhomogeneities were identified as the major cause of the stochastic phase fluctuations. These inhomogeneities can manifest themselves through spatial and/or temporal fluctuations in the fiber parameters, namely, the linear refractive index n_0 , the group velocity v_g , the group velocity dispersion $\beta^{(2)}$ and the nonlinearity γ [39]. Of these, the fluctuation in the linear refractive index was found to be the only source of phase fluctuation that had a significant effect on the dynamics. A relationship between the level of refractive index fluctuations and the corresponding level of phase fluctuations has been arrived at. It is found that refractive index fluctuations as small as $\sigma_n^2 \sim 10^{-17} \text{ m}^{-1}$ can cause the desired phase fluctuations. Possible sources of these refractive index fluctuations are discussed below.

Consider the modified nonlinear Schrödinger equation (NLSE) which is stated below, with the linear multiplicative noise term represented in terms of spatial and

temporal fluctuations in the refractive index of the fiber.

$$\frac{\partial U}{\partial z} + \frac{i\beta^{(2)}}{2T_0^2} \frac{\partial^2 U}{\partial \tau^2} + \frac{\alpha U}{2} + ik_0 \delta n(z, \tau) U - i\gamma P_0 |U|^2 U = 0, \quad (\text{A.14})$$

where $\delta n(z, \tau)$ is the spatial and temporal variation of the refractive index along the fiber. It can be caused by temperature and density fluctuations in the fiber [40].

The thermodynamic estimate for Δn is given by [40]

$$\langle \Delta n^2 \rangle = \frac{-kT\rho^2}{V^2} \left(\frac{\partial V}{\partial P} \right)_T \left(\frac{\partial n}{\partial \rho} \right)_T^2 + \frac{kT^2}{\rho V C_v} \left(\frac{\partial n}{\partial T} \right)_\rho^2. \quad (\text{A.15})$$

This gives the mean-square index fluctuation in terms of the properties of the material. It can be rewritten as

$$\langle \Delta n^2 \rangle = \frac{V_\rho + V_T}{V} = \langle \Delta n^2 \rangle_\rho + \langle \Delta n^2 \rangle_T. \quad (\text{A.16})$$

For a fiber of length $z=1$ m and radius $r=2.82 \mu\text{m}$ (Volume $V=2.5 \times 10^{-12} \text{m}^3$), these have been calculated to be

$$\begin{aligned} \langle \Delta n^2 \rangle_\rho &\sim 10^{-21} \quad \equiv \quad \langle \Delta \rho^2 \rangle \sim 10^{-14} \frac{kg^2}{m^6}, \\ \langle \Delta n^2 \rangle_T &\sim 10^{-23} \quad \equiv \quad \langle \Delta T^2 \rangle \sim 10^{-12} \text{ }^\circ\text{C}^2. \end{aligned} \quad (\text{A.17})$$

It should be noted that $\langle \Delta n^2 \rangle \propto (1/z) \Rightarrow \delta n \propto (1/\sqrt{z})$. The corresponding phase fluctuation that this would lead to in the NLSE is given by $\delta\phi = k_0 \delta n z \propto \sqrt{z}$, which is equivalent to the prescription for incorporating phase fluctuations into the stochastic NLSE model described in Sec. 2.3, namely, $\langle \Delta \phi^2 \rangle = 6.7 \times 10^{-3} z$. Hart *et al.* [28] used the same prescription and the same noise strength in their truncated-ODE model. From this we can estimate the level of refractive index fluctuation that

corresponds to the noise strength used in the simulations described in Sec. 2.3

$$\begin{aligned} \langle \Delta n^2 \rangle &= \frac{6.7 \times 10^{-3}}{k_0^2} = 6.78 \times 10^{-17} \\ &\equiv \langle \Delta T^2 \rangle \sim 10^{-6} \text{ }^\circ\text{C}^2 \equiv \Delta T \sim 10^{-3} \text{ }^\circ\text{C} \end{aligned} \quad (\text{A.18})$$

The temperature coefficient of the refractive index of silica [40], $(\partial n / \partial T)_\rho \sim 10^{-5} \text{ }^\circ\text{C}^{-1}$. Thus even small spatio-temporal temperature fluctuations of $\sim 10^{-3} \text{ }^\circ\text{C}$ are enough to cause the inferred level of refractive index fluctuations.

The refractive index fluctuations could also be due to inhomogeneities in the density of the fiber material, frozen in at the time of manufacture of the fiber. The simulations were averaged over ~ 600 iterations to get a good estimate of the power fluctuations in the sidebands. Initially, simulations were performed with a different phase noise distribution for each iteration. Later, a particular (arbitrary) phase noise distribution was selected and frozen for all the iterations. This did not reduce the level of damping observed in the sideband trajectories provided that the strength of the phase noise was kept the same, thus indicating that density fluctuations induced during fiber manufacture could be a possible source. The phase noise was modeled as δ -correlated in both space and time. A more realistic approach would be to use correlated noise. Numerical methods to incorporate linear multiplicative correlated noise into the NLSE have been developed by M.J. Werner *et al.* [32].

A.4 Conclusions

The role of stochasticity in the dynamical evolution of four-wave-mixing processes in an optical fiber has been investigated. This research consisted of theoretical

and numerical computations. It focuses on tracing the evolution of the sidebands, generated through FWM, along a length of optical fiber. Detailed comparisons were made with the experimental results of Hart *et al.* [28] and the agreement was excellent. The present work uses numerical techniques that have much higher resolution and better efficiency, and it presents a theoretical basis for the role of the stochasticity in the dynamics. The system is known to be governed by the nonlinear Schrödinger equation (NLSE) to a very good approximation [8].

A powerful technique that can be used for simulations of the stochastic NLSE is the Split-step Fourier Method (SSFM) [8]. An algorithm for the direct implementation of stochastic processes along the length of the fiber in the SSFM has been developed. The advantages of this approach with respect to the coupled-ODE approach are that we can carry out simulations with much higher frequency and time resolution without sacrificing computational efficiency.

The physical sources of these stochastic phase fluctuations are investigated quantitatively and are identified to be due to fluctuations in the linear refractive index of the fiber. Strong candidates for the causes of these refractive index fluctuations are temperature fluctuations in the fiber medium caused by the fluctuating temperature of the fiber environment, density fluctuations in the fiber medium frozen into the fiber during manufacture, and intrinsic thermodynamic fluctuations in the temperature and density of the fiber.

The experiments performed by Hart *et al.* [28] can be used to determine the level of these refractive index fluctuations in commercial fibers. Results described in Figs. 2 and 3 represent a destructive experiment that measures the sideband

evolution with fiber length for a fixed input pump power, necessarily requiring the fiber to be cut repeatedly. The level of refractive index fluctuations can be used as a parameter in the simulations to best fit the experimental results. Alternatively, Fig. 4 represents a non-destructive experiment that measures the sideband evolution with input pump power for a fixed fiber length. These experiments are found to be effective for estimating the refractive index fluctuations, as the dynamics is observed to be sensitively dependent on the strength of the phase fluctuations.

Appendix B

Overview

The understanding of nonlinear processes in optical fibers is crucial towards extending the capabilities of modern optical communication systems based on wavelength division multiplexing (WDM), where each communication channel is represented by a unique wavelength. One of the nonlinear processes that limits the information carrying capacity of a WDM system is four-wave mixing (FWM), which causes cross-talk between neighboring channels. This places a lower limit on the wavelength separation between adjacent channels and an upper limit on the input power in each channel. In this study, we describe a process by which the evolution of FWM processes in an optical fiber can be used to estimate the inhomogeneities in the fiber core material, in particular the fluctuations in the linear refractive index of the fiber core.

Experiments measuring the evolution of FWM processes along a length of fiber were carried out by Hart *et al.* [28] and are described in detail in Sec. 2.2. In this experiment, two input pump waves at frequencies ω_1 and ω_2 , interacted with each other through the third-order nonlinearity of the fiber material to generate first-order sidebands at frequencies $\omega_3 = 2\omega_1 - \omega_2$ and $\omega_4 = 2\omega_2 - \omega_1$. These waves further interacted to produce second-order sidebands at $\omega_5 = 2\omega_3 - \omega_4$ and $\omega_6 = 2\omega_4 - \omega_3$. Higher-order sidebands were also generated. The normalized power in the sideband

at frequency ω_m was represented by ρ_m . The evolution of the FWM processes was characterized by the evolution of $\rho_m(z)$ as a function of fiber length z .

In the present work, we make a quantitative comparison between these experimental results and our numerical results based on efficient algorithms [8] to solve the nonlinear Schrödinger equation (NLSE) that governs the system. The numerical model, its underlying assumptions and the results are described in Sec. B.3. A realistic description of a standard single mode optical fiber must take into account the random phase perturbations a light wave undergoes while propagating through it, without disturbing the underlying conservative properties of the system. The NLSE needs to be suitably modified in order to incorporate the stochastic nature of the propagation. In order to preserve the conservative properties of the system, the stochastic terms in the NLSE must necessarily be multiplicative in nature as an additive term acts as a source or a sink. An algorithm that achieves this with linear, Gaussian, δ -correlated noise is outlined in Sec. B.3. This algorithm preserves the unconditional stability of the system. At the same time, care is taken to transform the stochastic NLSE from its original Ito representation [29] to the computationally feasible Stratanovich representation [30] by compensating for the spurious linear drift that results from integrating such stochastic differential equations [31, 32, 33, 34]. The dominant sources of phase noise are discussed in Sec. B.4.

Conclusions on the relevance of the experiments of Hart *et al.* [28] and the stochastic modeling presented here are summarized in Sec. B.5.

B.1 Experimental and Computational Background

In this work, we focus on tracing the evolution of the sidebands, generated through FWM, along a length of optical fiber. The FWM spectral evolution along 50 m of fiber for two input pump power regimes (2.1 W and 5.5 W) was investigated [28]. In the 2.1 W case, the sideband evolution followed a damped sinusoid along the length of the fiber. The experiments also found that the two first-order sidebands (ρ_3 -blueshifted and ρ_4 -redshifted from the two pumps) had different evolutions along the fiber (with different spatial wavelengths). For the 5.5 W case, the evolution of both first- and second-order sidebands was measured. The damping in the first-order sidebands (ρ_3 and ρ_4) occurred faster than in the 2.1 W case. Experiments probing the dependence of the sideband power on the input power (ranging from 2 W to 17 W) were also performed at a fixed output length of 50 m of the fiber. At the same fiber length, the optical spectra for input powers ranging from 2 W to 17 W were also recorded [28]. The spectral envelopes were observed to fit well to a hyperbolic secant function and the fit parameters were recorded. Measurements with a high-resolution wavemeter showed that one of the two pumps consisted of two very closely spaced longitudinal modes ($\Delta\nu \sim 0.5$ GHz) which were not resolved by the spectrometer used to record the FWM spectra. Inclusion of this multimode nature of the pump input in their model was found to alter the sideband dynamics dramatically and partly explained the asymmetry between the blue-shifted and red-shifted sidebands though it did not account for the damping in the sidebands. This was accounted for by adding weak phase fluctuations to the waves as they propagated

along the fiber [28]. The physical source of these phase fluctuations was not known at that time. However, the inclusion of the phase fluctuations into the model gave excellent qualitative and quantitative agreement with experiment. Their model involved integration of a system of coupled ODEs derived from the NLSE [35] by a process of truncation that retained only the leading frequency components (the pumps and the first- and second-order sidebands), a process justified by the fact that the input pump waves are well approximated by a combination of monochromatic waves. Their final numerical results are based on simulations using the truncated-ODE model with Langevin noise terms representing phase fluctuations in the fiber. Another physical source of stochasticity in their experiment was the inherent power fluctuation in the lasers used as the input pumps. The level of fluctuations (5-20%) was measured and incorporated appropriately into their model through stochastic initial conditions. This explained the evolution of the level of observed fluctuations in the sideband trajectories although it was found to be inadequate by itself, to account for the damping of the trajectories. They found that all three physical characteristics mentioned above, namely the multimode nature of the pump input, the stochastic phase fluctuations along the length of the fiber, and the stochastic initial power fluctuations were crucial to explaining the different features of the experimental measurements [28].

B.2 Stochastic NLSE Model

In the present work, we have developed and implemented an unconditionally stable scheme for integrating the NLSE that successfully incorporates phase noise into the SSFM. Thus, we are now in a position to harness the high frequency / time resolution of the SSFM together with its efficient convergence properties. Due to these advances, we are now able to do simulations with much higher frequency resolution (60 MHz as compared to 300 GHz in the ODE model). This high resolution, coupled with an appropriate convolution scheme, enables us to compare these simulated spectra with the composite spectra observed by the spectrometers which had a resolution of ~ 60 GHz. This was not possible with the truncated ODE model as the resolution of the simulated spectra in that case was ~ 300 GHz. For exactly the same levels of phase fluctuations, and initial condition fluctuations as used in Ref. [28], comparisons for the present NLSE model with the experimental sideband evolution functions $\rho_i(z)$ show excellent quantitative agreement. These results, along with the algorithms employed, are described in detail in this section. We have identified linear refractive index fluctuations along the fiber length to be a strong candidate for a physical source of the stochastic phase fluctuations. A comparison between the various possible sources is given in Sec. B.4.

Under the assumption that the electric field of the light in the fiber has a slowly varying envelope $A(z, \tau)$, and that the fiber medium has an instantaneous nonlinear response, the system is well described by the nonlinear Schrödinger equation (NLSE)

with a linear multiplicative stochastic term

$$\frac{\partial U}{\partial z} + \frac{i\beta^{(2)}}{2T_0^2} \frac{\partial^2 U}{\partial \tau^2} + \frac{\alpha U}{2} + i\Gamma(z, \tau)U - i\gamma P_0 |U|^2 U = 0. \quad (\text{B.1})$$

Z is distance along the length of the fiber, $U(z, \tau) = A(z, \tau)/\sqrt{P_0}$ is the complex electric field envelope $A(z, \tau)$ normalized to the absolute amplitude of the field $\sqrt{P_0}$, P_0 is the total power in the fiber, τ is time normalized to a convenient time scale T_0 (~ 1 ns) measured in a reference frame moving with the group velocity of the pulse [$\tau = (t - z/v_g)/T_0$]. The simulations are carried out for exactly the same physical parameters as the experiments and simulations reported by Hart *et al.* [28], i.e., $\beta^{(2)} = 55$ (ps)²/km, is the group velocity dispersion of the fiber at the operating wavelength $\lambda_0 \sim 632$ nm ($k_0 \sim 10^7$ m⁻¹). A loss of ~ 6 dB/km gives $\alpha = 0.0014$ m⁻¹ as the loss in the fiber at this wavelength. The nonlinearity coefficient $\gamma = 0.019$ W⁻¹m⁻¹ is given by

$$\gamma = \frac{\omega_{ave} n_2^I}{c A_{eff}}, \quad (\text{B.2})$$

where A_{eff} is the effective core area of the fiber, n_2^I is the Kerr coefficient for the intensity-dependent refractive index, and ω_{ave} is the average angular frequency of the wave envelope. $\Gamma(z, \tau)$ is a linear multiplicative phase noise field. In this study the noise field is assumed to be δ -correlated in both space and time. The evolution of the FWM dynamics is found to be sensitive to the strength of this noise field. It can be physically interpreted as phase noise arising due to fluctuations in the linear refractive index of the fiber medium. A detailed discussion of its physical origin is given in Sec. B.4.

The system was simulated using the Split-Step Fourier Method (SSFM) [8].

An algorithm for appropriately incorporating stochastic phase fluctuations along the length of the fiber in the SSFM was developed and is summarized below.

The NLSE is composed of linear and nonlinear terms, and can be written in operator form as

$$\begin{aligned}
\frac{\partial U}{\partial z} &= (\hat{D} + \hat{S} + \hat{N})U \\
\hat{D} &= \frac{-i\beta^{(2)}}{2T_0^2} \frac{\partial^2}{\partial \tau^2} - \frac{\alpha}{2} \\
\hat{S} &= i\Gamma(z, \tau) \\
\hat{N} &= i\gamma P_0 |U|^2,
\end{aligned} \tag{B.3}$$

where \hat{D} , \hat{S} and \hat{N} are linear (dispersive), nonlinear and stochastic operators, respectively. It has an exact solution for infinitesimal Δz given by -

$$U(z + \Delta z, \tau) = \exp[\Delta z(\hat{D} + \hat{S} + \hat{N})]U(z, \tau), \tag{B.4}$$

which can be approximated by

$$U(z + \Delta z, \tau) \approx \exp[\Delta z \hat{D}] \exp[\Delta z \hat{S}] \exp[\Delta z \hat{N}] U(z, \tau). \tag{B.5}$$

The execution of $\exp[\Delta z \hat{N}]$ is carried out in τ -space:

$$B_1(z, \tau) = \exp[\Delta z \hat{N}] U(z, \tau). \tag{B.6}$$

The execution of $\exp[\Delta z \hat{S}]$ and $\exp[\Delta z \hat{D}]$ is carried out in ω -space.

In particular, the stochastic phase fluctuations are introduced by modifying the phase ϕ_j of each frequency component ω_j of the complex field according to

$$\begin{aligned}
B_2(z, \omega) &= \mathcal{F}[B_1(z, \tau)] \\
B_3(z, \omega_j) &= \exp[i\delta\phi(z, \omega_j)] B_2(z, \omega_j),
\end{aligned} \tag{B.7}$$

where \mathcal{F} represents the Fourier transform operation.

This process only modifies the phase of each complex frequency component, leaving its absolute value unchanged. Thus the algorithm conserves the total power and the unconditional stability of the system.

The stochastic phase fluctuations $\delta\phi(z, \omega_j)$ are taken to be δ -correlated in frequency as well as spatially along the fiber length. The Box-Muller algorithm [36] was used to generate Gaussian random deviates from computer-generated uniform random deviates r_{1j} and r_{2j} at each spatial step and for each frequency component ω_j . The fluctuations are given by

$$\delta\phi(z, \omega_j) = \sqrt{-2\sigma_\phi^2 \Delta z \ln(r_{1j})} \cos(2\pi r_{2j}). \quad (\text{B.8})$$

This is followed by the execution of $\exp[\Delta z \hat{D}]$, which is also carried out in Fourier space, followed by the inverse transform

$$U(z + \Delta z, \tau) = \mathcal{F}^{-1}[\exp[\Delta z \hat{D}(i\omega)] B_3(z, \omega)]. \quad (\text{B.9})$$

$\hat{D}(i\omega)$ is obtained by replacing $(\partial/\partial\tau)$ by $i\omega$.

The basic form of the initial complex wave envelope function is

$$U(0, \tau) = \exp\left(-\frac{\tau^2}{2\tau_p^2}\right) \left\{ \begin{array}{l} \exp\left(\frac{i\Omega\tau}{2}\right) + \\ \exp\left(-\frac{i\Omega\tau}{2}\right) \end{array} \right\}, \quad (\text{B.10})$$

where τ_p is the pulse width $T_p = 5$ ns FWHM, normalized to the time scale T_0 , $\Omega = 366$ GHz is the frequency detuning between the two laser sources normalized to a frequency scale $\Omega_0 = 62.5$ MHz. Figure B.1(a) shows a plot of this pulse $|U(0, \tau)|^2$. The overall Gaussian envelope has an FWHM of 5 ns, the closely spaced dark lines

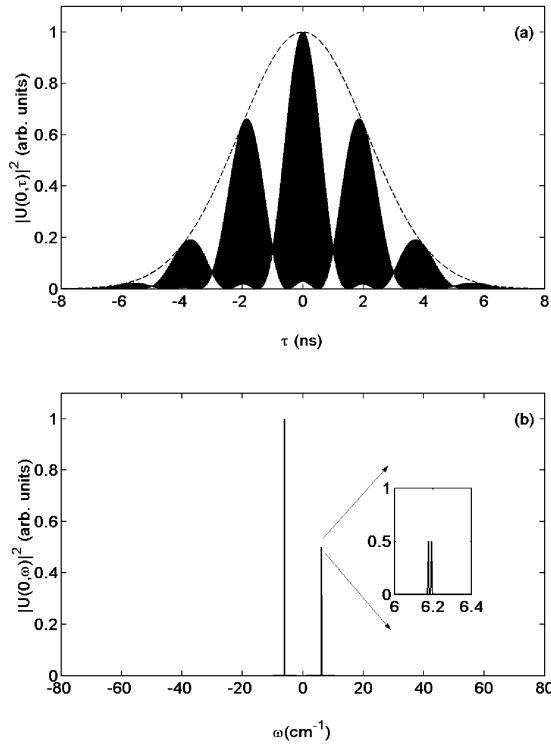


Figure B.1: Multimode pulse input to the NLSE: (a) input pulse in time domain and (b) input spectrum.

are due to the 366 GHz (~ 3 ps) beating between the two input pump frequencies. The 2 ns modulations on the pulse are due to the 0.5 GHz mode-structure in the blue-shifted pump wave. Figure 2.1(b) shows the input spectrum of this pulse which consists of two highly monochromatic pump waves with a detuning of $\Omega=366$ GHz. The spectrum of the blue-shifted pump, upon magnification, is seen to be composed of two very closely spaced peaks, with a separation of $\Delta\nu=0.5$ GHz. Hart *et al.* [28] did not use pulsed wave functions in their NLSE simulations as the size of the FFT required to do so made it computationally prohibitive at that time. The size of the FFT was chosen such that it would accommodate a time span of 16 ns in order to go sufficiently far into the wings on the Gaussian pulse; and a frequency span of 16 THz in order to accommodate all the sidebands generated and prevent spurious effects due to the reflection boundary conditions implicit in the SSFM algorithm. These considerations dictated the size of the FFT to be $\geq(16 \text{ THz})\cdot(16 \text{ ns}) = 256000$. The nearest power of 2 is $2^{18} = 262144$, which has been used throughout the present work. The incorporation of the pulsed nature of the light was found to be necessary in explaining the dynamics. From the perspective of the coupled amplitude equations used by Hart *et al.* [28], the present model is equivalent to a coupled-ODE model with 2^{18} coupled ODEs.

Upon incorporation of the multimode nature of the blue input pump laser source and the stochastic fluctuations in the initial power in the lasers, the initial

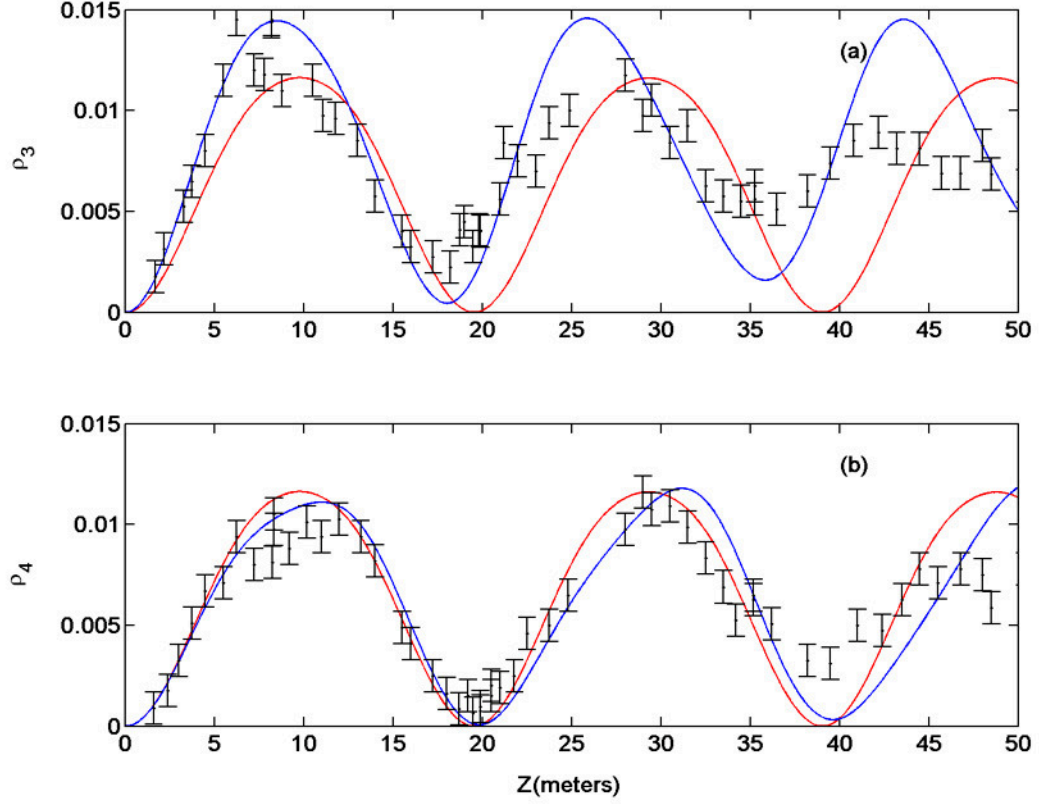


Figure B.2: Effects of inclusion of the multimode nature ($\Delta\nu = 0.5$ GHz) of the blue-shifted input pump laser on the 1st order sideband evolution as a function of fiber length for $P_0 = 2.1$ W. Dashed curves represent simulations without the multimode nature and solid curves represent simulations with the multimode nature. $\Omega = 366$ GHz, $\gamma = 0.019$ W⁻¹ m⁻¹, and $\beta^{(2)} = 55$ ps²/km (a) power in the blue-shifted sideband, (b) power in the red-shifted sideband.

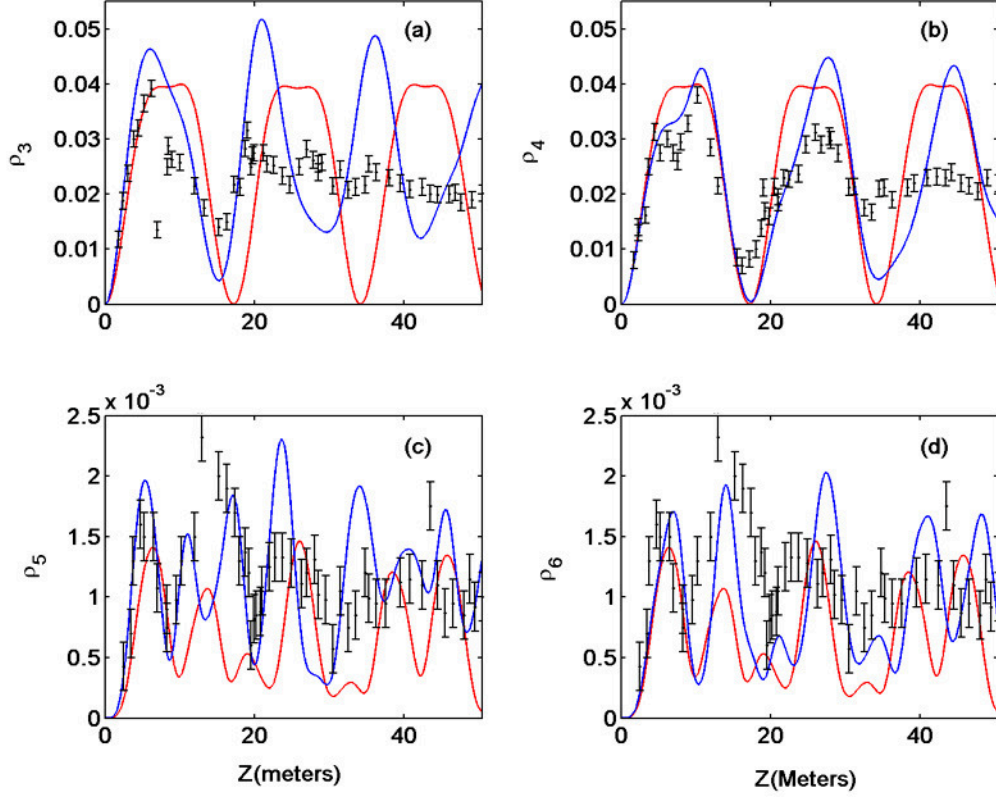


Figure B.3: Effects of inclusion of the multimode nature ($\Delta\nu = 0.5$ GHz) of the blue-shifted input pump laser on the 1st order sideband evolution as a function of fiber length for $P_0 = 5.5$ W. Dashed curves represent simulations without the multimode nature and solid curves represent simulations with the multimode nature. $\Omega = 366$ GHz, $\gamma = 0.019$ W $^{-1}$ m $^{-1}$, and $\beta^{(2)} = 55$ ps 2 /km (a) power in the first-order blue-shifted sideband, (b) power in the first-order red-shifted sideband, (c) power in the second-order blue-shifted sideband, (d) power in the second-order red-shifted sideband.

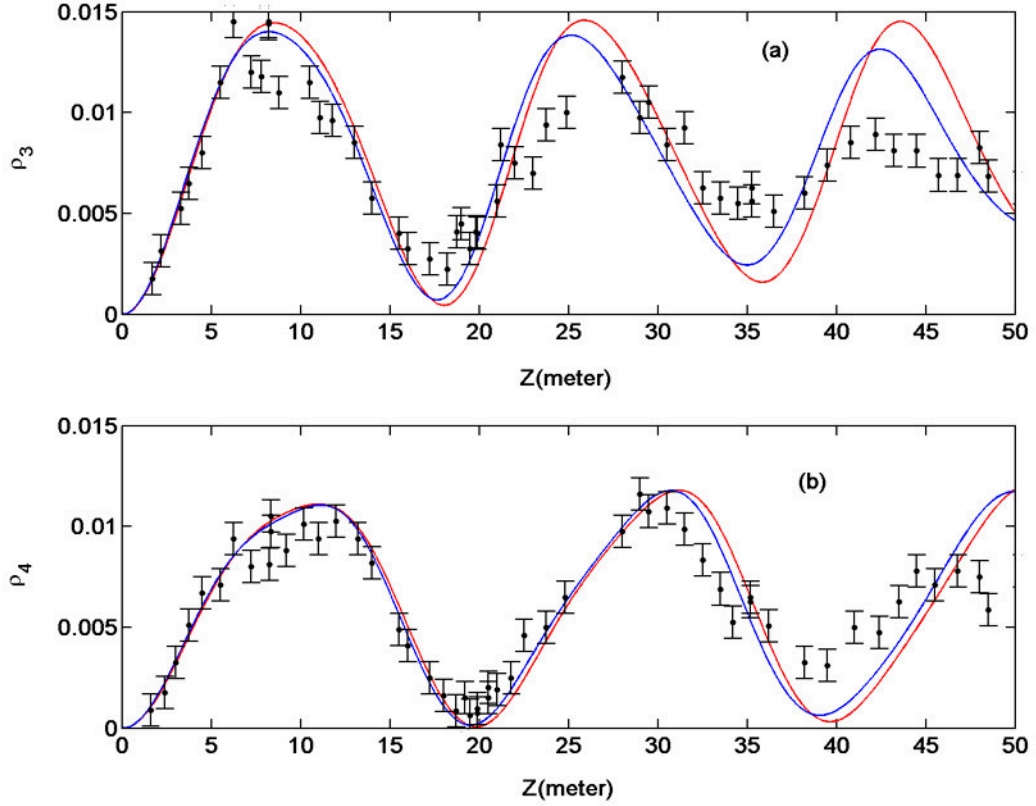


Figure B.4: Effects of inclusion of the pulsed nature (5 ns FWHM) of the input pump laser light on the first-order sideband evolution as a function of fiber length for $P_0 = 2.1$ W. Dashed curves represent cw simulations and solid curves represent pulsed simulations. $\Omega = 366$ GHz, $\Delta\nu = 0.5$, $\gamma = 0.019$ W $^{-1}$ m $^{-1}$, and $\beta^{(2)} = 55$ ps 2 /km (a) power in the blue-shifted sideband, (b) power in the red-shifted sideband.

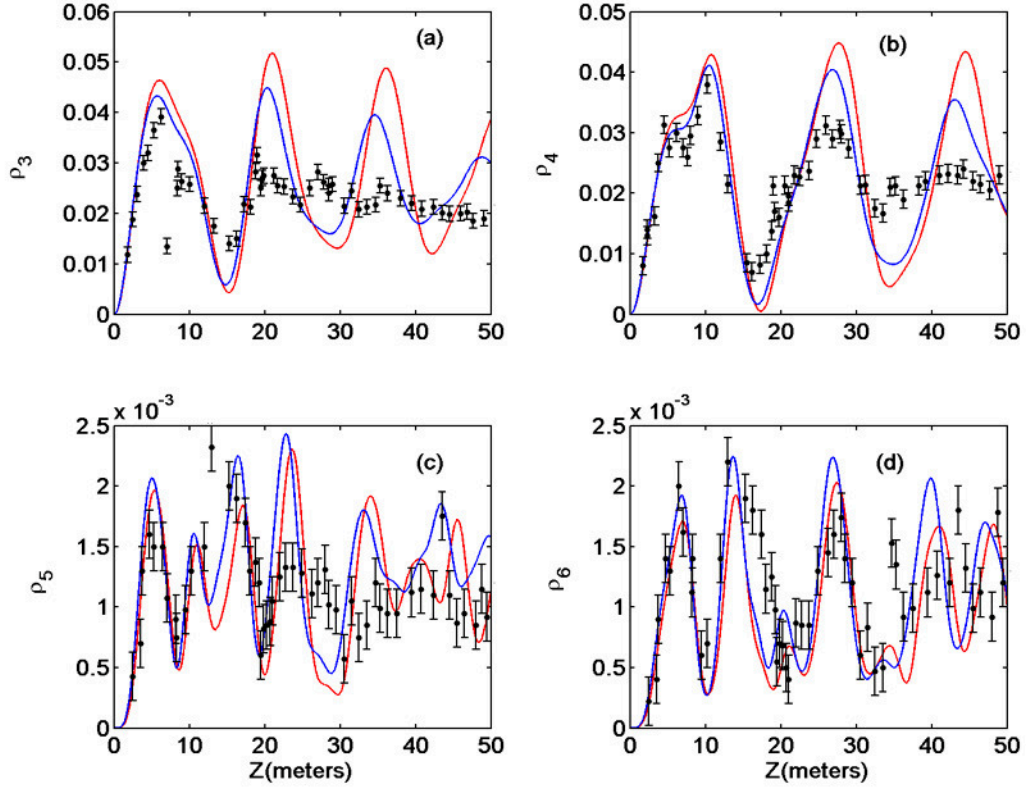


Figure B.5: Effects of inclusion of the pulsed nature (5 ns FWHM) of the input pump laser on the first- and second-order sideband evolution as a function of fiber length for $P_0 = 5.5$ W. Dashed curves represent cw simulations and solid curves represent pulsed simulations. $\Omega = 366$ GHz, $\Delta\nu = 0.5$, $\gamma = 0.019$ W $^{-1}$ m $^{-1}$, and $\beta^{(2)} = 55$ ps 2 /km (a) power in the first-order blue-shifted sideband, (b) power in the first-order red-shifted sideband, (c) power in the second-order blue-shifted sideband, (d) power in the second-order red-shifted sideband.

wave function takes the form

$$U(0, \tau) = \exp\left(-\frac{\tau^2}{2\tau_p^2}\right) \left\{ \begin{array}{l} \sqrt{\frac{1+\delta\rho_1}{2}} \left[\begin{array}{l} \exp\left(\frac{i(\Omega+\Delta\nu)\tau}{2}\right) + \\ \exp\left(\frac{i(\Omega-\Delta\nu)\tau}{2}\right) \end{array} \right] \\ + \sqrt{1+\delta\rho_2} \exp\left(-\frac{i\Omega\tau}{2}\right) \end{array} \right\}. \quad (\text{B.11})$$

$\Delta\nu = 0.5$ GHz is the frequency separation between the two longitudinal modes in the blue-shifted pump. $\delta\rho_1$ and $\delta\rho_2$ are Gaussian random deviates (generated using the Box-Muller algorithm [36]) that represent the initial power fluctuations in each of the pump laser sources. Their standard deviations were taken to be, $\sigma_{\rho_1} = 0.2$, $\sigma_{\rho_2} = 0.11$ for simulations from 0 m to 20 m, $\sigma_{\rho_1} = 0.12$, $\sigma_{\rho_2} = 0.05$ for simulations from 20 m to 50 m along the length of the fiber. This is exactly the same prescription used by Hart *et al.* [28] in their simulations and is dictated by their experimental measurements of the fluctuations in the pump laser intensities.

At this point it is worth noting the effects of the inclusion of two attributes of the input laser light, namely, the multimode nature of the blue-shifted pump, and the pulsed nature of the input light (assumed to be cw in the simulations reported by Hart *et al.* [28]).

Figure B.2 shows a comparison between simulations with (solid curves) and without (dashed curves) the multimode nature for an input pump power of 2.1 Watts. The simulations with the mode structure show the asymmetry between the blue- and red-shifted sideband evolution, in particular, the difference in spatial wavelength between the two, and a non-return to zero nature of the evolution, as observed in the experimental data (black dots with error bars). These features are

absent in the simulations without mode-structure. ρ_3 and ρ_4 stands for the first order blue- and red-shifted sidebands respectively. Figure 2.3 shows the corresponding comparison for the case of 5.5 Watts of input pump power. Here, too, the simulations incorporating the multimode nature of the blue-shifted pump (solid curves) are seen to be an improvement over those not incorporating it (dashed curves). A feature of the experimental data (black dots with errorbars) is that for the ρ_3 sideband, the initial part of the evolution involves a peak followed by a shoulder, while for the ρ_4 sideband, the initial part of the evolution involves a shoulder followed by a peak. This feature, too, is seen to occur as a result of the inclusion of the multimode nature of the blue-shifted pump.

The effect of inclusion of the pulsed nature of the input beam is seen in Fig. B.4 (for the 2.1 Watt case) and Fig. B.5 (for the 5.5 Watt case). The solid dashes represent simulations for a cw input beam and the solid curves represent those for a pulsed input beam. The incorporation of the pulsed nature clearly results in damping of the sideband trajectories which are seen to come closer to the experimental data [28] (black dots with error bars).

Use of the FFT algorithm makes evaluation relatively fast compared to other finite-difference schemes. The computational error is $O(\Delta z^2)$, thus the solution converges with decreasing spatial step-size Δz .

The simulations were tested for the conservation of total power along the fiber length (by setting the loss α to zero) and for the conservation of asymmetry [35, 28]

given by

$$C(Z) = \sum_{i=1}^{\infty} (2i - 1) [\rho_{2i-1}(Z) - \rho_{2i}(Z)]. \quad (\text{B.12})$$

A clearer picture of the evolution of the sidebands is obtained by plotting both the power in the sidebands and their standard deviations as a function of length along the fiber. Figures B.6(a) and B.6(b) show a comparison between simulation and experiment of the evolution of the first-order blue-shifted (ρ_3) and red-shifted (ρ_4) sidebands, respectively, for an input power of 2.1 W. The dashed curves represent NLSE simulations which include the stochastic nature of the input powers of the pump lasers but exclude the stochastic phase fluctuations added along the length of the fiber, an attribute which is included in the simulations represented by the solid curves. The black dots with error bars represent the experimental data. The measured sideband power, normalized to the total power in the fiber, is periodic in length but appears to be damping to a constant value. The measured data also show a clear difference between the spatial wavelengths of oscillation of the blue-shifted (ρ_3) and red-shifted (ρ_4) sidebands trajectories, respectively. Both these features are captured well by both the simulations. Figures B.6(c) and B.6(d) compare experimental and simulated measures of the evolution of the standard deviation in the sideband power along the fiber length. It is clearly observed that simulations with phase noise added to the light field along the length of the fiber (solid curves) are closer to the experimental data as compared to those that exclude this feature (dashed curves). This indicates the instrumental nature of the phase fluctuations in explaining key features of the dynamics.

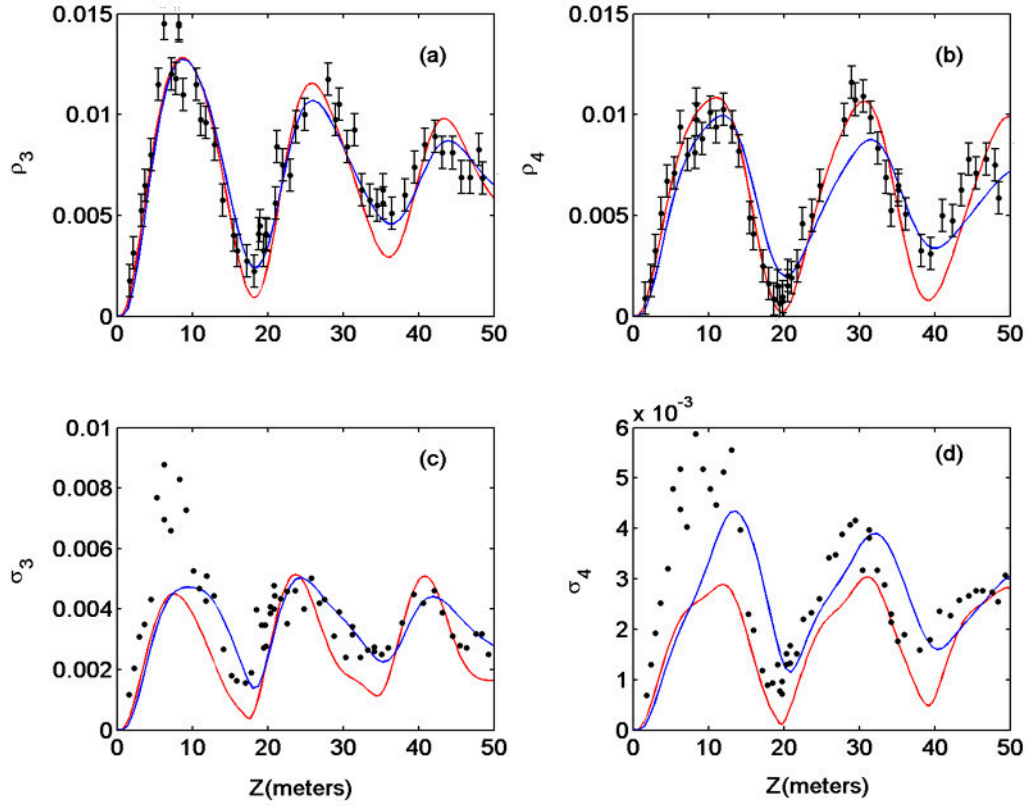


Figure B.6: Comparison between the experimental measurements [28](black), the random initial condition NLSE model excluding phase noise (dashed curves) and the stochastic phase noise NLSE model (solid curves) showing the first-order sideband evolution as a function of fiber length for $P_0 = 2.1$ W, $\Omega = 366$ GHz, $\Delta\nu = 0.5$ GHz, $\gamma = 0.019$ W $^{-1}$ m $^{-1}$, and $\beta^{(2)} = 55$ ps 2 /km: dynamical evolution of the: (a) power in the blue-shifted sideband, (b) power in the red-shifted sideband, (c) fluctuations in the blue-shifted sideband, (d) fluctuations in the red-shifted sideband.

The apparent damping of the periodic sideband trajectory is seen more dramatically in Figs. B.7(a) and B.7(b), which show the evolution of the first-order sideband power along the fiber for an input power of 5.5 W. The two first-order sidebands evolve differently. They appear to damp to a constant value at a faster rate than for the case with an input pump power of 2.1 W. Here again, NLSE simulations that incorporate phase noise along the length of the fiber (solid curves) are much more successful in accurately capturing the dynamical features of the system than NLSE simulations that do not take this feature into account (dashed curves). Figures B.7(c) and B.7(d) show a comparison between the simulated and measured standard deviations. Comparisons for the second-order blue-shifted (ρ_5) and red-shifted (ρ_6) sidebands, respectively, are shown in Figs. B.7(e) and B.7(f).

The observed dynamical evolution of the sidebands is found to depend sensitively on the strength of the stochastic phase fluctuations. Yet, best agreement with the experimental results of Hart *et al.* [28] is achieved with exactly the same noise strength σ_ϕ^2 as used in their truncated ODE model, namely, $\sigma_\phi^2 = 0.0067 \text{ m}^{-1}$. They report that including phase noise in their FWM calculations resulted in a spurious linear drift in the trajectories for the sideband power with length. To remove this artifact of the computations, they added a linear loss to their coupled ODEs. They set the loss coefficient $\alpha = 0.0046 \text{ m}^{-1}$ by finding the value that removed this increasing slope. We have observed exactly the same secular growth phenomenon for a wide range of the noise strength σ_ϕ^2 and have arrived at an empirical prescription for α namely, $\alpha \sim \sigma_\phi^2$, where σ_ϕ^2 is the variance of the added phase noise. This indicates the general nature of dynamics resulting from the addition of stochastic,

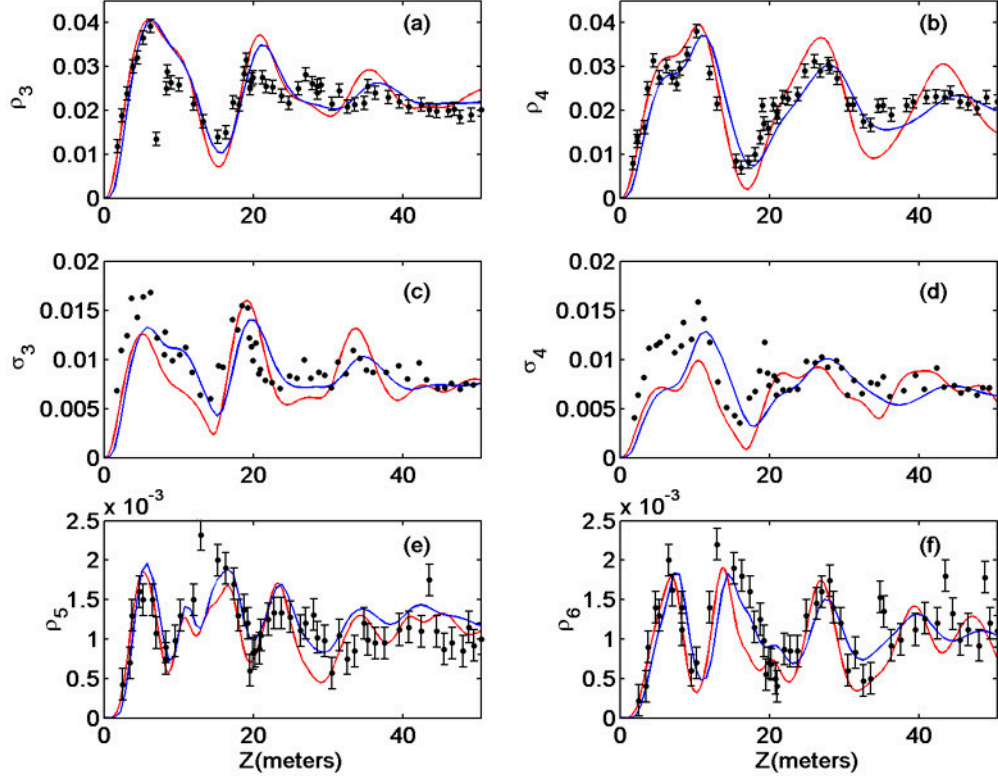


Figure B.7: This figure caption is indented and single-spaced. Comparison between the experimental measurements [28] (black), the random initial condition NLSE model excluding phase noise (dashed curves) and the stochastic phase noise NLSE model (solid curves) showing the first- and second-order sideband evolution as a function of fiber length for $P_0 = 5.5 \text{ W}$, $\Omega = 366 \text{ GHz}$, $\Delta\nu = 0.5 \text{ GHz}$, $\gamma = 0.019 \text{ W}^{-1}\text{m}^{-1}$, and $\beta^{(2)} = 55 \text{ ps}^2/\text{km}$: dynamical evolution of the: (a) power in the first-order blue-shifted sideband, (b) power in the first-order red-shifted sideband, (c) fluctuations in the first-order blue-shifted sideband, (d) fluctuations in the first-order red-shifted sideband, (e) power in the second-order blue-shifted sideband, (f) power in the second-order red-shifted sideband.

δ -correlated phase fluctuations to systems governed by nonlinear partial differential equations [31].

It is remarkable that the strength of the phase noise required is the same in both the 2.1 W and the 5.5 W cases. Further, it is worth noting that exactly the same noise strength was used by Hart *et al.* [28], the difference being that they introduced phase noise only in the pump frequencies, whereas we have introduced it in all the Fourier modes ($\sim 2^{18}$). As a confirmation of this result, they also performed experiments and numerical simulations examining the sideband power dependence on the input power at a fixed length of 50.4 m of the same fiber. We have repeated these simulations with the stochastic NLSE model and the results are shown in Figs. B.8(a) (blue-shifted sideband) and B.8(b) (red-shifted sideband). The experimental measurements of the sideband powers are represented by filled squares and the results of numerical simulations are represented by triangles (without phase noise) and by circles (with phase noise). The simulations are seen to follow the general trend seen in the experiments. As the pump power is increased, the triangles (without phase noise) start to disagree with experiment, whereas the circles (with phase noise) are much closer to experiment. The phase noise strength used in these simulations was exactly the same as that used in the simulations depicted in Figs. B.6 and B.7. The agreement between the phase noise simulations and the experimental data was (once again) highly sensitive to the noise strength. Since this experiment (unlike those shown in Figs. B.2 - B.7) is non-destructive, it can be used to deduce the strength of phase noise processes in a given optical fiber. It will be shown in Sec. B.4 that a likely cause of the phase noise is fluctuation in the linear refractive

index of the fiber. The noise strength deduced from the present computational study corresponds to a refractive index inhomogeneity of $\langle \Delta n^2 \rangle \sim 10^{-16}$.

Till now the comparisons between our simulations of the full NLSE and the truncated ODE model give basically the same results, although with much better agreement with experiment. However, the full NLSE can also provide a detailed comparison with the experimental spectra. This was not available from the truncated ODE model. The simulations reported in this work were carried out with a very high frequency and time resolution in order to incorporate the fact that the input light was not cw, but was composed of ~ 5 ns long pulses; and that the number of sidebands generated required the frequency spread of the FFT to be ~ 16 THz, while resolving a longitudinal mode-structure of $\Delta\nu \sim 0.5$ GHz. The spectral resolution used was ~ 0.05 GHz, whereas the spectrometer used to observe the spectra had a resolution 1000 times larger (~ 50 GHz). To account for this difference, the simulated spectra were first convolved with a Gaussian of unit peak and 62 GHz FWHM, before they were compared with the observed spectra.

Figures B.9(a) and B.9(b) show three-dimensional plots of the average experimental FWM output spectrum along the length of the fiber for input pump powers of 2.1 W and 5.5 W, respectively (courtesy Hart *et al.* [28]). The vertical axis represents the intensity, normalized to the peak power in one of the input pumps, plotted on a logarithmic scale. The pump frequencies are centered on $\pm \Omega/2$ and the fiber length is increasing into the page. Figures B.9(c) and B.9(d) show the corresponding comparisons based on simulations using the stochastic-NLSE model. The basic features of the spectral evolution are captured by the simulations.

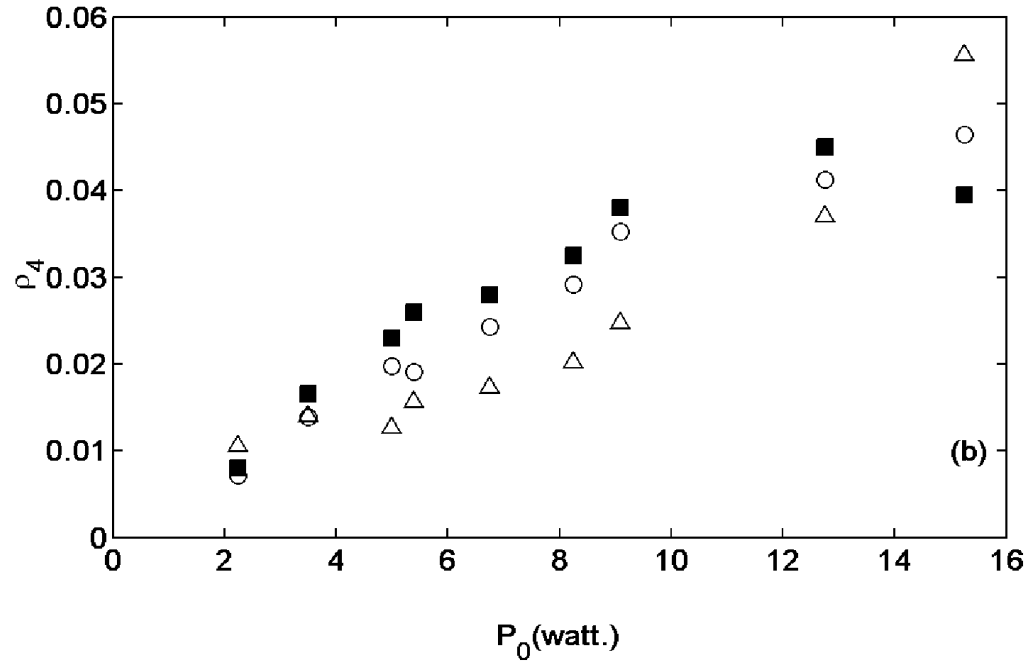
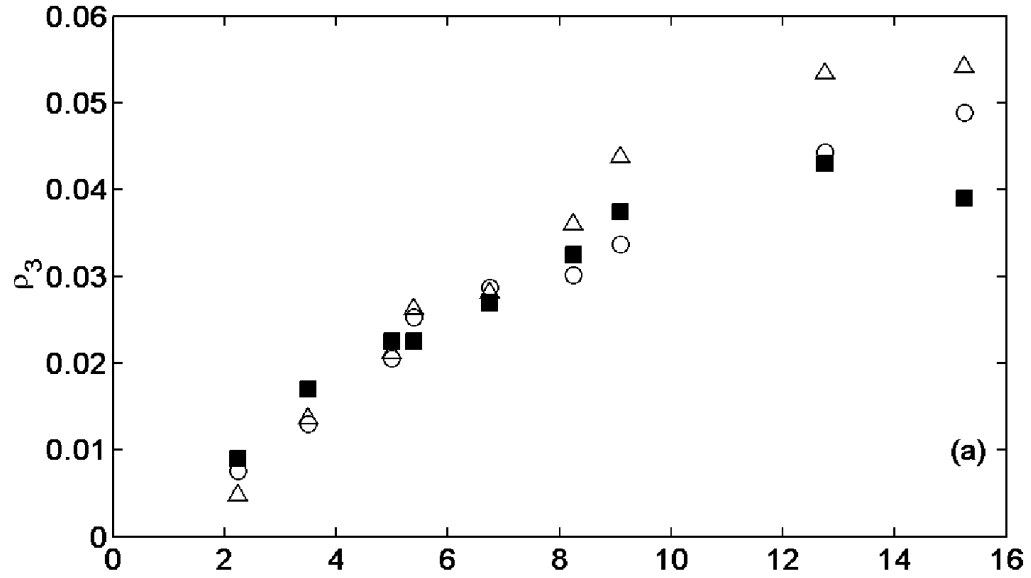


Figure B.8: Comparison between the experimental measurements (filled squares), simulations without stochastic phase fluctuations (open triangles) and with stochastic phase fluctuations (open circles) of the first-order sideband power versus pump input power for $L=50.39$ m, and $\Omega = 366$ GHz: power in the (a) blue-shifted sideband and (b) red-shifted sideband.

Figure B.9: Evolution of the FWM spectrum along the fiber (a) $P=2.1$ W, experiment, (b) $P=5.5$ W, experiment, (c) $P=2.1$ W, stochastic-NLSE model, (d) $P=5.5$ W, stochastic-NLSE model.

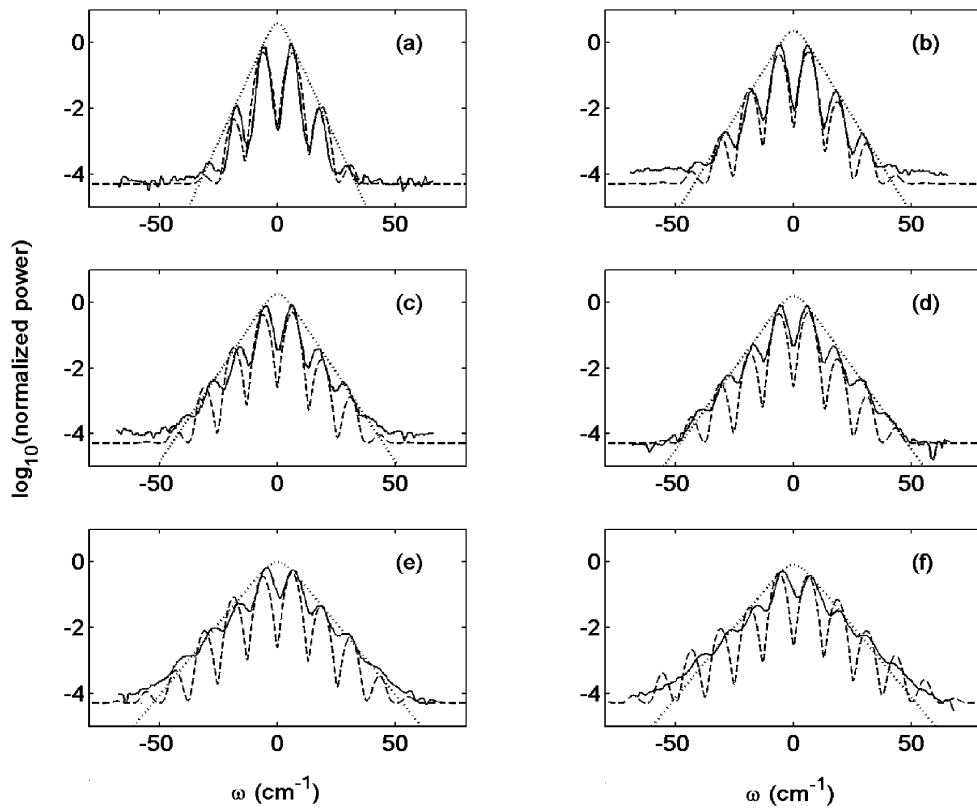


Figure B.10: Experimental FWM output spectrum (solid line), convolved spectra from simulations of the stochastic NLSE model (dashed line), and hyperbolic secant envelope fit (dotted line) for pump input powers P_0 of (a) 2.1 W, (b) 5.5 W, (c) 6.7 W, (d) 8.3 W, (e) 12.7 W, (f) 17.4 W, fiber length $L= 50.39$ m, $\Omega = 366$ GHz, $\Delta\nu = 0.5$ GHz, $\gamma = 0.019$ W⁻¹m⁻¹, and $\beta^{(2)} = 55$ ps²/km.

Hart *et al.* [28] also documented the experimentally observed FWM output spectra for a fixed fiber length of 50.39 meters for 6 different input pump powers. They state the coefficients A and B of the hyperbolic secant envelopes that best fit the output spectra which are given by

$$f(\omega) = A \operatorname{sech}(B\omega), \quad (\text{B.13})$$

where A and B are the experimental fit parameters.

The hyperbolic secant parameters A and B, that best fit the simulated spectra are exactly the same as those that best fit the experimental spectra [28] for all the 6 cases of input power considered. Figure 2.10 shows an overlap of the simulated spectra (dashed line), with the experimental spectra (solid line) and the experimental hyperbolic secant envelope (dotted line) for 6 different pump powers, namely, (a) 2.1 W, (b) 5.5 W, (c) 6.7 W, (d) 8.3 W, (e) 12.7 W, (f) 17.4 W. The hyperbolic secant parameters for each of these pump powers are (a) A=3.85 and B=0.36, (b) A=2.26 and B=0.27, (c) A=1.81, B=0.25, (d) A=1.56 and B=0.23, (e) A=0.98, B=0.20, and (f) A=0.81 and B=0.20. The exact shapes of the simulated spectra match very well with the experimental spectra for low input pump powers (2.1 W and 5.5 W), but tend to lack the "filled-in" character of the experimental spectra at higher powers (6.7 W, 8.3 W, 12.7 W and 17.4 W).

B.3 Discussion

Hart *et al.* [28] postulated that strong candidates for the possible physical sources of the phase fluctuations are stimulated Brillouin scattering, stimulated

Raman scattering and fiber medium inhomogeneities. Brillouin scattering was eliminated as a source, since a backward propagating wave, which is a signature of Brillouin scattering in optical fibers, was not observed in the experiments. We have modeled stimulated Raman scattering [27, 37] for our system and have found no evidence to support the hypothesis that it could be a possible source of the stochastic phase fluctuations for fiber lengths up to 50 meters and pump power levels up to 5.5 Watts. A more detailed discussion of the Raman scattering simulations performed is given in Chap. 3. Apart from these, quantum phase fluctuations are another well known, though extremely weak, source of phase noise in optical fibers [8, 38].

Fiber medium inhomogeneities were identified as the major cause of the stochastic phase fluctuations. These inhomogeneities can manifest themselves through spatial and/or temporal fluctuations in the fiber parameters, namely, the linear refractive index n_0 , the group velocity v_g , the group velocity dispersion $\beta^{(2)}$ and the nonlinearity γ [39]. Of these, the fluctuation in the linear refractive index was found to be the only source of phase fluctuation that had a significant effect on the dynamics. A relationship between the level of refractive index fluctuations and the corresponding level of phase fluctuations has been arrived at. It is found that refractive index fluctuations as small as $\sigma_n^2 \sim 10^{-17} \text{ m}^{-1}$ can cause the desired phase fluctuations. Possible sources of these refractive index fluctuations are discussed below.

Consider the modified nonlinear Schrödinger equation (NLSE) which is stated below, with the linear multiplicative noise term represented in terms of spatial and

temporal fluctuations in the refractive index of the fiber.

$$\frac{\partial U}{\partial z} + \frac{i\beta^{(2)}}{2T_0^2} \frac{\partial^2 U}{\partial \tau^2} + \frac{\alpha U}{2} + ik_0 \delta n(z, \tau) U - i\gamma P_0 |U|^2 U = 0, \quad (\text{B.14})$$

where $\delta n(z, \tau)$ is the spatial and temporal variation of the refractive index along the fiber. It can be caused by temperature and density fluctuations in the fiber [40].

The thermodynamic estimate for Δn is given by [40]

$$\langle \Delta n^2 \rangle = \frac{-kT\rho^2}{V^2} \left(\frac{\partial V}{\partial P} \right)_T \left(\frac{\partial n}{\partial \rho} \right)_T^2 + \frac{kT^2}{\rho V C_v} \left(\frac{\partial n}{\partial T} \right)_\rho^2. \quad (\text{B.15})$$

This gives the mean-square index fluctuation in terms of the properties of the material. It can be rewritten as

$$\langle \Delta n^2 \rangle = \frac{V_\rho + V_T}{V} = \langle \Delta n^2 \rangle_\rho + \langle \Delta n^2 \rangle_T. \quad (\text{B.16})$$

For a fiber of length $z=1$ m and radius $r=2.82 \mu\text{m}$ (Volume $V=2.5 \times 10^{-12} \text{m}^3$), these have been calculated to be

$$\begin{aligned} \langle \Delta n^2 \rangle_\rho &\sim 10^{-21} \quad \equiv \quad \langle \Delta \rho^2 \rangle \sim 10^{-14} \frac{\text{kg}^2}{\text{m}^6}, \\ \langle \Delta n^2 \rangle_T &\sim 10^{-23} \quad \equiv \quad \langle \Delta T^2 \rangle \sim 10^{-12} \text{ }^\circ\text{C}^2. \end{aligned} \quad (\text{B.17})$$

It should be noted that $\langle \Delta n^2 \rangle \propto (1/z) \Rightarrow \delta n \propto (1/\sqrt{z})$. The corresponding phase fluctuation that this would lead to in the NLSE is given by $\delta\phi = k_0 \delta n z \propto \sqrt{z}$, which is equivalent to the prescription for incorporating phase fluctuations into the stochastic NLSE model described in Sec. 2.3, namely, $\langle \Delta \phi^2 \rangle = 6.7 \times 10^{-3} z$. Hart *et al.* [28] used the same prescription and the same noise strength in their truncated-ODE model. From this we can estimate the level of refractive index fluctuation that

corresponds to the noise strength used in the simulations described in Sec. 2.3

$$\begin{aligned} \langle \Delta n^2 \rangle &= \frac{6.7 \times 10^{-3}}{k_0^2} = 6.78 \times 10^{-17} \\ &\equiv \langle \Delta T^2 \rangle \sim 10^{-6} \text{ }^\circ\text{C}^2 \equiv \Delta T \sim 10^{-3} \text{ }^\circ\text{C} \end{aligned} \quad (\text{B.18})$$

The temperature coefficient of the refractive index of silica [40], $(\partial n / \partial T)_\rho \sim 10^{-5} \text{ }^\circ\text{C}^{-1}$. Thus even small spatio-temporal temperature fluctuations of $\sim 10^{-3} \text{ }^\circ\text{C}$ are enough to cause the inferred level of refractive index fluctuations.

The refractive index fluctuations could also be due to inhomogeneities in the density of the fiber material, frozen in at the time of manufacture of the fiber. The simulations were averaged over ~ 600 iterations to get a good estimate of the power fluctuations in the sidebands. Initially, simulations were performed with a different phase noise distribution for each iteration. Later, a particular (arbitrary) phase noise distribution was selected and frozen for all the iterations. This did not reduce the level of damping observed in the sideband trajectories provided that the strength of the phase noise was kept the same, thus indicating that density fluctuations induced during fiber manufacture could be a possible source. The phase noise was modeled as δ -correlated in both space and time. A more realistic approach would be to use correlated noise. Numerical methods to incorporate linear multiplicative correlated noise into the NLSE have been developed by M.J. Werner *et al.* [32].

B.4 Conclusions

The role of stochasticity in the dynamical evolution of four-wave-mixing processes in an optical fiber has been investigated. This research consisted of theoretical

and numerical computations. It focuses on tracing the evolution of the sidebands, generated through FWM, along a length of optical fiber. Detailed comparisons were made with the experimental results of Hart *et al.* [28] and the agreement was excellent. The present work uses numerical techniques that have much higher resolution and better efficiency, and it presents a theoretical basis for the role of the stochasticity in the dynamics. The system is known to be governed by the nonlinear Schrödinger equation (NLSE) to a very good approximation [8].

A powerful technique that can be used for simulations of the stochastic NLSE is the Split-step Fourier Method (SSFM) [8]. An algorithm for the direct implementation of stochastic processes along the length of the fiber in the SSFM has been developed. The advantages of this approach with respect to the coupled-ODE approach are that we can carry out simulations with much higher frequency and time resolution without sacrificing computational efficiency.

The physical sources of these stochastic phase fluctuations are investigated quantitatively and are identified to be due to fluctuations in the linear refractive index of the fiber. Strong candidates for the causes of these refractive index fluctuations are temperature fluctuations in the fiber medium caused by the fluctuating temperature of the fiber environment, density fluctuations in the fiber medium frozen into the fiber during manufacture, and intrinsic thermodynamic fluctuations in the temperature and density of the fiber.

The experiments performed by Hart *et al.* [28] can be used to determine the level of these refractive index fluctuations in commercial fibers. Results described in Figs. 2 and 3 represent a destructive experiment that measures the sideband

evolution with fiber length for a fixed input pump power, necessarily requiring the fiber to be cut repeatedly. The level of refractive index fluctuations can be used as a parameter in the simulations to best fit the experimental results. Alternatively, Fig. 4 represents a non-destructive experiment that measures the sideband evolution with input pump power for a fixed fiber length. These experiments are found to be effective for estimating the refractive index fluctuations, as the dynamics is observed to be sensitively dependent on the strength of the phase fluctuations.

Bibliography

- [1] G.P. Agrawal, *Nonlinear Fiber Optics* (Academic Press, San Diego, CA, 2001), Chap. 1.
- [2] N. Bloembergen, *Nonlinear Optics* (Benjamin, Reading, MA, 1977).
- [3] Y.R. Shen, *Principles of Nonlinear Optics* (Wiley, New York, 1984).
- [4] P.N. Butcher and D.N. Cotter, *The Elements of Nonlinear Optics* (Cambridge University Press, Cambridge, UK, 1990).
- [5] R.W. Boyd, *Nonlinear Optics* (Academic Press, San Diego, CA, 1992).
- [6] A.C. Newell and J.V. Moloney *Nonlinear Optics (Advanced Topics in the Interdisciplinary Mathematical Sciences)* (Westview Press, Boulder, CO, April 1992).
- [7] D. Marcuse, *Light Transmission Optics* (Van Nostrand Reinhold, New York, 1982), Chaps. 8 and 12.
- [8] G.P. Agrawal, *Nonlinear Fiber Optics* (Academic Press, San Diego, CA, 2001), Chap. 2.
- [9] P. Diament, *Wave Transmission and Fiber Optics* (Macmillan, New York, 1990).
- [10] V.E. Zakharov and A. Shabat, Sov. Phys. JETP **34**, 62 (1972)
- [11] R.H. Hardin and F.D. Tappert, SIAM Rev. Chronicle **15**, 423 (1973).
- [12] R.A. Fisher and W.K. Bischel, Appl. Phys. Lett. **23**, 661 (1973); J. Appl. Phys **46**, 4921 (1975).
- [13] J.W. Cooley and J.W. Tukey, Math. Comput. **19**, 297 (1965).
- [14] R. Trebino, D.J. Kane, "Using phase retrieval to measure the intensity and phase of ultrashort pulses: frequency resolved optical gating," J. Opt. Soc. Am. B **10**, 1101 (1993).
- [15] D.J. Kane, R. Trebino, "Characterization of Arbitrary Femtosecond Pulses Using Frequency-Resolved Optical Gating," IEEE J. Quant. Elect. **29**, 571 (1993).

- [16] D.J. Kane, R. Trebino, "Single-shot measurement of the intensity and phase of an arbitrary ultrashort pulse by using frequency-resolved optical gating," *Opt. Lett.* **10**, 1101 (1993).
- [17] P. O'Shea, M. Kimmel, X. Gu, R. Trebino, "Highly simplified device for ultrashort-pulse measurement," *Opt. Lett.* **26**, 932 (2001).
- [18] G.P. Agrawal, *Nonlinear Fiber Optics* (Academic Press, San Diego, CA, 2001), Chap. 3.
- [19] G.P. Agrawal, *Nonlinear Fiber Optics* (Academic Press, San Diego, CA, 2001), Chap. 4.
- [20] G.P. Agrawal, *Nonlinear Fiber Optics* (Academic Press, San Diego, CA, 2001), Chap. 10.
- [21] G.P. Agrawal, *Nonlinear Fiber Optics* (Academic Press, San Diego, CA, 2001), Chap. 7.
- [22] G.P. Agrawal, *Nonlinear Fiber Optics* (Academic Press, San Diego, CA, 2001), Chap. 6.
- [23] R.H. Stolen, E.P. Ippen, and A.R. Tynes, *Appl. Phys. Lett.* **20**, 62 (1972).
- [24] E.P. Ippen and R.H. Stolen, *Appl. Phys. Lett.* **21**, 539 (1972).
- [25] R.G. Smith, *Appl. Opt.* **11**, 2489 (1972).
- [26] G.P. Agrawal, *Nonlinear Fiber Optics* (Academic Press, San Diego, CA, 2001), Chap. 9.
- [27] G.P. Agrawal, *Nonlinear Fiber Optics* (Academic Press, San Diego, CA, 2001), Chap. 8.
- [28] D.L. Hart, Arthur F. Judy, Rajarshi Roy and James W. Beletic, *Phys. Rev. E* **57**, 4757 (1998); D.L. Hart, Arthur F. Judy, T.A.B. Kennedy, Rajarshi Roy and K. Stoev, *Phys. Rev. A* **50**, 1807 (1994).
- [29] K. Ito, *Lectures on Stochastic Processes* (Tata Institute of Fundamental Research, Bombay, 1960).
- [30] R.L. Stratanovich, *Topics in the Theory of Random Noise*, Vols I. and II. (Gordon & Breach, New York, 1963).

- [31] H. Risken, *The Fokker-Planck Equation* (Springer-Verlag, Berlin, 1989).
- [32] M.J. Werner and P.D. Drummond, *J. Comput. Phys.* **132**, 312 (1997).
- [33] P.D. Drummond and I.K. Mortimer, *J. Comput. Phys.* **93**, 144 (1991).
- [34] S.J. Carter, *Phys. Rev. A.* **51**, 3274 (1995).
- [35] J.R. Thompson and Rajarshi Roy, *Phys. Rev. A* **43**, 4987 (1991).
- [36] W.H. Press, S.A. Teukolsky, W.T. Vetterling and B.P. Flannery, *Numerical Recipes in Fortran: The Art of Scientific Computing* (Cambridge University Press, Cambridge, 1992).
- [37] C. Headley, G.P. Agrawal, *IEEE J. Quantum Electron.* **QE-31**, 2058 (1995),
C. Headley, G.P. Agrawal *J. Opt. Soc. Am. B.* **13**, 2170 (1995).
- [38] S.H. Perlmutter, M.D. Levenson, R.M. Shelby and M.B. Weisman, *Phys. Rev. Lett.* **61** 1388, 1988.
- [39] F. Kh. Abdullaev, J.H. Hensen, S. Bischoff and M.P. Sorensen, *J. Opt. Soc. Am. B.* **15**, 2424 (1998); F. Kh. Abdullaev, J.G. Caputo, and Nikos Flytzanis, *Phys. Rev E.* **50**, 1552 (1994).
- [40] William H. Glenn, *IEEE J. Quantum Electron.* **QE-25**, 1218 (1989).
- [41] R. Trebino. *Frequency-Resolved Optical Gating: The Measurement of Ultrashort Laser Pulses* (Kluwer Academic 2002).
- [42] G.P. Agrawal *Nonlinear Fiber Optics* (Academic, San Diego, 2001).
- [43] J.M. Dudley, X. Gu, L. Xu, M. Kimmel, E. Zeek, P. O'Shea, R. Trebino, S. Coen, R.S. Windeler, "Cross-correlation frequency resolved optical gating analysis of broadband continuum generation in photonic crystal fiber: simulations and experiments," *Opt. Express* **10**, 1215 (2002).
- [44] Q.D. Liu, J.T. Chen, Q.Z. Wang, P.P. Ho, and R.R. Alfano, "Single pulse degenerate-cross-phase modulation in a single-mode optical fiber," *Opt. Lett.* **20**, 542 (1995).
- [45] T. Sylvestre, H. Maillotte, E. Lantz, and D. Gindre "Combined spectral effects of pulse walk-off and degenerate cross-phase modulation in birefringent fibers", *Journal of Nonlinear Optical Physics and Materials* **6**, 313-320 (1997).

- [46] Q.D. Liu, L. Shi, P.P. Ho, R.R. Alfano, R.J. Essiambre, and G.P. Agrawal, "Degenerate cross-phase modulation of femtosecond laser pulses in a birefringent single-mode fiber," *IEEE Photon. Tech. Lett.* **9**, 1107 (1997).
- [47] F.G. Omenetto, B.P. Luce, D. Yarotski and A.J. Taylor, "Observation of chirped soliton dynamics at $\lambda = 1.55$ mm in a single-mode optical fiber with frequency-resolved optical gating," *Opt. Lett.* **24**, 1392 (1999).
- [48] F.G. Omenetto, Y. Chung, D. Yarotski, T. Shaefer, I. Gabitov and A.J. Taylor, "Phase analysis of nonlinear femtosecond pulse propagation and self-frequency shift in optical fibers," *Opt. Commun.* **208**, 191 (2002).
- [49] F.G. Omenetto, J.W. Nicholson, B.P. Luce, D. Yarotski, A.J. Taylor, "Shaping, propagation and characterization of ultrafast pulses in optical fibers," *Appl. Phys. B* **70**[Suppl.], S143 (2000).
- [50] N. Nishizawa and T. Goto, "Experimental analysis of ultrashort pulse propagation in optical fibers around zero-dispersion region using cross-correlation frequency resolved optical gating," *Opt. Express* **8**, 328 (2001).
- [51] N. Nishizawa and T. Goto, "Trapped pulse generation by femtosecond soliton pulse in birefringent optical fibers," *Opt. Express* **10**, 256 (2002).
- [52] N. Nishizawa and T. Goto, "Characteristics of pulse trapping by use of ultrashort soliton pulses in optical fibers across the zero-dispersion wavelength," *Opt. Express* **10**, 1151 (2002).
- [53] N. Nishizawa and T. Goto, "Ultrafast all optical switching by use of pulse trapping across zero-dispersion wavelength," *Opt. Express* **11**, 359 (2003).
- [54] , K. Ogawa, M.D. Pelusi, "Characterization of ultrashort optical pulses in a dispersion-managed fiber link using two-photon absorption frequency-resolved optical gating," *Opt. Commun.* **198**, 83-87 (2001).
- [55] R.A. Altes, "Detection, estimation, and classification with spectrograms," *J. Acoust. Soc. Am.* **67**(4), 1232 (1980).
- [56] A. Christian Silva, "GRENOUILLE - Practical Issues," unpublished.
- [57] J. Garduno-Mejia, A.H. Greenaway, and D.T. Reid, "Designer femtosecond pulses using adaptive optics," *Opt. Express* **11** 2030 (2003).

- [58] P. O'Shea, M. Kimmel, X. Gu, R. Trebino, "Increased-bandwidth in ultrashort-pulse measurement using an angle-dithered nonlinear-optical crystal," *Opt. Express* **7**, 342 (2000).
- [59] P. O'Shea, M. Kimmel, R. Trebino, "Increased phase-matching bandwidth in simple ultrashort-laser-pulse measurements," *J. Opt. B* **4**, 44 (2002).
- [60] S. Akturk, M. Kimmel, P. O'Shea, R. Trebino, "Measuring pulse-front tilt in ultrashort pulses using GRENOUILLE", *Opt. Express* **11**, 491 (2003).
- [61] K. J. Blow, D. Wood, "Theoretical Description of Transient Stimulated Raman Scattering in Optical Fibers," *IEEE J. Quant. Elect.* **25**, 2665 (1989).
- [62] R.H. Stolen, J.P. Gordon, W.J. Tomlinson, *J. Opt. Soc. Am. B* **6**, 1159 (1989).
- [63] P.V. Mamyshev and S.V. Chernikov, *Sov. Lightwave Commun.* **2**, 97 (1992).
- [64] C. Headley III, *Ultrafast Stimulated Raman Scattering in Optical Fibers, Ph.D. Thesis, University of Rochester, NY (1995).*